Seasonal variability of the surface ocean carbon cycle: a synthesis

Draft: April 3rd 2023

Keith B. Rodgers[1,2,*], Jörg Schwinger[3,*], Andrea J. Fassbender[4], Peter Landschützer[5], Ryohei Yamaguchi[6], Hartmut Frenzel[7,4], Karl Stein[1,2], Jens Daniel Müller[8], Nadine Goris[3], Sahil Sharma[1,9], Seth Bushinsky[10], Thi-Tuyet-Trang Chau[11], Marion Gehlen[11], M. Angeles Gallego[10], Lucas Gloege[12], Luke Gregor[8], Nicolas Gruber[8], Judith Hauck[13], Yosuke Iida[14], Masao Ishii[15], Lydia Keppler[16], Ji-Eun Kim[1,2], Sarah Schlunegger[17], Jerry Tjiputra[3], Katsuya Toyama[14], Pradeebane Vaittinada Ayar[3,10], Antón Velo[18]

* corresponding authors: keithbrodgers@gmail.com, jrsc@norceresearch.no

1. Center for Climate Physics, Institute for Basic Science, Busan, Republic of Korea
2. Pusan National University, Busan, Republic of Korea
3. NORCE Climate & Environment, Bjerknes Centre for Climate Research, Bergen, Norway
4. NOAA/OAR Pacific Marine Environmental Laboratory, Seattle, USA
5. Flanders Marine Institute (VLIZ), Oostende, Belgium
6. Japan Agency for Marine-Earth Science and Technology, Yokosuka, Japan
7. Cooperative Institute for Climate, Ocean, and Ecosystem Studies (CICOES), University of Washington, Seattle, WA, USA
8. Environmental Physics, Institute of Biogeochemistry and Pollutant Dynamics, ETH Zürich, Zürich, Switzerland
9. Department of Climate System, Pusan National University, Busan, South Korea
10. Department of Oceanography, School of Ocean and Earth Science and Technology, University of Hawai‘i at Mānoa, Honolulu, Hawai‘i
11. Laboratoire des Sciences du Climat et de l’Environnement, Gif-sur-Yvette, France
12. Open Earth Foundation, California, USA
13. Alfred Wegener Institute, Helmholtz Centre for Polar and Marine Research, Bremerhaven, Germany
14. Atmosphere and Ocean Department, Japan Meteorological Agency, Tokyo, Japan
15. Climate and Geochemistry Research Department, Meteorological Research Institute, Japan Meteorological Agency, Tsukuba, Japan
16. Scripps Institution of Oceanography, University of California San Diego, La Jolla, USA
17. AOS Program, Princeton University, Princeton, USA
18. Institute of Marine Research, Spanish National Research Council (CSIC), Vigo, Spain

Abstract

The seasonal cycle is the dominant mode of variability in the air-sea CO_2 flux in most regions of the global ocean, yet discrepancies between different seasonality estimates are rather large. As part of the Regional Carbon Cycle Assessment and Processes phase 2 project (RECCAP2), we synthesize surface ocean pCO_2 and air-sea CO_2 flux seasonality from models and observation-based estimates, focusing on both a modern climatology and decadal changes between the 1980s and 2010s. Four main findings emerge: First, global ocean biogeochemistry models (GOBMs) and observation-based estimates (pCO_2 products) of surface pCO_2 seasonality disagree, primarily due to discrepancies in the seasonal variability in surface DIC. Second, the seasonal cycle in pCO_2 has increased in amplitude over the last three decades in both pCO_2 products and GOBMs. Third, decadal increases in pCO_2 seasonal cycle amplitudes in subtropical biomes for both pCO_2 products and GOBMs are driven by increasing DIC concentrations stemming from the uptake of anthropogenic CO_2 (C_{ant}). In subpolar and Southern Ocean biomes, however, the seasonality change for GOBMs is dominated by C_{ant} invasion, whereas for pCO_2 products an indeterminate combination of C_{ant} invasion and climate change modulates the changes. Fourth, we have shown that biome-aggregated decadal changes in the amplitude of pCO_2 seasonal variability are largely detectable against both mapping uncertainty (reducible) and natural variability uncertainty (irreducible), but not at the gridpoint scale over much of the northern subpolar oceans and over the Southern Ocean, underscoring the importance of sustained high-quality seasonally-resolved measurements over these regions.

Plain Language Summary

Changes in the amplitude of seasonal variations in the surface ocean carbon dioxide partial pressure (pCO_2) over the period 1985-2018 are described over the historical period spanning 1985-2018, using both observation-based and model-based estimates. We identify increasing pCO_2 seasonality over most regions that is largely driven by the impact of the invasion flux of anthropogenic carbon into the surface ocean, with observation-based products also revealing

important modulations of pCO_2 seasonality in high latitude regions also being impacted by perturbations to the climate system. We also identified that there are important discrepancies between observation-based and modeled pCO_2 seasonality over global scales, with much of this likely associated with systematic biases in model representations of the seasonal cycle in surface dissolved inorganic carbon (DIC). Both reducible and irreducible forms of uncertainty in monitoring pCO_2 seasonality changes are quantified, with both cases highlighting the need for sustained seasonally-resolving measurements over the high latitudes as part of an optimized marine carbon observing system.

Key points:

(1) Changes in pCO_2 seasonal cycle amplitude over 1985-2018 are detectable against both mapping uncertainty and natural variability uncertainty.
(2) The dominant driver of pCO_2 amplitude increases over decadal timescales is attributed to the direct effect of C_{ant} invasion.
(3) A discrepancy is identified with surface DIC variability being systematically lower in GOBMs than in surface DIC observation-based products.

1 Introduction

How is the ocean carbon cycle changing as a consequence of sustained increases in emissions of carbon to the atmosphere? Important steps toward answering this question over the last several decades have been provided via estimates of ocean carbon uptake from both interior hydrographic measurements (Gruber et al., 2019; Sabine et al., 2004), surface fluxes inferred from measurements of the sea surface partial pressure of CO_2 (pCO_2) (Chau et al., 2022; Gregor et al., 2019; Landschützer et al., 2014; Rödenbeck et al., 2015), global ocean biogeochemistry model simulations (Friedlingstein, et al., 2022; Hauck et al., 2020; Orr et al., 2001) and ocean inverse models (Gloor et al., 2003; Gruber et al., 2009). A first global synthesis was performed roughly a decade ago through the REgional Carbon Cycle Assessment and Processes (RECCAP) project (https://www.globalcarbonproject.org/reccap), highlighting the inevitable forced carbon cycle changes, while also identifying sources of uncertainty.

In a parallel direction of inquiry, it has also become clear that the seasonal cycle in surface ocean pCO_2 (and thereby air-sea CO_2 flux) has been changing, with this first identified in modeling studies (Rodgers et al., 2008; Riebesell et al., 2009; Gorgues et al., 2010; Hauck and Völker, 2015; Gallego et al., 2018) and subsequently inferred from observational constraints (Fassbender et al., 2018; Landschützer et al., 2018) and more recently also identified from changes in the seasonal cycle of atmospheric CO_2 induced by air-sea CO_2 fluxes in the Southern Ocean (Yun et al., 2022). Studies to date show that the dominant drivers of this trend towards increasing pCO_2 seasonal amplitude are the increasing surface concentrations of dissolved inorganic carbon (DIC), due to the invasion of anthropogenic CO_2 into the ocean, and the associated decline in surface ocean buffering capacity. The trend towards increased seasonal amplitude is also expected to be modulated by natural variability and by warming (Schlunegger et al., 2019). The net effect of warming in high emission projections by the end of the 21st century is to enhance increases in the seasonal amplitude of CO_2 fluxes over the expansive subtropical domain by approximately 15% (Rodgers et al., 2020).

Our synthesis effort builds on the earlier studies of Fassbender et al. (2018), Landschützer et al. (2018), and Fassbender et al. (2022), but here we rely on a greatly expanded set of pCO_2 products and GOBMs, spanning the time period 1985 to 2018, to assess the drivers of multi-decadal changes in the seasonal cycle of surface pCO_2. Such changes are of interest for three primary reasons. First, they may impact stressors of marine ecosystems, as emphasized in the analysis of future changes in pH, hydrogen ion concentration, and calcium carbonate mineral saturation state seasonality by Kwiatkowski and Orr (2018). Second, they can have potential impacts for climate feedback mechanisms, as demonstrated by Fassbender et al. (2022) for 21st century climate change under both strong and moderate CO_2 emissions pathways. Third, they will have implications for optimizing the design of the global marine carbon observing system, as summer-biased measurements can lead to significant errors for a system where the seasonal cycle itself is not stationary.

For the majority of the global ocean, the seasonal cycle in sea surface pCO_2 exhibits strong variability that is up to two orders of magnitude larger than the seasonal cycle in atmospheric pCO_2 (e.g. Takahashi et al., 2002). Seasonal variations in pCO_2 reflect the interplay of four principal underlying drivers: sea surface temperature (SST), sea surface salinity (SSS), dissolved inorganic carbon concentrations (DIC), and total alkalinity (TA) (Takahashi et al., 1993, 2002). Variations in these drivers are the result of changes in ocean circulation and mixing, biological processes, as well as exchanges of heat, freshwater, and carbon with the atmosphere. While the temperature-driven or thermal component of observed pCO_2 seasonality is well constrained by laboratory studies and by high-quality satellite-derived SST products, this is not the case for the other drivers. Therefore, observational studies often refer to changes related to DIC, TA, or salinity collectively as changes in the nonthermal component (Takahashi et al., 1993, 2002). Importantly, thermal and nonthermal drivers of pCO_2 seasonality are typically found to be opposed in phase and large in amplitude relative to the resulting net pCO_2 variations. For this reason, skillful modeling of seasonal pCO_2 cycling can be compromised if any of the underlying processes are not well-represented, both for the amplitude and the phase/timing of seasonality changes. Therefore, state-of-the-art models still face challenges in skillfully simulating the seasonal cycle of pCO_2 in regions that are known to be important for CO_2 exchange with the atmosphere (Anav et al., 2013; Goris et al., 2018; Kessler amd Tjiputra, 2016; Mongwe et al., 2018; Pilcher et al., 2015). For the important case of the North Atlantic, it has been shown that future carbon uptake in ESM projections can be constrained by diagnosing the timing and magnitude of modeled seasonal variations in pCO_2 (Goris et al., 2018). Similarly, Nevison et al. (2016) demonstrated, for the Southern Ocean, that the way an ESM represents the seasonal carbon cycle is related to the model's projected carbon uptake. A much weaker seasonal cycle than in higher latitudes is observed in the tropics, where seasonal pCO_2 amplitudes are obscured by interannual variability. In polar latitudes where there is seasonal ice cover, the challenge of data sparsity associated with the difficulty of sampling pCO_2 through the seasonal cycle presents challenges and uncertainty that are beyond the scope of this study.

An important source of uncertainty with detecting anthropogenic trends in the carbon cycle is natural variability. As a matter of definition, we consider the forced anthropogenic signal to

represent the sum total of the effects of anthropogenic forcing on atmospheric radiation (greenhouse gases, anthropogenic aerosols, etc.) and thereby warming ensuing physical and biogeochemical state changes in the ocean, as well as the effect of the invasion flux of anthropogenic carbon into the ocean. For the analysis presented here, even if pCO_2 products were able to perfectly resolve multi-decadal changes in the seasonal amplitude of sea surface pCO_2 over 1985 to 2018, it would not be possible to confidently isolate the anthropogenic trend from the impacts of natural variability. Given that natural variability is an intrinsic property of the Earth system, natural variability uncertainty is understood to be an irreducible form of uncertainty that can nevertheless be quantified. To address the degree to which natural variability obscures detection of anthropogenic trends, we include analyses of large ensemble (LE) simulations with Earth system models (ESMs) in this study. LE simulations were considered previously in the study of Schlunegger et al. (2019) for the case of 21st century climate change projections under strong emissions, and they showed that over the subtropics forced changes in ΔpCO_2 seasonal amplitude are more emergent than forced trends in annual mean ΔpCO_2.

Previous research has pointed towards significant model biases in representing the seasonal cycle of pCO_2 and its underlying drivers (Goris et al., 2018; Mongwe et al., 2018; Rodgers et al., 2014). The question naturally arises as to whether models have improved since the evaluation of seasonal variability in an early generation of prognostic biogeochemistry models (McKinley et al., 2006; Tjiputra et al., 2012). For the case of the North Pacific, the forward models in McKinley et al. (2006) had their seasonal cycles in pCO_2 evaluated directly against time series measurements from observing stations spanning the subpolar and subtropical gyres to identify non-trivial biases in models. Our study differs in that, rather than direct comparisons with time series stations, our observation-based data sources consist of mapped global sea surface pCO_2 products constructed from the same underlying ungridded SOCAT (Surface Ocean CO_2 Atlas; Pfeil et al., 2013) data, as well as ocean interior seasonal climatological fields of DIC.

More extensive analyses for the regions with seasonal ice cover, which are not considered here due to their sparsity of carbon observations for estimating the seasonal cycle, will be

provided by the Arctic and Southern Ocean regional contributions to RECCAP2. Our analysis and synthesis is developed using a diverse set of resources: nine observationally-based pCO_2 products, three of which include associated time-varying monthly surface DIC and TA fields; two independent three-dimensional seasonally-resolved DIC climatologies; hindcast simulations from eleven GOBMs; five large ensemble simulations; and individual realizations of 11 CMIP6 models.

This paper is structured as follows. We begin in the methods section by introducing the RECCAP2 pCO_2 products and GOBMs, along with ancillary products used for this study. In the main results section, we present a descriptive account of changes in pCO_2 seasonality as well as discrepancies between pCO_2 products and GOBMs, followed by attribution of these changes and discrepancies to their drivers. We finally present an analysis focused on identifying detectability of forced/anthropogenic signals, as well as an assessment of the robustness of our chosen biome aggregation for detectability of the forced changes in seasonality to changes due to natural variability. Our objective is to present a synthesis of the carbon cycle community's current knowledge of how the seasonal cycle of sea surface pCO_2 and the air-sea CO_2 exchange has been changing over the last three decades.

2 Methods

2.1 Considered regions

Ocean biomes offer a number of advantages as aggregation regions for studying the global carbon cycle (Fay and McKinley, 2014). For our interests in seasonality, biomes appropriately reflect the structures that are determined by real-world interactions between ocean circulation and biogeochemistry. For all of the oceanic studies within RECCAP2, a discrete number of ocean biomes based on Fay and McKinley (2014) are used to facilitate consistent intercomparison between regions (described in the RECCAP2 Global Ocean contribution by DeVries et al., submitted to the RECCAP2 special issue). This study analyzes pCO_2 and CO_2

flux seasonality for six biomes (**Table 1** and central panel of **Fig. 1**) aggregated from the aforementioned. Our decision to aggregate some biomes and exclude others is based on the following: First, this is a synthesis study and the seasonal cycle in surface ocean pCO_2 exhibits important similarities across the subtropics of each hemisphere. Second, we have elected to not include either the Arctic, the Bering Sea, or the regions of the Southern Ocean that are impacted by ice cover, with the analysis of those regions left to the individual regional RECCAP2 studies. Third, we have chosen to not include the equatorial regions, given that the seasonal cycle there is relatively weak and often obscured by large interannual variability.

Thus, our six aggregated biomes (**Table 1** and **Fig. 1**) consist of North Atlantic subpolar seasonally stratified (NA-SPSS), North Pacific subpolar seasonally stratified (NP-SPSS), Northern Hemisphere subtropical seasonally stratified (NH-STSS), Northern Hemisphere subtropical permanently stratified (NH-STPS), Southern Hemisphere subtropical permanently stratified (SH-STPS), and Southern Hemisphere seasonally stratified (subpolar and subtropical combined, SH-SS). We have elected to keep the North Atlantic and North Pacific subpolar biomes separate in our analysis in light of important differences that arise in their seasonal cycles.

Besides the aggregation as designated in **Table 1**, adjustments have been taken to avoid confounding changes in observational coverage with seasonality or changes in seasonality. We limit our analysis to regions that have valid observation-based (and GOBM) fields for the whole time period 1985-2018 for all pCO_2 products and for all variables considered in this study (CO_2 fluxes, pCO_2, SST, SSS, surface DIC, and surface TA). Thereby we make sure that the same region is considered for all variables over the whole seasonal cycle but also over the whole observational period (see **Fig.1**).

2.2. Temporal filtering of RECCAP2 products

In general, the monthly mean pCO_2 products and GOBMs considered here can be expected to represent pCO_2 seasonality modulations that are sustained through the combined effects of the invasion flux of C_{ant}, natural variability, and warming. In order to identify the amplitude of the seasonal cycle (with its modulations), we follow Landschützer et al. (2018) in using a quadratic polynomial fit to remove the decadal trend from monthly time series over 1985-2018. Our analysis through the majority of this manuscript characterizes multi-decadal changes in pCO_2 seasonal variations by considering differences between the five-year intervals 1985-1989 and 2014-2018. We also investigated the degree to which the main results are sensitive to the choice of five-year versus 10-year versus 15-year intervals for describing climatologies (**Fig. S3**), and upon finding that the results are relatively insensitive to the approach we opted to use the difference between the two five-year intervals 1985-1989 and 2014-2018. As such, our approach is consistent with that used by Landschützer et al. (2018), who also used five-year climatologies in calculating decadal changes.

2.3. Surface observation-based products of pCO_2, DIC, and TA

Observation-based pCO_2 products that are compared for their representation of pCO_2 seasonality are listed in **Table 2**. All of these products are built on surface ocean pCO_2 measurements within the Surface Ocean CO_2 Atlas database (SOCAT, Bakker et al., 2016) yet they differ significantly in the way they spatiotemporally interpolate or map the sparse observations. Methodologically they include multiple linear regression (Iida et al., 2021), gradient boosted decision trees (Gloege et al., 2022), neural networks (Chau et al., 2022; Landschützer et al., 2016; Zeng et al., 2022), ensembles of various machine learning approaches (Gregor et al., 2019; Gregor and Gruber, 2021), and a Bayesian approach that is additionally constrained by mixed-layer dynamics (Rödenbeck et al., 2013, 2022). Additionally, one neural network product applies adjustments to the SOCAT data to account for temperature gradients between the ocean surface and the depth of the seawater intake on the observing ships and for the cold skin layer effect (Watson et al., 2020).

Of central importance to our study is that three of these products (JMAMLR, OceanSODA-ETHZ, and CMEMS-LSCE-FFNN) additionally provide time-varying surface DIC and TA products spanning 1985-2018. While we use all available pCO_2 products listed in **Table 2** for our analysis of seasonal cycles of CO_2-fluxes and pCO_2, our analysis greatly benefits from using these three products to attribute changes of pCO_2 seasonality to its drivers. We will refer to them as the pCO_2/TA products. We provide a summary of how DIC and TA are derived for these three pCO_2 products in the **Supplementary Materials**, but we refer the reader to the papers cited in **Table 2** for a more complete description of methods for the individual observation-based products.

2.4. Three-dimensional DIC climatologies

For our evaluation of seasonal variability in surface DIC concentrations, we consider two three-dimensional DIC climatologies constructed from observational products: the Mapped Observation-Based Oceanic DIC (MOBO-DIC) product by Keppler et al. (2020a, 2020b), and the NNGv2LDEO monthly climatology of interior DIC by Broullón et al. (2020). Unlike the pCO_2/TA products, these products are based on direct observations of DIC and as such provide an independent estimate of surface DIC seasonality, with the caveat that they offer a climatological view only. Both of these three-dimensional DIC climatologies are described in greater detail in the **Supplementary Materials**.

2.5. Global Ocean Biogeochemistry Models (GOBMs)

Global ocean biogeochemistry models (GOBMs) are compared against the pCO_2 products for modulations of CO_2 fluxes and pCO_2 for the six aggregated biomes over the period 1985-2018. Many of the GOBMs considered here have contributed to the Global Carbon Project's estimate of the ocean carbon sink (Friedlingstein et al., 2022), and have been evaluated by Hauck et al. (2020). Both the phase and amplitude of seasonal variability in the GOBMs will be evaluated against the pCO_2 products, as will the behavior of the drivers (SST, DIC, SSS,

and TA). The GOBMs are listed in **Table 3**, and they are further described for their initialization, forcing, and resolution in the submitted global RECCAP2 study of DeVries et al. All but one of the GOBMs listed in **Table 3** provide the full suite of variables and timescales needed for this analysis. The exception is the CCSM model for which output is available only through 2017 (rather than 2018). For this model alone we construct climatologies over 2014-2017. Additionally we have included the abiotic data-assimilation model OCIM (DeVries, 2014, 2022) where appropriate in our analysis. Although more commonly applied to the uptake of anthropogenic carbon, the abiotic nature of the OCIM model is of value as an endmember case in evaluating potential biotic biases in the GOBMs.

Air-sea heat fluxes for the GOBMs used throughout RECCAP2 are calculated with bulk formulae following the protocols of Large and Yeager (2009). This method does not impose a specific nudging or restoring of simulated sea surface temperature (SST) to observed SST, but rather imposes a negative feedback to SST through heat fluxes determined using observed surface boundary layer atmospheric temperatures. In this way, the simulation of seasonal variations in SST shows strong fidelity to observations when aggregated over biome scales.

2.6. Attribution Analysis

2.6.1 Attribution of drivers of the climatological seasonal cycle in pCO_2

The first stage of the attribution analysis has the goal of identifying the mechanisms responsible for discrepancies between pCO_2 products and GOBMs in representing the climatological seasonal cycle of pCO_2. We will consider both a decomposition into thermal and nonthermal drivers, using the analysis methods presented by Fassbender et al. (2022). The thermal/nonthermal decomposition provides a valuable means to identify spatially regions where seasonal SST variations are or are not the dominant driver of seasonal variations in pCO_2. We will also apply the Taylor Series decomposition method previously considered by Sarmiento and Gruber (2006). A Taylor Series decomposition is a more

extensive decomposition into individual drivers of the seasonal cycle in pCO_2, where we are specifically interested in parsing the contributions of SST, SSS, DIC, and TA. In this way we will evaluate any discrepancies that may call into question the fidelity of modeled pCO_2 to the real ocean. This analysis is possible for all GOBMs and the three observation-based products that include DIC and TA.

Additionally mixed layer depth (MLD) products will be used as part of our attribution analysis. For the sake of consistency with our choice of the relatively data-rich period 2014-2018 for evaluating climatologies of pertinent variables, we present a MLD product for this period 2014-2018 derived from the gridded monthly Argo product of Roemmich and Gilson (2009) for temperature and salinity. We define MLD by a density threshold through application of the MLD definition of Holte and Talley (2009).

2.6.2 Attribution of decadal changes in the seasonal cycle of pCO_2

The second stage of attribution analysis consists of applying the method of Fassbender et al. (2022) to identify the drivers of decadal changes in pCO_2 seasonality over 1985-2018. The method provides a means to separate the impacts of the invasion flux of anthropogenic carbon from the atmosphere from other climate signals that can modulate the seasonal cycle in pCO_2. More specifically, the goal for this work will be to identify the direct impact of an increase in the anthropogenic carbon (C_{ant}) content (i.e., a decrease of the surface ocean buffering capacity) relative to climate change and natural variability impacts on pCO_2 seasonality changes over 1985-2018. The original application by Fassbender et al. (2022) was for 21st century LE projections with an ESM, where the ensemble mean was applied to identify the forced component of change. Here our intention is to apply the method to the period 1985-2018 for all GOBMs (**Table 3)** and gridded pCO_2 products that include associated monthly DIC and TA fields along with SST and SSS. A description of the method is provided in the **Supplementary Materials.**

2.7. Uncertainty analysis for detecting the anthropogenic signal

As in the study of Fassbender et al. (2022), we apply large ensemble (LE) simulations with ESMs to aid in our interpretation of forced changes in pCO_2 seasonality in the presence of non-negligible background variability. Whereas Fassbender et al. (2022) focused on centennial timescale projections and could rely on the ensemble mean to isolate forced signals, we are here faced with a different challenge of interpreting historical records for which we have only three out of nine pCO_2 products that are viable for attribution analysis, all aiming to represent the same individual realization experienced by the chaotic Earth system. Thus, LE simulations will be applied to interpret changes measured over the historical period 1985-2018 to estimate uncertainty in isolating a forced change in the presence of natural background variability.

The LE models considered here are listed in **Table 4**. The first set of models were run under CMIP5 protocols using historical/RCP8.5 forcing (CanESM2, ESM2M, and CESM1) and the second set were run under CMIP6 protocols with historical/SSP3-7.0 forcing (CanESM5 and CESM2). Such a mix of CMIP5 and CMIP6 is appropriate to our interest in the historical period spanning 1985-2018, as the total radiative forcing component for the CMIP5 and CMIP6 forcing pathways is very similar through 2018 (Riahi et al., 2017). These LE outputs are not part of the resources made available through RECCAP2, but were rather collected by the authors through a modest expansion of the collection of LE models considered by Schlunegger et al. (2020) and Gloege et al. (2021). We are particularly interested in evaluating confidence levels for emergent changes between the time intervals 1985-1989 and 2014-2018, where the ensemble mean changes (signal) and natural variability in the changes (noise) provide a means to identify the signal-to-noise ratio (SNR) to characterize the degree of emergence or detectability.

For the attribution of decadal changes in pCO_2 seasonal amplitude, we have applied the CESM2-LE, as this was deemed to have better correspondence with climatological pCO_2 variability over biome scales than the other models (this will be addressed in **Fig. 12a**). The

394 application of CESM2-LE will allow us to address the degree of confidence that we have in
395 distinguishing the impact of the invasion flux of anthropogenic carbon from climate-driven
396 perturbations. CESM2-LE is also applied to identify the degree to which thermal and
397 nonthermal drivers of pCO_2 seasonality changes are emergent.

398

399 **2.8. CMIP6 models**

400

401 This study also includes analyses of 11 CMIP6 ESMs that are evaluated for their agreement
402 with the pCO_2 products over biome scales, with the models listed in **Table 6**. As ESMs are
403 used for future projections of the ocean carbon sink, it is of interest to assess their fidelity in
404 reproducing the seasonal cycle and its underlying processes. The CMIP6 models are not
405 intended to correspond to coupled versions of the GOBMs considered here, but our goal is
406 rather to identify similarities or discrepancies between these models, the GOBMs, and
407 observational pCO_2 products. For the CMIP6 models we have opted to focus on a slightly
408 different period, namely the five years (2010-2014) at the end of the historical component of
409 CMIP6 simulations, rather than the 2014-2018 interval considered for the GOBMs.

410

411 **3 Results**

412

413 **3.1. Overview of Multi-Decadal Changes in CO_2 Flux and pCO_2 seasonality**

414

415 The evolution of air-sea CO_2 flux seasonality, considered as averages over the six biomes, is
416 shown in **Fig. 1** as time series of the annual minimum and annual maximum of the monthly
417 air-sea CO_2 fluxes for the pCO_2 products and GOBMs. Here, we have chosen to show the
418 maximum and minimum of the fluxes to represent the full range of the seasonal cycle. One
419 should keep in mind that the across-product ensemble spread also includes the impacts of
420 wind speed on gas exchange that are not treated the same way across products (more details
421 are provided in the submitted DeVries et al. global ocean contribution to RECCAP2).

422

A prominent feature in **Fig. 1** is that the amplitude of the seasonal cycle in CO_2 fluxes is consistently larger for the GOBMs than it is for the pCO_2 products, across all biomes (see also **Fig. S1)**. From the RECCAP2 GOBMs alone it is not possible to determine the degree to which these internal disagreements reflect structural differences between the GOBMs and the degree to which it represents differences in forcing of the GOBMs. It is also worth noting that both the GOBMs and pCO_2 products exhibit a non-negligible degree of natural variability (interannual to decadal), for both the maxima and minima.

A decadal trend towards increased seasonal amplitude of biome-integrated CO_2 fluxes is evident over the subtropical biomes, as well as for NP-SPSS, whereas for NA-SPSS and SH-SS biomes this is less evident (especially in the pCO_2 products, see also **Fig. S1**). The increase in the amplitude, where it exists, can be accounted for mainly by a decrease of the annual minima (i.e., an increase of the uptake flux), whereas the annual flux maxima remained comparably constant over time. To better constrain whether there are discernable decreases in the spread amongst the pCO_2 products over 1985-2018 as pCO_2 observations increase, the biome-averaged pCO_2 for seasonal maximum and seasonal minimum are shown in **Fig. S2**, where although there is a decrease for both NA-SSS, SH-STPS, and SH-SS between 1985 and 2018, for the other biomes the changes are rather small. The broad-scale view of the evolution of CO_2 fluxes in **Fig. 1** serves to motivate much of the analysis that follows, with emphasis devoted to pCO_2 rather than CO_2 fluxes as a means to facilitate attribution and mechanistic understanding. Nevertheless we will return to CO_2 fluxes in the discussion of decadal trends in seasonal cycle amplitude.

3.1.1 Climatological seasonal cycle of pCO_2 and multi decadal changes

The climatological monthly pCO_2 seasonal cycle over 2014-2018 as a zonal mean is shown in **Fig. 2.** For the pCO_2 products (**Fig. 2a**), pCO_2 is highest in the subtropics in summer and highest in the Northern Hemisphere subpolar region and in the Southern Ocean in winter. The GOBMs (**Fig. 2e**) are in agreement with the pCO_2 products in their seasonal phasing in the subtropics but are in disagreement in the Northern Hemisphere subpolar regions and the

Southern Ocean. As a measure of the internal consistency across the nine pCO_2 products and the 11 GOBMs for this 2014-2018 climatology, the standard deviation is calculated month-by-month across the pCO_2 products (**Fig. 2b**) and across the GOBMs (**Fig. 2f**). From this we learn that the agreement across the pCO_2 products is robust (<10% disagreement relative to the annual cycle amplitude), whereas internal disagreements are much larger across the GOBMs (larger than 20% of the annual cycle amplitude at some locations), with the GOBMs diverging the most north of 30°N and south of 30°S. For the Northern Hemisphere subpolar regions, the disagreement in the GOBMs is largest in summer, and over the Southern Ocean it is largest in summer and in late winter.

We also consider the multi-decadal changes in the climatological monthly pCO_2 seasonal cycle between 1985-1989 and 2014-2018 for the pCO_2 products (**Fig. 2c**) and for the GOBMs (**Fig. 2g**). For both the pCO_2 products and the GOBMs (**Fig. 2c** and **Fig. 2g**, respectively), the meridional patterns of increases in seasonal amplitude to first order reflect and amplification of the climatological seasonal cycle in the Northern Hemisphere subtropical and subpolar biomes. However, this is less clear in the Southern Hemisphere subtropics and the Southern Ocean.

3.1.2 Spatial structure in the seasonal amplitude change

To understand the spatial structure of the amplitude change and the coherence between pCO_2 products and between GOBMs, maps of changes in the amplitude of the pCO_2 seasonal cycle between 1985-1989 and 2014-2018 are shown for the pCO_2 products in **Fig. 3a** and for the GOBMS in **Fig. 3b**. We use two definitions for the amplitude assessment: winter minus summer (JFM minus JAS for the Northern Hemisphere and JAS minus JFM for the Southern Hemisphere) in **Figs. 3a** and **3b** and climatological monthly maximum minus minimum in **Figs. 3c** and **3d**. For both the GOBMs and the pCO_2 products, regions where the multi-decadal trends are not significant (defined using a one standard deviation threshold) are stippled. From this we can see that the Northern Hemisphere has more significant changes than the Southern Hemisphere. Nevertheless for both hemispheres for GOBMs and pCO_2

products the broadest regions of significant changes are in the subtropics, although there is also a significant trend in the eastern subpolar North Pacific.

The two different definitions of seasonal amplitude (winter-minus-summer and maximum-minus-minimum) result in very similar large-scale patterns, although, due to their definition, with largely opposite sign. While for the maximum-minus-minimum definition positive changes always indicate an increase in seasonal amplitude, the winter-minus-summer amplitude is negative over the subtropical domain and positive in high latitudes, such that negative (positive) values for the multi-decadal amplitude change in **Fig. 3**a and **3b** over the subtropics (high latitudes) also indicate an amplitude increase. Phasing differences in seasonality are treated differently with the two definitions, since winter-minus-summer refers to fixed time intervals while the maximum and minimum can occur at any time throughout the year. While the winter-minus-summer definition highlights differences in phasing between pCO_2 products and GOBMs, it conceals some of the changes in the seasonal amplitude, specifically if the maximum or minimum of the seasonal cycle occurs outside of winter or summer months (as seen in **Fig. 3d** in the high latitude North Atlantic and North Pacific, where the discrepancy between GOBMs and pCO_2 products is much larger for the winter-minus-summer definition).

For the remainder of our analysis we will use the winter minus summer definition of seasonality due to its simplicity when it comes to analysis of multiple models and products, and also for consistency with previous work (e.g., Landschützer et al., 2018), keeping in mind that the specifics of this definition (the choice of JFM and JAS for defining seasonal amplitude) are sensitive to phasing differences between GOBMs and pCO_2 products. The sensitivity of the choice of five-year versus 10-year versus 15-year climatologies for the case of the pCO_2 products (**Fig. S3**) indicates that the results are robust to the length of the climatologies, the main difference being that using 10-year or 15-year climatologies shortens the effective decadal-change interval and weakens the signal of interest.

512 The fields shown in **Fig. 3a** and **3c** reveal important information about uncertainty in
513 detecting multi-decadal changes in pCO_2 seasonality using pCO_2 products. As all of the
514 products are based upon the same un-gridded SOCAT data product, differences in multi-
515 decadal changes shown in **Fig. 3a** and **3c** are due to mapping differences rather than
516 differences in the basis data itself. As such, the stippled regions indicate where mapping
517 uncertainty is large relative to resolved decadal changes. We interpret mapping uncertainty to
518 be a reducible variety of uncertainty, in that with improved data coverage and expansion of
519 the ocean observing system the products should be expected to converge.

520

521 For the GOBMs (**Figs. 3b** and **3d**) the regions of significance are very similar to what is
522 shown for the pCO_2 products, but the underlying reasons for uncertainty are of course
523 fundamentally different. For the GOBMs, regions where trends are not significant reflect the
524 combined effect of structural differences between models and differences in GOBM forcing
525 (described in the submitted global RECCAP2 contribution of DeVries et al. for differences in
526 forcing). The uncertainty in **Fig. 3b** and **3d** for the GOBMs should also be considered as a
527 reducible variety of uncertainty.

528

529 Nevertheless it should also be noted that for both pCO_2 products and GOBMs that it is the
530 subtropics where the thermal component of pCO_2 seasonality has the weakest opposition from
531 the nonthermal component that there is emergence. Thus both mapping uncertainty and
532 presumably structural uncertainty with GOBMs are mostly problematic in regions where the
533 nonthermal drivers become important. This will be discussed further in subsequent analyses
534 of this study.

535

536 **3.1.3 Biome aggregated climatologies**

537

538 Climatological monthly anomalies in pCO_2 and its primary drivers, SST and surface DIC,
539 relative to their annual means are displayed in **Fig. 4** as (area-weighted) averages across the
540 RECCAP2 biome regions. A first comparison between the full collection of pCO_2 products

(blue) and all GOBMs (green) is shown in the first column of **Fig. 4** by biome region, where continuous lines and associated shading represents the mean and one standard deviation, respectively. Our first objective is to identify discrepancies between the GOBMs and the pCO_2 products, with such discrepancies to be addressed subsequently in the **Attribution** section of the paper.

In broad terms, the seasonal phasing agreement between GOBMs and pCO_2 products is best in subtropical biomes (NH-STSS, NH-STPS, and SH-STPS) and worst in the Northern Hemisphere subpolar and the Southern Ocean biomes (NA-SPSS, NP-SPSS, and SH-SS). In the NA-SPSS and NP-SPSS biomes, GOBMs consistently represent seasonal pCO_2 minima that occur earlier than in the pCO_2 products, and that are weaker for NA-SPSS. For NA-SPSS and NP-SPSS, after the spring minimum in pCO_2 in the GOBMS there is an increase towards a maximum in August, whereas the pCO_2 products remain low throughout the summer before increasing in autumn and winter towards a maximum in January/February. Analogous to what is found in the Northern Hemisphere subpolar biomes, there are also discrepancies in phasing for the GOBMs relative to the pCO_2 products for SH-SS. For the higher latitude regions where phasing in models diverges greatly from that seen in the pCO_2 products, it is widely understood that the early summer minimum in pCO_2 (as seen in pCO_2 products) is directly related to biological drawdown of DIC (Gregor and Gruber, 2021). It is a known bias of coupled models that primary production is often not realistically sustained through summer after a pronounced spring bloom. This has been shown in the North Atlantic (Goris et al., 2018), and more broadly for the high latitudes of both hemispheres (Cabré et al., 2016; Mongwe et al., 2018; Nevison et al., 2016), and the same limitation appears to be pertinent in our study.

In the subtropical biomes, on the other hand, the GOBMs consistently simulate a pCO_2 seasonal cycle that is larger than what is seen in the pCO_2 products (**Table 5**). For NH-STSS the amplitude averaged across the GOBMs is 80% larger than for that averaged across the pCO_2 products, for NH-STPS it is 26% larger, and for SH-STPS it is 34% larger. This occurs with phasing that is largely consistent between the GOBMs and pCO_2 products. As seen in **Fig. 4** (second column), this discrepancy in the amplitude of pCO_2 variations does not reflect

biases in the seasonal amplitude of SST variations, as the thermodynamic boundary conditions for forcing the GOBMs result in SSTs that have relatively strong fidelity to observations when averaged over biome scales. Rather, the discrepancy in the amplitude of the pCO_2 seasonal amplitude indicates that surface DIC (**Fig. 4**, second column) as the main driver of the nonthermal component of pCO_2 seasonality is not providing sufficient counterbalance to the realistic thermal component of seasonal forcing (i.e., the seasonal amplitude seems to be too small in GOBMs). For the subtropical biomes it is worth noting that the OCIM model (**Fig. 4**, thin line) has an even larger pCO_2 seasonal amplitude than the GOBMs. The OCIM model has a realistic SST seasonal evolution (not shown), but simulates only circulation- and surface flux-driven DIC variations without including a contribution of the biological drawdown of DIC. The OCIM pCO_2 and DIC seasonal cycle amplitude discrepancies relative to the GOBMs provide an estimate of the contribution of the biological pump to DIC and pCO_2 seasonality.

The fact that the DIC seasonal amplitude is weaker for the GOBMs relative to the pCO_2 products means that the nonthermal component of pCO_2 seasonality is smaller. Over the subtropical regions, this will serve to enhance the thermal dominance of seasonal pCO_2 variations and in the subpolar and circumpolar regions this will reduce the nonthermal dominance of seasonal pCO_2 variations. This provides a means to alter the phasing of pCO_2 variations, although the degree to which this occurs will be modulated by the background mean state of DIC and TA (Fassbender et al., 2018). In all biomes, the DIC seasonal amplitude for GOBMs lies between that of the abiotic OCIM model and that of the pCO_2/TA products, suggesting that for the GOBMs there may be as-yet undetermined shortcomings in the representation of the seasonal processes that increase DIC (entrainment) and decrease DIC (net biological consumption of DIC).

Comparing the decadal changes (**Fig. 4**, right column) with the climatologies over 2014-2018 (left column), we see again that the decadal changes in pCO_2 to first order amplify the climatological seasonal cycle in the Northern Hemisphere as well as for SH-STSS, consistent with what was identified in the Hovmöller diagrams in **Fig. 2**. Importantly, the pCO_2 products show significantly less internal disagreement for the climatological seasonal cycle (left

603 column of **Fig. 4** and **Table 5**) than the GOBMs. Yet, for the decadal changes (right column
604 of **Fig. 4**), the spread across the GOBMs and across the pCO_2 products is similar (one
605 standard deviation for the biome averaged seasonal amplitude changes are roughly between 1
606 and 10 ppm, **Table 5**). While this is of the same order of magnitude as for their seasonal
607 amplitude for the pCO_2 products, GOBMs show significantly less internal disagreement for
608 the decadal change than for the seasonal amplitude. This indicates that the processes
609 responsible for the increase in seasonal pCO_2 amplitude are relatively well represented in
610 GOBMs We hypothesize here that the pertinent process in the GOBMs is the invasion flux of
611 C_{ant} dominating pCO_2 seasonality modulations associated with climate-driven changes in the
612 state of the ocean, a hypothesis to which we will return in the **Attribution** section. The best
613 agreement for decadal changes in the pCO_2 seasonal amplitude occurs in the subtropical
614 biomes, consistent with **Fig. 2**. For NH-STSS, the GOBMs show a mean net increase in the
615 seasonal amplitude of 10.7 μatm and the pCO_2 products of 9.8 μatm, with the difference in
616 their increase being less than 10%. For NH-STPS, the mean net increase in the seasonal
617 amplitude for the GOBMs and pCO_2 products are the same at 6.3 μatm. For SH-STPS the
618 increase for GOBMs is 2.7 μatm, which is approximately half of the mean pCO_2 product
619 increase of 5.3 μatm. It can also be seen in **Table 5** that the relatively consistent ranges of
620 change over the subtropical biomes between GOBMs and pCO_2 products are approximately
621 within each other's uncertainty range.

622

623 **3.2. Attribution**

624 Having evaluated the seasonal cycle of pCO_2 in terms of its phasing and amplitude, as well as
625 related discrepancies between the pCO_2 products and the GOBMs, we now turn our attention
626 to attribution of the drivers. We have already inferred from the biome-aggregated analyses in
627 **Fig. 4** that DIC should be explored as having a potential first-order role in modulating the
628 differences between pCO_2 products and GOBMs in the pCO_2 seasonal cycle by serving as the
629 main nonthermal driver.

630

631 **3.2.1 Spatial patterns of the seasonal cycle in surface DIC concentrations**

632

633 The spatial patterns for the surface DIC seasonal cycle amplitude (winter minus summer,
634 climatology over 2014-2018) for the pCO_2/TA products is shown in **Fig. 5a** (average across
635 JMAMLR, CMEMS-LSCE-FFNN, and OceanSODA-ETHZ) as well as for the GOBMs in
636 **Fig. 5b**. We see a good agreement between the amplitude of the surface DIC seasonal cycle
637 from pCO_2/TA products and the GOBMs for the overall patterns with maximum values seen
638 in the Northern Hemisphere subpolar domains. For the pCO_2/TA products we also see a
639 zonally-oriented local surface DIC maximum across 40°S-45°S that can be distinguished from
640 a local minimum over the Antarctic Circumpolar Current (ACC) region between 50°S-60°S,
641 with this feature being more weakly present in the GOBMs. The differences in the seasonal
642 amplitude of DIC (GOBMs minus pCO_2 products) in **Fig. 5c** indicates a negative bias of the
643 GOBMs that is relatively consistent over large scales, and that is particularly pronounced at
644 northern high latitudes .

645

646 The zonal average of the amplitude of the seasonal cycle (winter minus summer) in DIC is
647 shown in **Fig. 5d**. Additionally the amplitude of the surface ocean DIC seasonal variability
648 for the two three-dimensional DIC climatologies, namely MOBO-DIC and NNGv2LDEO are
649 also shown. The MOBO-DIC product tends to have a seasonal amplitude that is somewhat
650 larger than the surface DIC products over most latitudes, except over the Southern Ocean and
651 north of 50°N. NNGv2LDEO is also larger than the GOBMs over most latitudes, also with an
652 exception to the north of 50°N but not over the Southern Ocean.

653

654 The same collection of products considered as zonal means in **Fig. 5d** are shown as biome
655 averages in **Fig. S4**, along with the OCMIP product. This further illustrates that there is a
656 discrepancy between the weaker DIC seasonal amplitude of GOBMs relative to not only the
657 pCO_2/TA products but also to MOBO-DIC and NNGv2LDEO, although the seasonal DIC
658 amplitude of MOBO-DIC is smaller than that of all other observation-based products (and
659 thus closer to the GOBMs) in the high latitude biomes (NA-SPSS, NP-SPSS, and SH-SS).
660 Interestingly, for both large permanently stratified biomes (NS-STPS and SH-STPS) the late
661 summer seasonal minimum in DIC concentrations for the MOBO-DIC and NNGv2LDEO
662 products precedes that of the pCO_2/TA products.

3.2.2 pCO_2 seasonality differences between observational products and GOBMs

To systematically attribute discrepancies in the pCO_2 seasonal cycle between GOBMs and pCO_2 products to their drivers, we begin with an analysis of the relative importance of the thermal and nonthermal drivers of pCO_2 seasonal variability following the framework of Fassbender et al. (2022) (see the **Supplementary Materials** for a description). For this approach, in contrast to the widely applied deconvolution method of Takahashi et al. (1993, 2022), monthly pCO_2 deviations in a given year are considered relative to the pCO_2 value calculated from annual mean values of SST, SSS, DIC, TA, PO_4 and SiO_4 rather than relative to a direct mean of the monthly pCO_2 values, which could obscure seasonally asymmetric pCO_2 responses to its drivers.

Within this analysis we consider for each grid point the absolute value of the differences between the winter and summer seasonal averages over 2014-2018. The difference between the thermal and nonthermal pCO_2 amplitudes is shown for the observational products (**Fig. 6a**) and for the GOBMs (**Fig. 6b**). For both panels, positive values (red) indicate that the thermal pCO_2 component dominates the seasonal cycle amplitude and negative values (blue) indicate that the nonthermal component dominates for this climatological diagnostic.

We see consistency between the pCO_2 products (**Fig. 6a**) and the GOBMs (**Fig. 6b**) in that the thermal pCO_2 component is dominant over the subtropics, with this dominance being even stronger for the GOBMs. Over the northern subpolar gyres and the Southern Hemisphere circumpolar regions there is a pronounced disagreement between the pCO_2 products and the GOBMs. Specifically, for the pCO_2 products the nonthermal pCO_2 component is dominant in these biomes, while the GOBMs exhibit a relatively strong thermal component in these regions. These discrepancies between the pCO_2 products and GOBMs are also shown for each GOBM and pCO_2 product separately in **Fig. 6c**, revealing the relatively strong agreement between the pCO_2 products and the disparity between the GOBMs that was also in evidence in **Fig. 4** for pCO_2 itself averaged over biome scales.

As we have identified in **Figs. 4** and **5**, there is a systematic discrepancy between GOBMs and pCO_2 products, with GOBMs indicating a weaker climatological seasonal cycle in DIC variations, which is consistent with a more pronounced dominance of the thermal component of pCO_2 seasonality highlighted in **Fig. 6**. Next, we evaluate whether the nonthermal pCO_2 component discrepancy between GOBMs and pCO_2 products can be explained by the smaller DIC seasonal variability in the GOBMs.

We consider the drivers of the climatological pCO_2 seasonal cycle during 2014-2018 over the six aggregated biomes in **Fig. 7**. The left column shows pCO_2 climatologies for the pCO_2 products (blue) and the GOBMs (green). This serves as a reminder that over the NA-SPSS, NP-SPSS and SH-SS domains, there are fundamental discrepancies between the GOBMs and the pCO_2 products in their representation of both the phase and amplitude of pCO_2 seasonality, while in NH-STSS, NH-STPS, and SH-STPS regions the amplitude of the seasonal cycle of pCO_2 is consistently larger in GOBMs. In order to understand the cause of these discrepancies, a decomposition of the month-to-month changes in pCO_2 into its main drivers (SST, SSS, DIC, and TA) is presented in the second and third column of **Fig. 7**. For the pCO_2 products (**Fig. 7**, second column) the SST term dominates over the DIC term in the subtropics, while the DIC contribution is dominant in the subpolar biomes of the Northern Hemisphere and high latitude regions of the Southern Hemisphere. For each of these six biomes, we see that the GOBMs have a smaller DIC contribution (third column of **Fig.7**) when compared to the pCO_2 products (second column of **Fig. 7**).

It is worth noting for the observational pCO_2 products (second column in **Fig. 7**) that although the effect of the spring bloom in NA-SPSS is marked by a short DIC-driven minimum in the pCO_2 tendency in April, for NP-SPSS the DIC-driven pCO_2 tendency is sustained from April through July (emphasis on the blue DIC tendency line in each case). For the GOBMs (third column in **Fig. 7**) there is no sustained dominance of the DIC contribution relative to SST over most of the seasonal cycle for NA-SPSS and NP-SPSS. For both of these biomes the GOBMs simulate weak phytoplankton blooms in late spring as indicated by the DIC tendency

term for both cases, with the discrepancies in amplitude being larger than discrepancies in phase. This results in an SST dominance of the pCO_2 tendency through the summer months, thereby driving pCO_2 to peak 6-7 months earlier than that of the pCO_2 products for each of the two biomes. This represents the impact of the weaker representation of the seasonal amplitude of surface DIC variations for the GOBMs.

In the fourth column of **Fig. 7**, the difference between the GOBM contributions (third column) and the pCO_2 product contributions (second column) allows us to identify DIC discrepancies as the underlying term that leads to the principal different tendencies in pCO_2 seasonal amplitude over biome scales. In other words, over these aggregated scales the most important driver that causes the disagreement between the pCO_2 seasonal cycle of the GOBMs and the pCO_2 products lies in the processes that control DIC seasonality. It is important to emphasize that the GOBMs provide a distinct advantage over coupled ESMs in studying disagreements between modeled and observation-based pCO_2 seasonality, because their climatological seasonal evolution of SST is effectively imposed from observations. This allowed us to identify and understand the potential magnitude of pCO_2 seasonality biases that are imposed by a seeming systematic bias with GOBMs to underestimate the importance of DIC seasonality. It is worth recalling here that the DIC from the pCO_2/TA products is more consistent with the independent products (MOBO-DIC and NNGv2LDEO) than with the GOBMs (**Fig. 5d**), lending credence to the discrepancies highlighted in **Fig. 7**.

A candidate mechanism that could potentially account for why the GOBMs have smaller seasonal surface DIC variability than the DIC products could be in the modeled seasonal variability of biological drawdown of surface DIC. However, in addressing this question we are faced with the caveat that seasonal variability in biological drawdown of surface DIC over global scales is poorly constrained by observations. To shed light on this question, we consider in **Fig. 8** the relationship between climatological (2014-2018) surface salinity-normalized DIC (nDIC) variations and mixed layer depth (MLD) averaged over the six biomes. The MLD product is derived from Argo observations, described above. **Fig. 8** shows that MLD variations averaged across the GOBMs are smaller throughout the seasonal cycle than they are for the observational product. Additionally, during summer months when the

MLD becomes minimum, strong nDIC reductions are more pronounced in the observations than in the GOBMs. This suggests that the surface summer DIC drawdown, likely associated with biological drawdown of DIC, is underestimated in GOBMs. This could reflect a spurious exhaustion of nutrients by early summer in GOBMs. Investigating these questions further is not possible with the tools available through RECCAP2. However, given their importance for pCO_2, it is strongly advised that process understanding of the potential shortcomings of models in this regard be further investigated.

3.2.3. Attribution for decadal increases in pCO_2 seasonality

Here we adopt the framework of Fassbender et al. (2022) to address both mechanistically and quantitatively the drivers of enhanced pCO_2 seasonal amplitude. Specifically, this method allows one to deconvolve the relative importance of these drivers, namely the transient invasion flux of anthropogenic carbon (denoted as the C_{ant} contribution) and other drivers (denoted collectively as climate contribution). As the attribution methodology of Fassbender et al. (2022) requires not only surface pCO_2 but also surface DIC and TA concentrations (in addition to SST, SSS, PO_4, and SiO_4), we focus here on the three RECCAP2 pCO_2 products that include the necessary quantities, specifically JMAMLR, OceanSODA-ETHZ, and CMEMS-LSCE-FFNN, as well as the GOBMs listed in **Table 3**. For the observation-based products, monthly climatological PO_4 and SiO_4 fields were taken from World Ocean Atlas 2018 (Garcia et al., 2019).

We begin the analysis for this section on decadal changes in pCO_2 and CO_2 flux seasonality with a descriptive assessment of seasonal asymmetries in the changes in seasonal amplitude between 1985-1989 and 2014-2018 in **Fig. 9**. pCO_2 anomalies are shown relative to the annual mean value computed from annual means of SST, SSS, DIC, TA, and nutrients ($pCO_{2\,AM}$) for both observationally-based products and GOBMS, following the method described in Fassbender et al. (2022). Calculations are performed separately for each year and then averaged over the time intervals 1985-1889 and 2014-2018. This provides an estimate of the annual mean if pCO_2 were to respond linearly to its individual drivers over the seasonal cycle,

784 making it possible to identify seasonally asymmetric changes in pCO_2 that are obscured when
785 computing a mean of monthly pCO_2 values over an annual cycle.

786

787 We first consider the case of the subtropics as approximately 15°N-40°N and 15°S-40°S,
788 where summer anomalies of pCO_2 for 1985-1989 (**Fig. 9a**) and 2014-2018 (**Fig. 9b**) are
789 larger for the GOBMs than for the pCO_2 products, reflecting discrepancies in the amplitude of
790 DIC seasonality between the GOBMs and observation-based products discussed previously
791 (**Fig. 5d**). Importantly, between 25°N-40°N and 25°S-40°S the summer anomalies are larger
792 than the winter anomalies over both time intervals. For the difference between the 2014-2018
793 and 1985-1989 intervals (**Fig. 9c**), we see that over the Northern Hemisphere subtropical
794 latitudes the summer changes are larger than the winter changes. In other words, notable
795 asymmetry can be identified over the Northern Hemisphere subtropics with larger increases in
796 summer highs than decreases in winter lows. North of 45°N there are relatively symmetric
797 changes in summer and winter for the observation-based products and the GOBMs, but the
798 changes for the two product classes are of reverse sign (see next paragraph) and larger for the
799 pCO_2 products. The changes for the Southern Hemisphere are less pronounced, with some
800 degree of asymmetry over 10°S-25°S where for the observation-based products the winter
801 lows decrease more than the summer highs increase. There is no discernable asymmetry over
802 the Southern Ocean.

803

804 The disagreement between the GOBMs and pCO_2 products, both for seasonal pCO_2
805 anomalies (**Fig. 9a,b**) and their changes (**Fig. 9c**), is largest in the northern subpolar latitudes
806 (45°N-60°N). For both the 1985-1989 and 2014-2018 climatologies, the pCO_2 products show
807 relatively strong positive pCO_2 anomalies in winter, and relatively strong negative pCO_2
808 anomalies in summer, reflecting the interplay between winter convective mixing and warm-
809 season export production in this region where nonthermal pCO_2 effects are dominant. In
810 contrast, over the same region the anomalies for pCO_2 in GOBMs are relatively small in both
811 winter and summer, reflecting the near balance between thermal and nonthermal pCO_2 cycles.
812 Although it is not explicitly shown here, it is important to keep in mind that **Fig. 2** and **Fig. 4**
813 revealed that there are discrepancies in the phenology or phasing of seasonal variations
814 between the GOBMs and pCO_2 products, such that the results with the GOBMs are sensitive

to the specific definition of the seasonal cycle amplitude with pCO_2 products showing indeed the largest seasonal change in winter and summer for 45°N-60°N, while GOBMs show the largest change in early spring and late summer/early autumn (**Fig. 2** and **Fig. 4**). For the Southern Hemisphere region between 45°S and 60°S, the GOBMs and pCO_2 products are much more similar than they are over the Northern Hemisphere subpolar regions over both 1985-1989 and 2014-2018, with relatively modest decadal changes for the northern subpolar regions where nonthermal pCO_2 drivers are larger than thermal pCO_2 drivers for the pCO_2 products.

The corresponding asymmetries in zonally-integrated seasonal CO_2 fluxes, shown in **Fig. 9d-9f**, are quite different from what was seen for surface pCO_2 anomalies. For both time periods 1985-1989 and 2014-2018, seasonal CO_2 fluxes are larger over the subtropics in winter (ingassing) than in summer (outgassing), which indicates that seasonal wind speed asymmetries more than compensate the summer-skewed pCO_2 seasonal asymmetry over the same latitude range (Fassbender et al., 2022). This is consistent with the winter CO_2 fluxes showing local extrema for ingassing near 40°N and 40°S where westerly winds exhibit meridional maxima. This feature is also found in the 1985-1989 to 2014-2018 decadal change. For the Northern Hemisphere subpolar regions spanning 45°N-60°N, the seasonal amplification in CO_2 fluxes between 1985-1989 and 2014-2018 shows enhanced ingassing during summer for the pCO_2 products, whereas the GOBMs show enhanced winter uptake over these latitudes. For the circumpolar regions of the Southern Hemisphere spanning 45°S-60°S, both the GOBMs and the pCO_2 products broadly exhibit enhanced ingassing in summer (JFM) and winter (JAS) seasons relative to the 1985-1989 period.

We next turn our attention in **Fig. 10** to deconvolve the role of C_{ant} invasion and climate perturbations (e.g., changes to the ocean physical or biogeochemical state caused by anthropogenic climate change) in driving multi-decadal changes in pCO_2 seasonality between 1985-1989 and 2014-2018. The changes in the subtropics are qualitatively similar in the pCO_2 products and GOBMs (top and model rows of **Fig. 10**), with the changes in the total seasonal cycle amplitude (**Fig. 10a**) dominated by the C_{ant} invasion impact on the thermal component with a small climate-driven increase in the thermal pCO_2 component (**Fig. 10b**).

However, for the subpolar regions of the Northern Hemisphere and the Southern Ocean, the pCO_2 products show that the nonthermal pCO_2 component changes driven by climate perturbations (**Fig. 10c**) are sufficiently large to dominate the total response in these regions (**Fig. 10a**), a feature that is not seen (or considerably weaker) for the GOBMs. C_{ant}-induced declines in carbonate buffering in the high latitudes also work to slightly amplify the total nonthermal pCO_2 seasonal cycle changes in both the pCO_2 products and GOBMs (red lines in right column).

For the total change in the GOBM pCO_2 values (**Fig. 10d**), the impact of climate perturbations is relatively minor so that the change in pCO_2 seasonality is largely dominated by the invasion flux of C_{ant}. For the thermal component of pCO_2 changes in the GOBMs, both the subtropical and subpolar latitudes of the Northern Hemisphere indicate dominance of the effect of transient C_{ant} invasion, with the Southern Ocean posing one region where this is neutralized by climate perturbations. For the nonthermal component of pCO_2 changes in the GOBMs, the impact of C_{ant} invasion is relatively minor, so that the changes are dominated by climate perturbations, which are also small. In summary, for the GOBMs, increases in the total pCO_2 seasonal cycle amplitude are dominated by the direct influence of C_{ant} on the thermal pCO_2 component seasonal cycle amplitude through the enhanced temperature sensitivity associated with elevated ocean pCO_2 values.

3.3. Estimating Irreducible Uncertainty in Seasonal Cycle Amplitude Changes

We now turn our attention to the emergence of decadal changes in pCO_2 seasonality, with applications at the gridoint, zonal mean, and biome scales.

3.3.1 Natural variability uncertainty in detecting forced changes in pCO_2 seasonal amplitude

As was emphasized in the study of Landschützer et al. (2018), natural variability in the seasonal amplitude of pCO_2 variations can obscure detection of anthropogenic trends, an effect that can be termed natural variability uncertainty. For sea surface pCO_2, the signal (**Fig. 11a**) and the signal-to-noise ratio (SNR) (**Fig. 11b**) are calculated for a single LE, to illustrate patterns of emergence. We choose here the CESM2 model (Danabasoglu et al., 2020) for which the phasing of the pCO_2 seasonal cycle over the Northern Hemisphere subpolar biomes has the best correspondence with the observation-based products out of the LE simulations described in **Table 4** or the CMIP6 models shown in **Table. 6**.

According to the CESM2-LE, the pCO_2 seasonality increases are most emergent (|SNR|>1) (**Fig. 11b**) at the grid point level over much of the subtropical Northern Hemisphere, as well as over a band spanning the subtropical convergence regions of the Southern Hemisphere. Large parts of the North Atlantic subpolar gyre exhibit a decrease in the amplitude of seasonal pCO_2 variations. This analysis is indicative of pCO_2 seasonality changes over the Southern Ocean being non-emergent above the noise level of natural variability at the grid point level over our three-decade interval. In particular, pCO_2 seasonality changes in the Antarctic Circumpolar Current region spanning 50°S-60°S are non-emergent, along with some parts of the Southern Hemisphere subtropics.

We next consider the emergence characteristics for the underlying thermal and nonthermal drivers of pCO_2 seasonality as represented by the large ensemble model. We see that the forced decadal change (ensemble mean) for the thermal component (**Fig. 11c**) and nonthermal component (**Fig. 11e**) are both considerably larger than the decadal change for the full pCO_2 field itself (**Fig. 11a**). For the resultant signal-to-noise ratio, we see that the patterns for the thermal component (**Fig. 11d**) and the nonthermal component (**Fig. 11f**) are spatially offset from each other, and when considered together help to account for the relatively restricted regions over which there is local grid point emergence, predominantly over the thermally dominated subtropical domain, for the pCO_2 seasonal cycle. From these analyses, we can see that within the subtropics, the emergent regions for total pCO_2 SNR (|SNR|>1 in **Fig. 11a**) correspond to the regions where the ensemble mean nonthermal component (**Fig. 11e**) is small.

905

906 **3.3.2 Interpretation of results of attribution analysis**

907

908 Having visualized the patterns of emergence for pCO_2 seasonality changes in **Fig, 11** we
909 redirect out attention to the last row of **Fig. 10** (panels **10g-10i**), where the same set of 50
910 large ensemble members with the CESM2-LE are applied to interpret the zonal mean changes
911 in the pCO_2 products (first row of **Fig. 10**). The shading for the LE results represents natural
912 variability uncertainty (one standard deviation about the 50-ensemble-member mean), while
913 the shading for the pCO_2 products (**Figs. 10a-10c)** can be interpreted to represent mapping
914 uncertainty. These forms of uncertainty are distinct, but can be used together to assess the
915 degree to which the C_{ant} and climate-driven signals for the pCO_2 products are detectable. We
916 consider the means of the pCO_2 products in **Figs. 10a-10c** to be "best estimates" of the
917 decadal changes. Superimposing the envelope of natural variability from the LE analysis
918 (**Figs. 10g-10i**) onto the pCO_2 product means would suggest that the C_{ant} and climate driven
919 signals are emergent when they and their associated natural variability are separated from
920 zero for their decadal change.

921

922 Under this framework, we interpret the C_{ant} component of the pCO_2 product changes to be
923 detectable for all regions and pCO_2 components (pCO_2, $pCO_{2\ T}$, and $pCO_{2\ NT}$). What is more
924 surprising and compelling with the pCO_2 products is the fact that the climate driven changes
925 over the Northern subpolar domains, with much of this signal found in the nonthermal
926 component, cannot be explained by natural variability according to our CESM2-LE results.
927 Further attribution of this climate-driven signal (mixing versus biology, for example) is
928 beyond the scope of this study, but at the very least this underscores the importance of
929 sustained seasonally-resolving observations in high latitude regions to better constrain and
930 understand this behavior.

931

932 Taken together, the attribution analysis in **Fig. 10** and the analyses of pCO_2 and CO_2 flux
933 seasonal asymmetries in **Fig. 9** indicate that, over the broad areal extent of the subtropics, the
934 pCO_2 seasonal amplitude increases with an asymmetric larger increase in summer are in large

935 part due to the C_{ant} impact on the thermal driver of seasonal amplitude. Through the effect of
936 stronger wind speeds in winter than summer, the seasonal CO_2 flux asymmetry becomes even
937 larger and of opposite sign over the subtropics, with large increases in winter ingassing. Over
938 the broad expanse of the subtropics, the agreement between the pCO_2 products and GOBMs,
939 together with the clear emergence indicated by the LE, gives us reasonable confidence for
940 both the driver (C_{ant}) and the asymmetry of pCO_2 seasonality changes and elevated winter
941 CO_2 uptake. However, for the high northern latitudes, pCO_2 products and GOBMs disagree
942 on the drivers of the changing pCO_2 seasonality. Here, the products indicate that a rather large
943 climate forcing is responsible for pCO_2 seasonal cycle changes.

944

945 **3.3.3 Emergence of forced trends with biome aggregation**

946

947 We next address the degree to which biome aggregation improves the emergence of pCO_2
948 seasonality trends between 1985-1989 and 2014-2018. To this aim, we use multiple LE
949 simulations with five different ESMs (detailed in **Table 4**), and apply them to interpret the
950 decadal changes in pCO_2 seasonal variations represented by the pCO_2 products. However,
951 before considering multi-decadal trends we consider first in **Fig. 12a** an analysis for the six
952 aggregated biomes of the simulated seasonal amplitude of pCO_2 variations for a climatology
953 over 2014-2018, both for pCO_2 products and LEs, with uncertainty ranges indicated for each
954 case. For the observation-based pCO_2 products, the uncertainty shown represents the
955 uncertainty across the nine pCO_2 products themselves, which is reflecting the spread across
956 methods (mapping uncertainty) in representing gridded pCO_2. For an individual LE, the
957 uncertainty represents the range of natural variability represented by the collection of
958 individual ensemble members for that specific LE. We see that for all six aggregated biomes,
959 at most, two of the five LEs have a climatological seasonal amplitude (defined as the absolute
960 value of JFM-JAS) where the first quartile range (25%-75%, solid bar) overlaps with the first-
961 to-third quartile range of the pCO_2 products. Over four of the six biomes (NP-SPSS, NH-
962 STPS, SH-STPS, and SH-SS) CESM2-LE overlaps with the pCO_2 products, thereby
963 indicating correspondence. We also see that inter-model differences in seasonal amplitude
964 (ensemble median) are much larger than the ensemble spread (natural variability) for the
965 individual ESMs. Overall, the analysis in **Fig. 12a** indicates that the representation of the

966 climatological seasonal amplitude of pCO_2 in LEs is partly inconsistent with the pCO_2
967 products, mirroring what was found for GOBMs in the first part of the **Results** section of this
968 study.

969

970 On the other hand, the decadal changes in the amplitude of seasonal pCO_2 variations between
971 1985-1989 and 2014-2018 (**Fig. 12b**) reveal a much better agreement (relative to **Fig. 12a**)
972 between the median of the observational products and the ensemble spread of the individual
973 LEs. Most importantly, with one exception over the three subtropical biomes (NH-STSS, NH-
974 STPS, SH-STPS) and for each LE within these regions, the range of outcomes for modeled
975 pCO_2 seasonality changes (the range indicated by the whiskers) does not intersect with a zero
976 trend or go negative. Thus in the subtropics the biome-aggregated changes in the seasonal
977 amplitude of pCO_2 are predominantly emergent, with SH-SS also being largely emergent. For
978 the NP-SPSS biome, the median decadal change calculated for each LE indicates an increase
979 in pCO_2 seasonal amplitude, although one of the LEs is not emergent while two other LEs are
980 near the one standard deviation threshold for emergence. This is indicative of the NP-SPSS
981 being moderately emergent under aggregation.

982

983 For the NA-SPSS biome the decadal changes in pCO_2 seasonal amplitude are quite distinct
984 from the other regions, in that all LEs are at least moderately emergent, but that they have
985 divergent signs in their simulated decadal changes. Three of the LEs (CESM1, CESM2, and
986 ESM2M) exhibit a decrease in pCO_2 seasonal amplitude, while two of the LEs (CanESM2
987 and CanESM5) exhibit an increase. Under the caveat that we have imposed a somewhat
988 restrictive definition of the seasonal cycle that is optimally suited for the pCO_2 products (see
989 **Fig. 2** and **Fig. 4**), the at least moderately emergent decrease in pCO_2 seasonal amplitude for
990 three LEs is distinctive for the NA-SPSS biomes. The study of Goris et al. (2022) suggests
991 that such behavior may be expected from the disparate responses of the Atlantic Meridional
992 Overturning Circulation (AMOC) for the LEs. However, further exploration of this point
993 should be done while taking into consideration the sensitivity of the models to the definition
994 of the seasonal cycle. It is interesting that one of the pCO_2 products does show zero net
995 change between 1985-1989 and 2014-2018.

The fact that the distribution of multi-decadal trends for individual LEs overlaps with the 25%-75% (bar) range for the observation-based pCO_2 products gives us a degree of confidence that the biome-aggregated changes can be considered emergent or detectable over this 30-year period. It should be noted, however, that the Northern Hemisphere biomes tend to be faced with a triple-whammy of elevated uncertainty, given the relatively high degree of disaccord between pCO_2 products (mapping uncertainty), the relatively elevated level of natural variability uncertainty, and the offset of the medians of the different LEs (model structural uncertainty). The LEs nevertheless bring great value to the parsing of uncertainty in that they allow us to distinguish between internal variability uncertainty and model structural uncertainty. Qualitatively they are of similar amplitude for the decadal changes (**Fig. 12b**), but the model structural uncertainty is much larger for the 2014-2018 climatology (**Fig. 12a**).

The Southern Ocean (SH-SS) region is characterized by relatively weak trends **(Fig. 12b**), yet due its relatively weak natural variability is also predominantly emergent at the biome scale despite being non-emergent at the gridpoint scale (**Fig. 11b**). The reason for there being both weak natural variability and a weak decadal trend over the Southern Ocean is due to the combined effects of the tendency of models to have a relatively weak dominance of thermal over nonthermal seasonality drivers over the Southern Ocean, and that the relatively small amplitude of seasonal SST variations over the Southern Ocean. Taken together, this limits the ability of the invasion flux of C_{ant} to boost pCO_2 seasonality amplitude between the 1980s and 2010s.

4 Discussion

The unprecedented collection of pCO_2 products and model simulations available through the RECCAP2 project has provided an opportunity for not only synthesizing but also understanding the changing seasonal cycle in sea surface pCO_2. The use of new observation-based pCO_2/TA products that include DIC and TA in addition to pCO_2 has made it possible to address the following scientific questions: (i) what are the underlying causes of discrepancies in pCO_2 seasonal variability between GOBMs and observation-based products? (ii) what are

the drivers of decadal-timescales trends towards increasing pCO_2 seasonality?, and (iii) are there asymmetries in the growth of pCO_2 and CO_2 flux seasonal variations over multi-decadal timescales that could give rise to a feedback mechanism consistent with the mechanism identified in the modeling study of Fassbender et al. (2022)?

One of the main findings of this study is that there are systematic discrepancies in the climatological seasonal amplitude of surface DIC variations between GOBMs and observation-based pCO_2/TA products over very large spatial scales (**Fig. 5c**) that are primarily responsible for compromising the climatological seasonal cycle of pCO_2. More specifically, simulated DIC seasonal variability is systematically smaller for GOBMs than for DIC seasonal variability in the pCO_2/TA products. The climatological seasonal amplitude of DIC variations can be impacted by both the seasonal amplitude of net biological removal of DIC from the surface layer and the seasonal process of entrainment associated with destratification. Although it is beyond the scope of this study to parse these processes, important information can be inferred from previous studies. Models have previously been shown to prematurely exhaust limiting nutrients in summer (Goris et al., 2018), and such behavior could impact the seasonal amplitude of surface DIC variations

From the biome-averaged time series shown in **Fig. 4**, we have seen that there are some important discrepancies in phasing of the climatological seasonal cycle for pCO_2 between GOBMs and pCO_2 products over biome scales. We have opted here to focus largely on a definition of seasonal cycle amplitude as the difference between winter and summer, defined as JFM-JAS (JAS-JFM) for the Northern (Southern) Hemisphere, as this was deemed to capture the main characteristics of pCO_2 seasonality over large scales, based on the pCO_2 products, as shown in the Hovmöller diagrams in **Fig. 2**. Although our main story of seasonality changes in pCO_2 is not strongly sensitive to this definition for the pCO_2 products or the GOBMs (**Fig. 3**), the presence of phasing differences between pCO_2 products and GOBMs in high latitudes influences the seasonal amplitude calculated according to this definition. We recommend further investigation of such phasing differences to better understand the underlying reasons for this discrepancy.

We emphasized earlier that for our purposes of a synthesis, the GOBMs potentially offer an important advantage over coupled ESMs for our seasonality study and associated attribution analysis. This is due to the fact that the SSTs of the GOBMs are constrained to correspond closely to observations through the imposition of a negative feedback in surface heat fluxes by virtue of using observed surface air temperatures (Large and Yeager, 2009). However, there is no analogous data-constraint applied for the DIC seasonal evolution, other than an indirect and much weaker effective restoring of sea surface pCO_2 to atmospheric pCO_2 over a one-year timescale (an order of magnitude less than for SST). As the SSTs of the GOBMs effectively track the observed seasonal cycle with fidelity, our attention in this study was drawn to the dominant role of DIC seasonality discrepancies in distorting pCO_2 seasonality for the GOBMs relative to the observation-based products.

Nevertheless, as a complementary exercise to the evaluation of GOBMs in **Fig. 4**, we consider here an analogous analysis of a collection of the 11 CMIP6 ESMs listed in **Table 6**. The ESMs are evaluated for their climatological seasonal cycle in pCO_2, SST, and DIC, as well as for decadal changes in pCO_2. For this case, we have considered changes between 1985-1989 and 2010-2014 (an interval four years shorter than in **Fig. 4**) to be consistent with the fact that the historical period in CMIP6 ends in 2014. In general terms there is no fundamental difference between both classes of models. Despite the absence of observational constraints, the simulated SST seasonal cycle in ESMs is in good agreement with observations (dotted lines in central column of **Fig. 13**), although the model spread is significantly larger as expected. The DIC seasonality of the ESMs is very similar to that of the GOBMs (weaker in models than in observation-based pCO_2 products) and the overall pCO_2 changes are very consistent between fully-coupled ESMs and GOBMs (right column of **Fig. 4** and **Fig. 13**). This serves to further underscore our main finding that there is a pervasive discrepancy between ocean carbon cycle models and pCO_2 products, not limited to the RECCAP2 GOBMs, with a seasonal variability in models that is too weak relative to pCO_2 products. Interpretation of projected future seasonal changes in ESMs should therefore take into account the systematic model uncertainties highlighted in this study. As we have seen in **Fig. 12**, a future extension of this analysis for coupled models could benefit from the

1087 inclusion of LEs, which offer a means to deconvolve for models the effects of structural
1088 uncertainty from natural variability uncertainty.

1089

1090 Our attribution analysis indicates that in the subtropics the GOBMs and pCO_2 products are
1091 qualitatively consistent in both the degree of seasonal asymmetry in decadal pCO_2 changes
1092 and CO_2 flux changes (**Fig. 9**), as well as for the mechanistic drivers (**Fig. 10**). This reflects
1093 the fact that both the GOBMs and pCO_2 products are dominated by the thermal pCO_2
1094 component in the subtropics, albeit with the degree of dominance of the thermal pCO_2
1095 component being exaggerated by the GOBMs. The fact that the Northern Hemisphere
1096 subtropics have a larger response than the Southern Hemisphere subtropics is expected given
1097 that the seasonal cycle in SST is larger in the north than in the south, and thereby the thermal
1098 component of seasonality to be larger in the north than in the south. Thus, C_{ant} invasion will
1099 preferentially boost the amplitude of pCO_2 seasonality in the subtropics of the Northern
1100 Hemisphere relative to the Southern Hemisphere, due to the higher amplitude SST variability
1101 to the north.

1102

1103 An important implication of our attribution analysis is that the decadal changes in seasonal
1104 pCO_2 and CO_2 flux amplitudes are qualitatively consistent with the existence of a negative
1105 climate feedback over the historical period spanning 1985-2018. Consistent with what was
1106 found by Fassbender et al. (2022) using future projections with an LE simulation, the seasonal
1107 asymmetry in CO_2 fluxes identified here for the historical period is by inference in large part
1108 due to seasonal asymmetries in wind speeds and thereby piston velocities, rather than in pCO_2
1109 itself. It is our hope that the analysis provided here will motivate future work to quantify the
1110 strength of this feedback over the historical period, as doing so was beyond the scope of this
1111 study.

1112

1113 Two studies that evaluated the early generation of prognostic ocean biogeochemistry models
1114 for their representation of pCO_2 seasonality against observations were McKinley et al. (2006)
1115 for the case of the North Pacific and Tjiputra et al. (2012) for the case of the North Atlantic.
1116 Although an explicit comparison of the models applied by McKinley et al. (2006) and

Tjiputra et al. (2012) with the RECCAP2 GOBMs is beyond the scope of this study, it is important to ask, "how far have we come?". The message from this study is that the new suite of pCO_2/TA products that provide time-varying surface DIC products that have become available provide invaluable tools for identifying and attributing potential model biases over global scales. Moving forward, we recommend that efforts be devoted to understanding how complexity in physical and biogeochemical process representation in models is reflected in pCO_2 seasonality. For the case of the biogeochemical components of models, one opportunity would be to evaluate with the same circulation state a climatology of pCO_2 seasonality using different complexity of biogeochemical models, analogous to what was explored by Galbraith et al. (2015) with the BLING and TOPAZ biogeochemical models, or by Karakus et al. (2022). Moreover, it could be beneficial to link the simulated strength of key circulation metrics (e.g. Atlantic Meridional Overturning Circulation for the North Atlantic) to the pCO_2 seasonality of the GOBMs. In a study with several coupled climate models, Goris et al. (2022) were able to show that the representation of a model's pCO_2 seasonality in the North Atlantic is strongly linked to the simulated strength of the Gulf Stream volume transport. In order to address the question of how missing physical processes may impact biogeochemistry and pCO_2 seasonality, it would be beneficial to explore independently the impact of mesoscale turbulence with ocean eddies (Lévy et al., 1998) and shear-induced turbulence associated with near-inertial oscillations, ocean swells, and wind stirring (Jochum et al., 2013; Keerthi et al., 2021; Rodgers et al., 2014) through perturbation studies with individual models. Such efforts would be beneficial in identifying the processes that contribute to the discrepancies identified in this RECCAP2 synthesis effort.

5 Conclusions

In this study, we have presented as a contribution to the RECCAP2 effort a synthesis of how the seasonal cycle in sea surface pCO_2 and air-sea CO_2 fluxes has changed over the last three decades (1985-2018). Our main findings include:

For a 2014-2018 climatology, we identified a systematic discrepancy in the seasonal amplitude of surface DIC variations between the GOBMs, which are too weak, and the surface DIC products, such that the pCO_2 seasonal cycle in subtropical biomes is spuriously large, and both the amplitude and phase of seasonal pCO_2 variations are spuriously modulated in subpolar and Southern Ocean biomes. Similar biases are found in ESMs as submitted to CMIP6. When averaged over aggregated biomes, both pCO_2 products and GOBMs represent consistent increases in the seasonal amplitude of pCO_2 and CO_2 fluxes between 1985-1989 and 2014-2018.

Decadal increases in pCO_2 seasonal amplitude in subtropical biomes are shown to be dominated process-wise by the invasion flux of anthropogenic carbon (C_{ant}) for both the pCO_2 products and GOBMs. For pCO_2 seasonality changes over subpolar and circumpolar biomes, GOBMs see this change as being dominated by C_{ant} invasion, but for pCO_2 products it is dominated rather by modulations of the climate state, which can be associated with changes in SST seasonality or in perturbations occurring in mixing or biological processes. Our analysis of LE simulations indicates that the climate-driven signal found in the subpolar biomes of the Northern Hemisphere (bold blue line in **Fig. 10a**) is likely too large to be explained by natural variability, as estimated from the amplitude of natural variability in the LE (width of blue shading in **Fig. 10g**). Considered together, the subtropical biomes exhibit decadal increases in CO_2 flux seasonality that are larger during winter than summer, consistent with the mechanism identified by Fassbender et al. (2022) whereby increased seasonal cycles may be promoting a negative feedback in the climate system.

We have also identified and quantified two distinct sources of uncertainty that can impact the detection of anthropogenic trends in pCO_2 seasonal amplitude. The first type is mapping uncertainty (**Fig. 3a** and **Fig. 3c**), which is in essence a reducible form of uncertainty. The second type is natural variability uncertainty (**Fig. 11** and **Fig. 12**), which we identified with the LE simulations, with this being an irreducible form of uncertainty. For both cases, we identified that there are large regions of the global domain where the forced anthropogenic signal does not rise above the one standard deviation (noise) level at the gridpoint scale. Even for the idealized case of a perfectly-resolving observational system where mapping error

1177 disappears, one would still need to quantify the degree of confidence one has that a local
1178 measured decadal change represents forced changes in the presence of natural variability. We
1179 tend in the subtropics to find unanimous agreement at the gridpoint scale across pCO_2
1180 products and GOBMs on the dominant mechanism of enhanced pCO_2 seasonality, namely the
1181 C_{ant}-driven boost to the thermally component of pCO_2 seasonality.

1182

1183 Thus our synthesis provides evidence that the seasonal pCO_2 amplitude has significantly
1184 increased globally, and for many regions, this increase has already emerged from the noise
1185 with biome aggregation. This highlights the importance of including seasonal changes when
1186 considering long-term acidification trends, as we will likely cross critical thresholds in some
1187 seasons, before such thresholds are crossed in the annual mean (Burger et al., 2020; Henson et
1188 al., 2017; Kwiatkowski and Orr, 2018; McNeil and Sasse, 2016). For similar reasons, we
1189 recommend that modeling resources be devoted to identifying missing processes and
1190 implementing representations or parameterizations of the pertinent missing processes in ocean
1191 biogeochemical models.

1192

1193 Our conclusions rest on the growing availability of pCO_2 products that include associated
1194 time-varying DIC and TA products, with this representing a significant advance for scientific
1195 inquiry into the mechanisms controlling the ocean uptake of anthropogenic carbon. The fact
1196 that the three pCO_2/TA products (considered here as surface DIC products) that exist to date
1197 (JMAMLR, OceanSODA-ETHZ, and CMEMS-LSCE-FFNN) indicate consistent patterns of
1198 seasonal variability over large scales, which are also consistent with depth-resolving three-
1199 dimensional monthly DIC climatologies (MOBO-DIC and NNGv2LDEO) over large scales,
1200 should boost community confidence in the scientific utility of these products. We therefore
1201 strongly recommend to the pCO_2 product providers to provide DIC and TA along with sea
1202 surface pCO_2 and air-sea CO_2 fluxes. In parallel, we recommend a rigorous skill-assessment
1203 of the mapping methods that transform from SOCAT measurements to globally-gridded pCO_2
1204 products, for example by using LEs with ESMs as a synthetic testbed similar to the work
1205 presented by Gloege et al. (2021).

1206

1207

1208

1209

1210

1211

1212

ACKNOWLEDGEMENTS

The authors have no conflicts of interest. KR and JS thank the Bjerknes Centre for Climate Research and the IBS Centre for Climate Physics for travel funding. KBR, KS, JEK, and SSh were supported by the Institute for Basic Science (grant no. IBS-R028-D1). The simulations with the CESM2-LE were conducted on the IBS/ICCP supercomputer "Aleph", a 1.43 petaflop high-performance Cray XC50-LC Skylake computing system. AJF was supported by NOAA's Pacific Marine Environmental Laboratory (PMEL). This is PMEL contribution 5502. JS acknowledges support by the Research Council of Norway (grant no. 270061) and JS and NGo are thankful for provision of computational/storage resources by UNINET/sigma2/(nn/ns2980k). JH was supported by the Initiative and Networking Fund of the Helmholtz Association (Helmholtz Young Investigator Group Marine Carbon and Ecosystem Feedbacks in the Earth System [MarESys], grant number VH-NG-1301). PL received funding from the European Union's Horizon 2020 research and innovation program under grant agreement no. 821003 (project 4C). LK was supported by NSF's Southern Ocean Carbon and Climate Observations and Modeling (SOCCOM) Project under the NSF Awards PLR-1425989 and OPP-1936222, with additional support from NOAA and NASA. PV, JT, and NGo acknowledge funding from the Research Council of Norway (COLUMBIA-275268, and CE2COAST-318477). MI, KT, and YI were supported by the Environment Research and Technology Development Fund (JPMEERF21S20810) of the Environmental Restoration and Conservation Agency provided by Ministry of the Environment of Japan. MI and KT were also supported by MEXT KAKENHI Grant Number JP19H05700. JDM, NGr, and LGr acknowledge support from the European Union's Horizon 2020 research and innovation programme under grant agreement no. 821003 (project 4C) and no. 820989 (project COMFORT). MG and TTTC acknowledge funding from the European Copernicus Marine Environment Monitoring Service (no. 83-CMEMSTAC-MOB). This publication is partially funded by the Cooperative Institute for Climate, Ocean, and Ecosystem Studies (COCOES) under NOAA Cooperative Agreement NA20OAR4320271, Contribution No. 2023-1266.

OPEN RESEARCH

All of the RECCAP2 data will be made available in a public repository before publication.

CONTRIBUTOR ROLES TAXONOMY

Conceptualization (Ideas; formulation or evaluation of overarching goals/aims):

KBR, JS, AJF, RY

Data Curation (Management activities to annotate (produce metadata)):

LGr, YI, TTTC, JDM, LK, PV, JS, PL, AV, JH, NGo, JT

Formal analysis (application of statistical, mathematical, computational, or other formal techniques to analyze or synthesize study data):

JS, AJF, RY, HF, KS, SSc, KBR

Funding acquisition (acquisition of the financial support for the project leading to publication):

KR

Investigation (Conducting a research and investigation process, specifically performing the experiments, or data/evidence collection):

JS, AJF, RY, JDM, NGo, JEK, HF, KS, PL, SSc, SSh, MI, KT, KBR

Project administration (Management and coordination responsibility for the research activity planning and execution):

NGr, JH, MI, JDM, KBR, JS, AJF, PL

Resources (Provision of study materials, reagents, materials, patents, etc.):

N/A

Software (Programming, software development, designing computer programs, implementation of the computer code and supporting algorithms, testing of existing code components):

JS, AJF, RY, HF, JDM, NGo, JEK, SSc, SSh, KS, PL, KBR

Supervision (Oversight and leadership responsibility for the research activity planning and execution, including mentorship external to the core team):

KBR, JS, AJF

Validation (Verification, whether as a part of the activity or separate, of the overall replication/reproducibility of results/experiments and other research outputs):

N/A

Visualization (Preparation, creation and/or presentation of the published work, specifically visualization/data presentation):

JS, AJF, RY, HF, JDM, NGo, JEK, SSh, KS, PL, KBR

Writing – original draft (Preparation, creation, and/or presentation of the published work, specifically writing the initial draft (including substantive translation):

KBR

Writing – review and editing (Preparation, creation, and/or presentation of the published work by those form the original research group, specifically critical review, commentary, or revision – including pre- or post-publication stages):

Everyone

Names	Aggregated seasonality biomes	RECCAP2 biomes
North Atlantic subpolar seasonally stratified	NA-SPSS	NA-SPSS
North Pacific subpolar seasonally stratified	NP-SPSS	NP-SPSS
Northern Hemisphere subtropical seasonally stratified	NH-STSS	NA-STSS+NP-STSS
Northern Hemisphere subtropical permanently stratified	NH-STPS	NA-STPS + NP-STPS
Southern Hemisphere subtropical permanently stratified	SH-STPS	SA-STPS + SP-STPS + Southern Indian Ocean
Southern Hemisphere seasonally stratified (subpolar and subtropical combined)	SH-SS	SO-STSS + SO-SPSS

Table 1: The six aggregated biomes used in this study. The full names are given in the left column, the abbreviated names used throughout this study in the central column, and the original RECCAP2 biomes from which they are constructed are listed in the right column. Our six aggregated biomes are shown in the central panel of **Fig. 1**. As has been noted in the Methods section, spatial and temporal data coverage of data products and models might further constrain the area of the aggregated biomes used for our analysis.

Product name	References	Duration and Remarks
CSIRML6	Gregor et al., 2019	1985-2018
CMEMS-LSCE-FFNN	Chau et al., 2022	1985-2018; DIC and TA available
JMAMLR	Iida et al., 2021	1985-2019; DIC and TA available
Jena-MLS	Rödenbeck et al., 2013, 2022	1985-2018
NIES-ML3	Zeng et al., 2022	1980-2020
OceanSODA-ETHZ	Gregor and Gruber, 2021	1985-2018; DIC and TA available
SOMFFN	Landschützer et al., 2016	1982-2019
UOEX_WAT20	Watson et al., 2020	1985-2019
spco2_LDEO_HPD	Gloege et al., 2022	1985-2018

Table 2: pCO_2 data products used for this study. The products are described more completely in the global RECCAP2 analysis of DeVries submitted to Global Biogeochemical Cycles. Note that the CMEMS-LSCE-FFNN, JMAMLR, and OceanSODA-ETHZ products include associated surface DIC and TA fields that are used in this study.

1307

Model Name	References	Remarks
CCSM	Doney et al., 2009	Covers only 1985-2017, For 2014-2018 climatologies an exception is made for this model
CESM-ETHZ	Doney et al., 2009; Lindsay et al., 2014; Yang and Gruber, 2016	
CNRM-ESM2-1	Berthet et al., 2019; Séférian et al., 2016, 2019	
EC-Earth3	Döscher et al., 2022	
FESOM-REcoM-LR	Hauck et al., 2020	No phosphate available, WOA2018 used for attribution analysis
MOM6-COBALT-PRINCETON	Liao et al., 2020; Stock et al., 2020	
MRI-ESM2-1	Nakano et al., 2011; Urakawa et al., 2020	
NorESM-OC1.2	Schwinger et al., 2016	
ORCA025-GEOMAR	Chien et al., 2022; Kriest and Oschlies, 2015; Madec et al., 2017	No silicate available, silicate from WOA2018 used for attribution analysis
IPSL-NEMO-PISCES	Aumont et al., 2015; Friedlingstein et al., 2022	

PlankTOM12	(Le Quéré et al., 2010; Wright et al., 2021)	No silicate available, WOA2018 used for attribution analysis
Assimilation Model	**References**	**Remarks**
OCIM v2021	(DeVries, 2014, 2022)	Abiotic model with data assimilated circulation; Used for some analyses but never included in ensemble means for GOBMs

Table 3: Global Ocean Biogeochemical Models (GOBMs) and an assimilation model used for this study. Model names are given in the first column, references are given in the second column, and comments pertinent to the application of the products are given in the third column. The CCSM model differs from the others in that output only extends to 2017 rather than to the RECCAP2 protocol end-year of 2018.

Earth System Model	References	Comments
CESM2 (CMIP6)	Rodgers et al., 2021	50 members
CanESM2 (CMIP5)	Kirchmeier-Young et al., 2017	50 members
CanESM5 (CMIP6)	Swart et al., 2019b	24 members
CESM1 (CMIP5)	Kay et al., 2015	34 members
ESM2M (CMIP5)	Rodgers et al., 2015	30 members
MPI-GE (CMIP5)	Maher et al., 2019	100 members

Table 4: Large Ensemble Simulations used in the analysis in **Fig. 12**.

	GOBMs		pCO_2 products	
Region	pCO_2 amplitude	pCO_2 amplitude change	pCO_2 amplitude	pCO_2 amplitude change
NA-SPSS	-18.5 +/- 18.5	-2.1 +/- 9.9	46.0 +/- 4.9	5.9 +/- 6.1
NP-SPSS	-34.1 +/- 29.3	-8.3 +/- 6.0	17.1 +/- 4.3	2.8 +/- 7.7
NH-STSS	-67.8 +/- 16.2	-10.7 +/- 3.2	-37.2 +/- 1.7	-9.8 +/- 3.9
NH-STPS	-42.0 +/- 6.7	-6.3 +/- 1.1	-33.2 +/- 2.4	-6.3 +/- 2.8
SH-STPS	-39.5 +/- 10.7	-2.7 +/- 2.0	-29.4 +/- 3.2	-5.3 +/- 2.7
SH-SS	-5.8 +/- 14.7	0.6 +/- 1.4	11.4 +/- 2.4	1.0 +/- 2.5

Table 5: Seasonal amplitude (winter-minus-summer) of biome averaged pCO_2 for GOBMs and pCO_2 products for the period 2014-2018. Seasons are defined as the three month periods JFM and JAS. Change represents the difference between 1985-1989 and 2014-2018,

Model Name	ESM reference	Data reference
ACCESS-ESM1-5	Law et al., 2017	Ziehn et al., 2019
CanESM5	Swart et al., 2019b	Swart et al., 2019a
CESM2	Lauritzen et al., 2018	Danabasoglu, 2019
CMCC-ESM2	Lovato et al., 2022	Lovato et al., 2021
CNRM-ESM2-1	Séférian et al., 2019	Séférian, 2018
GFDL-ESM4	Dunne et al., 2020	Krasting et al., 2018
IPSL-CM6A-LR	Boucher et al., 2020	Boucher et al., 2018
MIROC-ES2L	Hajima et al., 2020	Hajima et al., 2019
MRI-ESM2-0	Yukimoto et al., 2019b	Yukimoto et al., 2019a
NorESM2-MM	Seland et al., 2020	Bentsen et al., 2019
UKESM-0-LL	Sellar et al., 2019	Tang et al., 2019

Table 6: CMIP6 models evaluated against pCO_2 products in **Fig. 13**.

REFERENCES

Anav, A., Friedlingstein, P., Kidston, M., Bopp, L., Ciais, P., Cox, P., et al. (2013). Evaluating the Land and Ocean Components of the Global Carbon Cycle in the CMIP5 Earth System Models. *Journal of Climate*, *26*(18), 6801–6843. https://doi.org/10.1175/jcli-d-12-00417.1

Aumont, O., Ethe, C., Tagliabue, A., Bopp, L., & Gehlen, M. (2015). PISCES-v2: an ocean biogeochemical model for carbon and ecosystem studies. *Geoscientific Model Development*, *8*(8), 2465–2513. https://doi.org/10.5194/gmd-8-2465-2015

Bakker, D. C. E., Pfeil, B., Landa, C. S., Metzl, N., O'Brien, K. M., Olsen, A., et al. (2016). A multi-decade record of high-quality fCO_2 data in version 3 of the Surface Ocean CO_2 Atlas (SOCAT). *Earth System Science Data*, *8*(2), 383–413. https://doi.org/10.5194/essd-8-383-2016

Bentsen, M., Oliviè, D. J. L., Seland, Ø., Toniazzo, T., Gjermundsen, A., Graff, L. S., et al. (2019). NCC NorESM2-MM model output prepared for CMIP6 CMIP historical. *Earth System Grid Federation*, *635*.

Berthet, S., Seferian, R., Bricaud, C., Chevallier, M., Voldoire, A., & Ethe, C. (2019). Evaluation of an Online Grid-Coarsening Algorithm in a Global Eddy-Admitting Ocean Biogeochemical Model. *Journal of Advances in Modeling Earth Systems*, *11*(6), 1759–1783. https://doi.org/10.1029/2019ms001644

Boucher, O., Denvil, S., Levavasseur, G., Cozic, A., Caubel, A., & Foujols, M. A. (2018). IPSL IPSL-CM6A-LR model output prepared for CMIP6 CMIP historical. Version 20180803. Earth System Grid Federation.

1358 Boucher, O., Servonnat, J., Albright, A. L., Aumont, O., Balkanski, Y., Bastrikov, V., et al.
1359 (2020). Presentation and Evaluation of the IPSL-CM6A-LR Climate Model. *Journal*
1360 *of Advances in Modeling Earth Systems*, *12*(7). https://doi.org/10.1029/2019ms002010

1361 Broullón, D., Pérez, F. F., Velo, A., Hoppema, M., Olsen, A., Takahashi, T., et al. (2020). A
1362 global monthly climatology of oceanic total dissolved inorganic carbon: a neural
1363 network approach. *Earth System Science Data*, *12*(3), 1725–1743.

1364 Burger, F. A., John, J. G., & Frölicher, T. L. (2020). Increase in ocean acidity variability and
1365 extremes under increasing atmospheric CO_2. *Biogeosciences*, *17*(18), 4633–4662.
1366 https://doi.org/10.5194/bg-17-4633-2020

1367 Cabré, A., Shields, D., Marinov, I., & Kostadinov, T. S. (2016). Phenology of size-partitioned
1368 phytoplankton carbon-biomass from ocean color remote sensing and CMIP5 models.
1369 *Frontiers in Marine Science*, *3*, 39.

1370 Chau, T. T. T., Gehlen, M., & Chevallier, F. (2022). A seamless ensemble-based
1371 reconstruction of surface ocean pCO_2 and air–sea CO_2 fluxes over the global coastal
1372 and open oceans. *Biogeosciences*, *19*(4), 1087–1109.

1373 Chien, C.-T., Durgadoo, J. V., Ehlert, D., Frenger, I., Keller, D. P., Koeve, W., et al. (2022).
1374 FOCI-MOPS v1–integration of marine biogeochemistry within the Flexible Ocean and
1375 Climate Infrastructure version 1 (FOCI1) Earth system model. *Geoscientific Model*
1376 *Development*, *15*(15), 5987–6024.

1377 Danabasoglu, G. (2019). NCAR CESM2-WACCM model output prepared for CMIP6 CMIP
1378 historical, Earth System Grid Federation [data set].

Danabasoglu, G., Lamarque, J. -F., Bacmeister, J., Bailey, D. A., DuVivier, A. K., Edwards, J., et al. (2020). The Community Earth System Model Version 2 (CESM2). *Journal of Advances in Modeling Earth Systems*, *12*(2). https://doi.org/10.1029/2019MS001916

DeVries, T. (2014). The oceanic anthropogenic CO_2 sink: Storage, air-sea fluxes, and transports over the industrial era. *Global Biogeochemical Cycles*, *28*(7), 631–647.

DeVries, T. (2022). Atmospheric CO_2 and sea surface temperature variability cannot explain recent decadal variability of the ocean CO_2 sink. *Geophysical Research Letters*, *49*(7), e2021GL096018.

Doney, S. C., Lima, I., Feely, R. A., Glover, D. M., Lindsay, K., Mahowald, N., et al. (2009). Mechanisms governing interannual variability in upper-ocean inorganic carbon system and air-sea CO_2 fluxes: Physical climate and atmospheric dust. *Deep-Sea Research Part II-Topical Studies in Oceanography*, *56*(8–10), 640–655. https://doi.org/10.1016/j.dsr2.2008.12.006

Döscher, R., Acosta, M., Alessandri, A., Anthoni, P., Arsouze, T., Bergman, T., et al. (2022). The EC-Earth3 earth system model for the coupled model intercomparison project 6. *Geoscientific Model Development*, *15*(7), 2973–3020.

Dunne, J. P., Horowitz, L. W., Adcroft, A. J., Ginoux, P., Held, I. M., John, J. G., et al. (2020). The GFDL Earth System Model Version 4.1 (GFDL-ESM 4.1): Overall Coupled Model Description and Simulation Characteristics. *Journal of Advances in Modeling Earth Systems*, *12*(11), 56. https://doi.org/10.1029/2019ms002015

Fassbender, A. J., Rodgers, K. B., Palevsky, H. I., & Sabine, C. L. (2018). Seasonal Asymmetry in the Evolution of Surface Ocean pCO_2 and pH Thermodynamic Drivers

and the Influence on Sea-Air CO_2 Flux. *Global Biogeochemical Cycles*, *32*(10), 1476–1497. https://doi.org/10.1029/2017gb005855

Fassbender, A. J., Schlunegger, S., Rodgers, K. B., & Dunne, J. P. (2022). Quantifying the role of seasonality in the marine carbon cycle feedback: an ESM2M case study. *Global Biogeochemical Cycles*, *36*(6), e2021GB007018.

Fay, A. R., & McKinley, G. A. (2014). Global open-ocean biomes: mean and temporal variability. *Earth System Science Data*, *6*(2), 273–284. https://doi.org/10.5194/essd-6-273-2014

Friedlingstein, P., Jones, M. W., O'Sullivan, M., Andrew, R. M., Bakker, D. C. E., Hauck, J., et al. (2022). Global carbon budget 2021. *Earth System Science Data*, *14*(4), 1917–2005.

Friedlingstein, P., O'Sullivan, M., Jones, M. W., Andrew, R. M., Gregor, L., Hauck, J., et al. (2022). Global carbon budget 2022. *Earth System Science Data*, *14*(11), 4811–4900.

Galbraith, E. D., Dunne, J. P., Gnanadesikan, A., Slater, R. D., Sarmiento, J. L., Dufour, C. O., et al. (2015). Complex functionality with minimal computation: Promise and pitfalls of reduced-tracer ocean biogeochemistry models. *Journal of Advances in Modeling Earth Systems*, *7*(4), 2012–2028. https://doi.org/10.1002/2015ms000463

Gallego, M. A., Timmermann, A., Friedrich, T., & Zeebe, R. E. (2018). Drivers of future seasonal cycle changes in oceanic pCO_2. *Biogeosciences*, *15*(17), 5315–5327. https://doi.org/10.5194/bg-15-5315-2018

Garcia, H. E., Weathers, K. W., Paver, C. R., Smolyar, I., Boyer, T. P., Locarnini, M. M., et al. (2019). World ocean atlas 2018. Vol. 4: Dissolved inorganic nutrients (phosphate, nitrate and nitrate+ nitrite, silicate).

Gloege, L., McKinley, G. A., Landschützer, P., Fay, A. R., Frölicher, T. L., Fyfe, J. C., et al. (2021). Quantifying Errors in Observationally Based Estimates of Ocean Carbon Sink Variability. *Global Biogeochemical Cycles*, *35*(4), e2020GB006788.

Gloege, L., Yan, M., Zheng, T., & McKinley, G. A. (2022). Improved quantification of ocean carbon uptake by using machine learning to merge global models and pCO_2 data. *Journal of Advances in Modeling Earth Systems*, *14*(2), e2021MS002620.

Gloor, M., Gruber, N., Sarmiento, J., Sabine, C. L., Feely, R. A., & Rodenbeck, C. (2003). A first estimate of present and preindustrial air-sea CO_2 flux patterns based on ocean interior carbon measurements and models. *Geophysical Research Letters*, *30*(1). https://doi.org/10.1029/2002gl015594

Gorgues, T., Aumont, O., & Rodgers, K. B. (2010). A mechanistic account of increasing seasonal variations in the rate of ocean uptake of anthropogenic carbon. *Biogeosciences*, *7*(8), 2581–2589. https://doi.org/10.5194/bg-7-2581-2010

Goris, N., Tjiputra, J. F., Olsen, A., Schwinger, J., Lauvset, S. K., & Jeansson, E. (2018). Constraining Projection-Based Estimates of the Future North Atlantic Carbon Uptake. *Journal of Climate*, *31*(10), 3959–3978. https://doi.org/10.1175/jcli-d-17-0564.1

Goris, N., Johannsen, K., & Tjiputra, J. (2022). Gulf Stream and interior western boundary volume transport as key regions to constrain the future North Atlantic Carbon Uptake. *Geoscientific Model Development Discussions*, 1–30.

Gregor, L., & Gruber, N. (2021). OceanSODA-ETHZ: a global gridded data set of the surface ocean carbonate system for seasonal to decadal studies of ocean acidification. *Earth System Science Data*, *13*(2), 777–808. https://doi.org/10.5194/essd-13-777-2021

Gregor, L., Lebehot, A. D., Kok, S., & Monteiro, P. M. S. (2019). A comparative assessment of the uncertainties of global surface ocean CO_2 estimates using a machine-learning ensemble (CSIR-ML6 version 2019a) - have we hit the wall? *Geoscientific Model Development*, *12*(12), 5113–5136. https://doi.org/10.5194/gmd-12-5113-2019

Gruber, N., Gloor, M., Fletcher, S. E. M., Doney, S. C., Dutkiewicz, S., Follows, M. J., et al. (2009). Oceanic sources, sinks, and transport of atmospheric CO_2. *Global Biogeochemical Cycles*, *23*. https://doi.org/10.1029/2008gb003349

Gruber, N., Clement, D., Carter, B. R., Feely, R. A., van Heuven, S., Hoppema, M., et al. (2019). The oceanic sink for anthropogenic CO_2 from 1994 to 2007. *Science*, *363*(6432), 1193-+. https://doi.org/10.1126/science.aau5153

Hajima, T., Abe, M., Arakawa, O., Suzuki, T., Komuro, Y., Ogura, T., et al. (2019). MIROC MIROC-ES2L model output prepared for CMIP6 CMIP historical. *Earth System Grid Federation. Available Online at Https://Doi. Org/10.22033/ESGF/CMIP6*, *5602*.

Hajima, T., Watanabe, M., Yamamoto, A., Tatebe, H., Noguchi, M. A., Abe, M., et al. (2020). Development of the MIROC-ES2L Earth system model and the evaluation of biogeochemical processes and feedbacks. *Geoscientific Model Development*, *13*(5), 2197–2244. https://doi.org/10.5194/gmd-13-2197-2020

Hauck, J., & Volker, C. (2015). Rising atmospheric CO_2 leads to large impact of biology on Southern Ocean CO_2 uptake via changes of the Revelle factor. *Geophysical Research Letters*, *42*(5), 1459–1464. https://doi.org/10.1002/2015gl063070

1466 Hauck, J., Zeising, M., Le Quere, C., Gruber, N., Bakker, D. C. E., Bopp, L., et al. (2020).
1467 Consistency and Challenges in the Ocean Carbon Sink Estimate for the Global Carbon
1468 Budget. *Frontiers in Marine Science*, *7*, 22.
1469 https://doi.org/10.3389/fmars.2020.571720

1470 Henson, S. A., Beaulieu, C., Ilyina, T., John, J. G., Long, M., Séférian, R., et al. (2017). Rapid
1471 emergence of climate change in environmental drivers of marine ecosystems. *Nature*
1472 *Communications*, *8*, 9. https://doi.org/10.1038/ncomms14682

1473 Holte, J., & Talley, L. (2009). A New Algorithm for Finding Mixed Layer Depths with
1474 Applications to Argo Data and Subantarctic Mode Water Formation. *Journal of*
1475 *Atmospheric and Oceanic Technology*, *26*(9), 1920–1939.
1476 https://doi.org/10.1175/2009jtecho543.1

1477 Iida, Y., Takatani, Y., Kojima, A., & Ishii, M. (2021). Global trends of ocean CO_2 sink and
1478 ocean acidification: an observation-based reconstruction of surface ocean inorganic
1479 carbon variables. *Journal of Oceanography*, *77*(2), 323–358.
1480 https://doi.org/10.1007/s10872-020-00571-5

1481 Jochum, M., Briegleb, B. P., Danabasoglu, G., Large, W. G., Norton, N. J., Jayne, S. R., et al.
1482 (2013). The Impact of Oceanic Near-Inertial Waves on Climate. *Journal of Climate*,
1483 *26*(9), 2833–2844. https://doi.org/10.1175/jcli-d-12-00181.1

1484 Karakuş, O., Völker, C., Iversen, M., Hagen, W., & Hauck, J. (2022). The role of zooplankton
1485 grazing and nutrient recycling for global ocean biogeochemistry and phytoplankton
1486 phenology. *J. Geophys. Res. Biogeosciences*, *127*(10), e2022JG006798.

1487 Kay, J. E., Deser, C., Phillips, A., Mai, A., Hannay, C., Strand, G., et al. (2015). The
1488 Community Earth System Model (CESM) Large Ensemble Project: A Community

Resource for Studying Climate Change in the Presence of Internal Climate Variability. *Bulletin of the American Meteorological Society*, *96*(8), 1333–1349. https://doi.org/10.1175/BAMS-D-13-00255.1

Keerthi, M. G., Lévy, M., & Aumont, O. (2021). Intermittency in phytoplankton bloom triggered by modulations in vertical stability. *Scientific Reports*, *11*(1), 1285.

Keppler, L., Landschützer, P., Gruber, N., Lauvset, S., & Stemmler, I. (2020a). Mapped Observation-Based Oceanic Dissolved Inorganic Carbon (DIC), monthly climatology from January to December (based on observations between 2004 and 2017), from the Max-Planck-Institute for Meteorology (MOBO-DIC_MPIM)(NCEI Accession 0221526), NOAA National Centers for Environmental Information [data set]. *Centers Environ. Information. Dataset., Https://Doi. Org/10.25921/Yvzj-Zx46*, *1020*.

Keppler, L., Landschützer, P., Gruber, N., Lauvset, S. K., & Stemmler, I. (2020b). Seasonal Carbon Dynamics in the Near-Global Ocean. *Global Biogeochemical Cycles*, *34*(12). https://doi.org/10.1029/2020gb006571

Kessler, A., & Tjiputra, J. (2016). The Southern Ocean as a constraint to reduce uncertainty in future ocean carbon sinks. *Earth System Dynamics*, *7*(2), 295–312. https://doi.org/10.5194/esd-7-295-2016

Kirchmeier-Young, M. C., Zwiers, F. W., & Gillett, N. P. (2017). Attribution of Extreme Events in Arctic Sea Ice Extent. *Journal of Climate*, *30*(2), 553–571. https://doi.org/10.1175/jcli-d-16-0412.1

Krasting, J. P., Stouffer, R. J., Griffies, S. M., Hallberg, R. W., Malyshev, S. L., Samuels, B. L., & Sentman, L. T. (2018). Role of Ocean Model Formulation in Climate Response Uncertainty. *Journal of Climate*. https://doi.org/10.1175/jcli-d-18-0035.1

Kriest, I., & Oschlies, A. (2015). MOPS-1.0: towards a model for the regulation of the global oceanic nitrogen budget by marine biogeochemical processes. *Geoscientific Model Development*, *8*(9), 2929–2957.

Kwiatkowski, L., & Orr, J. C. (2018). Diverging seasonal extremes for ocean acidification during the twenty-first century. *Nature Climate Change*, *8*(2), 141-+. https://doi.org/10.1038/s41558-017-0054-0

Landschützer, P., Gruber, N., Bakker, D. C. E., & Schuster, U. (2014). An observation-based global monthly gridded sea surface pCO_2 product from 1998 through 2011 and its monthly climatology. *Carbon Dioxide Information Analysis Center, ORNL, US Department of Energy (Ed.), Oak Ridge, Tennessee*.

Landschützer, P., Gruber, N., & Bakker, D. C. E. (2016). Decadal variations and trends of the global ocean carbon sink. *Global Biogeochemical Cycles*, *30*(10), 1396–1417. https://doi.org/10.1002/2015gb005359

Landschützer, P., Gruber, N., Bakker, D. C. E., Stemmler, I., & Six, K. D. (2018). Strengthening seasonal marine CO_2 variations due to increasing atmospheric CO_2. *Nature Climate Change*, *8*(2), 146-+. https://doi.org/10.1038/s41558-017-0057-x

Large, W. G., & Yeager, S. G. (2009). The global climatology of an interannually varying air-sea flux data set. *Climate Dynamics*, *33*(2–3), 341–364. https://doi.org/10.1007/s00382-008-0441-3

Lauritzen, P. H., Nair, R. D., Herrington, A. R., Callaghan, P., Goldhaber, S., Dennis, J. M., et al. (2018). NCAR release of CAM-SE in CESM2. 0: A reformulation of the spectral element dynamical core in dry-mass vertical coordinates with comprehensive

1534 treatment of condensates and energy. *Journal of Advances in Modeling Earth Systems*,
1535 *10*(7), 1537–1570.

1536 Law, R. M., Ziehn, T., Matear, R. J., Lenton, A., Chamberlain, M. A., Stevens, L. E., et al.
1537 (2017). The carbon cycle in the Australian Community Climate and Earth System
1538 Simulator (ACCESS-ESM1) - Part 1: Model description and pre-industrial simulation.
1539 *Geoscientific Model Development*, *10*(7), 2567–2590. https://doi.org/10.5194/gmd-10-
1540 2567-2017

1541 Le Quéré, C., Takahashi, T., Buitenhuis, E. T., Rodenbeck, C., & Sutherland, S. C. (2010).
1542 Impact of climate change and variability on the global oceanic sink of CO_2. *Global*
1543 *Biogeochemical Cycles*, *24*. https://doi.org/10.1029/2009gb003599

1544 Lévy, M., Memery, L., & Madec, G. (1998). The onset of a bloom after deep winter
1545 convection in the northwestern Mediterranean sea: mesoscale process study with a
1546 primitive equation model. *Journal of Marine Systems*. https://doi.org/10.1016/s0924-
1547 7963(97)00097-3

1548 Liao, E. H., Resplandy, L., Liu, J. J., & Bowman, K. W. (2020). Amplification of the Ocean
1549 Carbon Sink During El Niños: Role of Poleward Ekman Transport and Influence on
1550 Atmospheric CO_2. *Global Biogeochemical Cycles*, *34*(9).
1551 https://doi.org/10.1029/2020gb006574

1552 Lindsay, K., Bonan, G. B., Doney, S. C., Hoffman, F. M., Lawrence, D. M., Long, M. C., et
1553 al. (2014). Preindustrial-Control and Twentieth-Century Carbon Cycle Experiments
1554 with the Earth System Model CESM1(BGC). *Journal of Climate*, *27*(24), 8981–9005.
1555 https://doi.org/10.1175/jcli-d-12-00565.1

1556 Lovato, T., Peano, D., & Butenschön, M. (2021). CMCC CMCC-ESM2 model output
1557 prepared for CMIP6 CMIP historical. *Earth Syst. Grid Fed.*

1558 Lovato, T., Peano, D., Butenschön, M., Materia, S., Iovino, D., Scoccimarro, E., et al. (2022).
1559 CMIP6 simulations with the CMCC Earth system model (CMCC-ESM2). *Journal of*
1560 *Advances in Modeling Earth Systems*, *14*(3), e2021MS002814.

1561 Madec, G., Bourdall□-Badie, R., Bouttier, P.-A., Bricaud, C., Bruciaferri, D., Calvert, D., et
1562 al. (2017). NEMO ocean engine.

1563 Maher, N., Milinski, S., Suarez-Gutierrez, L., Botzet, M., Dobrynin, M., Kornblueh, L., et al.
1564 (2019). The Max Planck Institute Grand Ensemble: Enabling the Exploration of
1565 Climate System Variability. *Journal of Advances in Modeling Earth Systems*, *11*(7),
1566 2050–2069. https://doi.org/10.1029/2019ms001639

1567 McKinley, G. A., Takahashi, T., Buitenhuis, E., Chai, F., Christian, J. R., Doney, S. C., et al.
1568 (2006). North Pacific carbon cycle response to climate variability on seasonal to
1569 decadal timescales. *Journal of Geophysical Research-Oceans*, *111*(C7).
1570 https://doi.org/10.1029/2005jc003173

1571 McNeil, B. I., & Sasse, T. P. (2016). Future ocean hypercapnia driven by anthropogenic
1572 amplification of the natural CO_2 cycle. *Nature*, *529*(7586), 383-+.
1573 https://doi.org/10.1038/nature16156

1574 Mongwe, N. P., Vichi, M., & Monteiro, P. M. S. (2018). The seasonal cycle of pCO_2 and CO_2
1575 fluxes in the Southern Ocean: diagnosing anomalies in CMIP5 Earth system models.
1576 *Biogeosciences*, *15*(9), 2851–2872. https://doi.org/10.5194/bg-15-2851-2018

1577 Nakano, H., Tsujino, H., Hirabara, M., Yasuda, T., Motoi, T., Ishii, M., & Yamanaka, G.
1578 (2011). Uptake mechanism of anthropogenic CO_2 in the Kuroshio Extension region in
1579 an ocean general circulation model. *Journal of Oceanography*, *67*(6), 765–783.
1580 https://doi.org/10.1007/s10872-011-0075-7

1581 Nevison, C. D., Manizza, M., Keeling, R. F., Stephens, B. B., Bent, J. D., Dunne, J., et al.
1582 (2016). Evaluating CMIP5 ocean biogeochemistry and Southern Ocean carbon uptake
1583 using atmospheric potential oxygen: Present-day performance and future projection.
1584 *Geophysical Research Letters*, *43*(5), 2077–2085.
1585 https://doi.org/10.1002/2015gl067584

1586 Orr, J. C., Maier-Reimer, E., Mikolajewicz, U., Monfray, P., Sarmiento, J. L., Toggweiler, J.
1587 R., et al. (2001). Estimates of anthropogenic carbon uptake from four three-
1588 dimensional global ocean models. *Global Biogeochemical Cycles*, *15*(1), 43–60.
1589 https://doi.org/10.1029/2000gb001273

1590 Pfeil, B., Olsen, A., Bakker, D. C. E., Hankin, S., Koyuk, H., Kozyr, A., et al. (2013). A
1591 uniform, quality controlled Surface Ocean CO_2 Atlas (SOCAT). *Earth System Science*
1592 *Data*, *5*(1), 125–143. https://doi.org/10.5194/essd-5-125-2013

1593 Pilcher, D. J., Brody, S. R., Johnson, L., & Bronselaer, B. (2015). Assessing the abilities of
1594 CMIP5 models to represent the seasonal cycle of surface ocean pCO_2. *Journal of*
1595 *Geophysical Research-Oceans*, *120*(7), 4625–4637.
1596 https://doi.org/10.1002/2015jc010759

1597 Riahi, K., van Vuuren, D. P., Kriegler, E., Edmonds, J., O'Neill, B. C., Fujimori, S., et al.
1598 (2017). The Shared Socioeconomic Pathways and their energy, land use, and
1599 greenhouse gas emissions implications: An overview. *Global Environmental Change-*

Human and Policy Dimensions, *42*, 153–168. https://doi.org/10.1016/j.gloenvcha.2016.05.009

Riebesell, U., Kortzinger, A., & Oschlies, A. (2009). Sensitivities of marine carbon fluxes to ocean change. *Proceedings of the National Academy of Sciences of the United States of America*, *106*(49), 20602–20609. https://doi.org/10.1073/pnas.0813291106

Rödenbeck, C., Keeling, R. F., Bakker, D. C. E., Metz, N., Olsen, A., Sabine, C., & Heimann, M. (2013). Global surface-ocean pCO_2 and sea-air CO_2 flux variability from an observation-driven ocean mixed-layer scheme. *Ocean Science*, *9*(2), 193–216. https://doi.org/10.5194/os-9-193-2013

Rödenbeck, C., Bakker, D. C. E., Gruber, N., Iida, Y., Jacobson, A. R., Jones, S., et al. (2015). Data-based estimates of the ocean carbon sink variability - first results of the Surface Ocean pCO_2 Mapping intercomparison (SOCOM). *Biogeosciences*, *12*(23), 7251–7278. https://doi.org/10.5194/bg-12-7251-2015

Rödenbeck, C., DeVries, T., Hauck, J., Le Quéré, C., & Keeling, R. F. (2022). Data-based estimates of interannual sea–air CO_2 flux variations 1957–2020 and their relation to environmental drivers. *Biogeosciences*, *19*(10), 2627–2652.

Rodgers, K. B., Sarmiento, J. L., Aumont, O., Crevoisier, C., Montegut, C. D., & Metzl, N. (2008). A wintertime uptake window for anthropogenic CO_2 in the North Pacific. *Global Biogeochemical Cycles*, *22*(2), 16. https://doi.org/10.1029/2006gb002920

Rodgers, K. B., Aumont, O., Fletcher, S. E. M., Plancherel, Y., Bopp, L., Montegut, C. D., et al. (2014). Strong sensitivity of Southern Ocean carbon uptake and nutrient cycling to wind stirring. *Biogeosciences*, *11*(15), 4077–4098. https://doi.org/10.5194/bg-11-4077-2014

Rodgers, K. B., Lin, J., & Frolicher, T. L. (2015). Emergence of multiple ocean ecosystem drivers in a large ensemble suite with an Earth system model. *Biogeosciences*, *12*(11), 3301–3320. https://doi.org/10.5194/bg-12-3301-2015

Rodgers, K. B., Schlunegger, S., Slater, R. D., Ishii, M., Frolicher, T. L., Toyama, K., et al. (2020). Reemergence of Anthropogenic Carbon Into the Ocean's Mixed Layer Strongly Amplifies Transient Climate Sensitivity. *Geophysical Research Letters*, *47*(18), 9. https://doi.org/10.1029/2020gl089275

Rodgers, Keith B., Lee, S.-S., Rosenbloom, N., Timmermann, A., Danabasoglu, G., Deser, C., et al. (2021). Ubiquity of human-induced changes in climate variability. *Earth System Dynamics*, 12, 1393-1411, https://doi.org/10.5194/esd-12-1393-2021.

Roemmich, D., & Gilson, J. (2009). The 2004-2008 mean and annual cycle of temperature, salinity, and steric height in the global ocean from the Argo Program. *Progress in Oceanography*, *82*(2), 81–100. https://doi.org/10.1016/j.pocean.2009.03.004

Sabine, C. L., Feely, R. A., Gruber, N., Key, R. M., Lee, K., Bullister, J. L., et al. (2004). The oceanic sink for anthropogenic CO_2. *Science*, *305*(5682), 367–371. https://doi.org/10.1126/science.1097403

Sarmiento, J. L., & Gruber, N. (2006). *Ocean biogeochemical dynamics*. Princeton University Press.

Schlunegger, S., Rodgers, K. B., Sarmiento, J. L., Frolicher, T. L., Dunne, J. P., Ishii, M., & Slater, R. (2019). Emergence of anthropogenic signals in the ocean carbon cycle. *Nature Climate Change*, 9(9), 719–725. https://doi.org/10.1038/s41558-019-0553-2

Schlunegger, S., Rodgers, K. B., Sarmiento, J. L., Ilyina, T., Dunne, J. P., Takano, Y., et al. (2020). Time of Emergence and Large Ensemble Intercomparison for Ocean Biogeochemical Trends. *Global Biogeochemical Cycles*, 34(8), 18. https://doi.org/10.1029/2019gb006453

Schwinger, J., Goris, N., Tjiputra, J. F., Kriest, I., Bentsen, M., Bethke, I., et al. (2016). Evaluation of NorESM-OC (versions 1 and 1.2), the ocean carbon-cycle stand-alone configuration of the Norwegian Earth System Model (NorESM1). *Geoscientific Model Development*, *9*(8), 2589–2622. https://doi.org/10.5194/gmd-9-2589-2016

Séférian, R. (2018). CNRM-CERFACS CNRM-ESM2-1 model output prepared for CMIP6 CMIP. *Earth System Grid Federation*, *10*.

Séférian, R., Delire, C., Decharme, B., Voldoire, A., Melia, D. S. Y., Chevallier, M., et al. (2016). Development and evaluation of CNRM Earth system model - CNRM-ESM1. *Geoscientific Model Development*, *9*(4), 1423–1453. https://doi.org/10.5194/gmd-9-1423-2016

Séférian, R., Nabat, P., Michou, M., Saint-Martin, D., Voldoire, A., Colin, J., et al. (2019). Evaluation of CNRM Earth System Model, CNRM-ESM2-1: Role of Earth System Processes in Present-Day and Future Climate. *Journal of Advances in Modeling Earth Systems*, *11*(12), 4182–4227. https://doi.org/10.1029/2019ms001791

Seland, Ø. ., Bentsen, M., Olivie, D., Toniazzo, T., Gjermundsen, A., Graff, L. S., et al. (2020). Overview of the Norwegian Earth System Model (NorESM2) and key climate response of CMIP6 DECK, historical, and scenario simulations. *Geoscientific Model Development*, *13*(12), 6165–6200. https://doi.org/10.5194/gmd-13-6165-2020

Sellar, A. A., Jones, C. G., Mulcahy, J. P., Tang, Y. M., Yool, A., Wiltshire, A., et al. (2019). UKESM1: Description and Evaluation of the UK Earth System Model. *Journal of Advances in Modeling Earth Systems*, *11*(12), 4513–4558. https://doi.org/10.1029/2019ms001739

Stock, C. A., Dunne, J. P., Fan, S. M., Ginoux, P., John, J., Krasting, J. P., et al. (2020). Ocean Biogeochemistry in GFDL's Earth System Model 4.1 and Its Response to Increasing Atmospheric CO_2. *Journal of Advances in Modeling Earth Systems*, *12*(10). https://doi.org/10.1029/2019ms002043

Swart, N. C., Cole, J. N., Kharin, V. V., Lazare, M., Scinocca, J. F., & Gillett, N. P. (2019a). CCCma CanESM5 model output prepared for CMIP6 CMIP historical. Version 20190429. *Earth System Grid Federation*.

Swart, N. C., Cole, J. N. S., Kharin, V. V., Lazare, M., Scinocca, J. F., Gillett, N. P., et al. (2019b). The Canadian Earth System Model version 5 (CanESM5.0.3). *Geoscientific Model Development*, *12*(11), 4823–4873. https://doi.org/10.5194/gmd-12-4823-2019

Takahashi, T., Olafsson, J., Goddard, J. G., Chipman, D. W., & Sutherland, S. C. (1993). Seasonal Variation of CO_2 and Nutrients in the High-Latitude Surface Oceans: A Comparative Study. *Global Biogeochemical Cycles*, *7*(4), 843–878. https://doi.org/10.1029/93gb02263

Takahashi, T., Sutherland, S. C., Sweeney, C., Poisson, A., Metzl, N., Tilbrook, B., et al. (2002). Global sea-air CO_2 flux based on climatological surface ocean pCO_2, and seasonal biological and temperature effects. *Deep-Sea Research Part II: Topical Studies in Oceanography*, *49*(9–10), 1601–1622. https://doi.org/10.1016/s0967-0645(02)00003-6

Tang, Y., Rumbold, S., Ellis, R., Kelley, D., Mulcahy, J., Sellar, A., et al. (2019). MOHC UKESM1. 0-LL model output prepared for CMIP6 CMIP historical. *Earth System Grid Federation*, *10*.

Tjiputra, J. F., Olsen, A., Assmann, K., Pfeil, B., & Heinze, C. (2012). A model study of the seasonal and long–term North Atlantic surface pCO_2 variability. *Biogeosciences*, *9*(3), 907–923.

Urakawa, L. S., Tsujino, H., Nakano, H., Sakamoto, K., Yamanaka, G., & Toyoda, T. (2020). The sensitivity of a depth-coordinate model to diapycnal mixing induced by practical implementations of the isopycnal tracer diffusion scheme. *Ocean Modelling*, *154*, 101693.

Watson, A. J., Schuster, U., Shutler, J. D., Holding, T., Ashton, I. G. C., Landschutzer, P., et al. (2020). Revised estimates of ocean-atmosphere CO_2 flux are consistent with ocean carbon inventory. *Nature Communications*, *11*(1), 6. https://doi.org/10.1038/s41467-020-18203-3

Wright, R. M., Le Quéré, C., Buitenhuis, E., Pitois, S., & Gibbons, M. J. (2021). Role of jellyfish in the plankton ecosystem revealed using a global ocean biogeochemical model. *Biogeosciences*, *18*(4), 1291–1320.

Yang, S., & Gruber, N. (2016). The anthropogenic perturbation of the marine nitrogen cycle by atmospheric deposition: Nitrogen cycle feedbacks and the ^{15}N Haber-Bosch effect. *Global Biogeochemical Cycles*, *30*(10), 1418–1440.

Yukimoto, S., Koshiro, T., Kawai, H., Oshima, N., Yoshida, K., Urakawa, S., et al. (2019a). MRI MRI-ESM2. 0 model output prepared for CMIP6 CMIP historical. *Earth System Grid Federation*, *10*.

Yukimoto, S., Kawai, H., Koshiro, T., Oshima, N., Yoshida, K., Urakawa, S., et al. (2019b). The Meteorological Research Institute Earth System Model version 2.0, MRI-ESM2. 0: Description and basic evaluation of the physical component. *Journal of the Meteorological Society of Japan. Ser. II*, *97*(5), 931–965.

Yun, J., Jeong, S., Gruber, N., Gregor, L., Ho, C.-H., Piao, S., et al. (2022). Enhance seasonal amplitude of atmospheric CO_2 by the changing Southern Ocean carbon sink. *Science Advances*, *8*(41), eabq0220.

Zeng, J., Matsunaga, T., & Shirai, T. (2022). A new estimate of oceanic CO_2 fluxes by machine learning reveals the impact of CO_2 trends in different methods. *Earth System Science Data Discussions*, 1–27.

Ziehn, T., Chamberlain, M., Lenton, A., Law, R., Bodman, R., Dix, M., et al. (2019). CSIRO ACCESS-ESM1. 5 model output prepared for CMIP6 CMIP historical, Earth System Grid Federation.

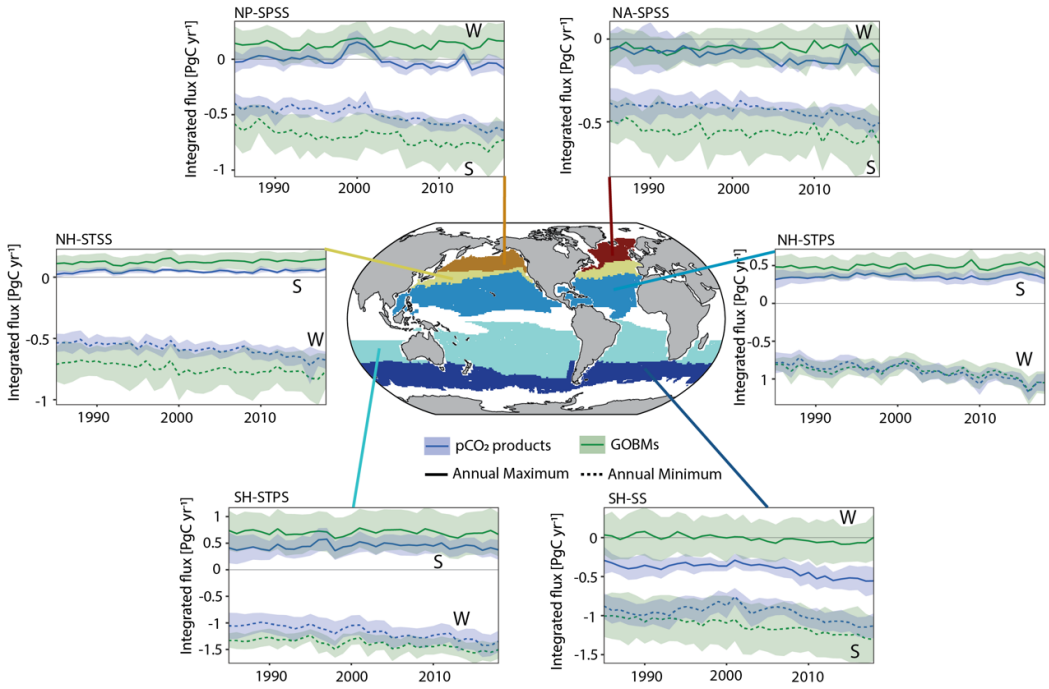

Fig. 1: Central panel showing biomes used for this study (see **Table 1** for details): North Atlantic subpolar seasonally stratified (NA-SPSS), North Pacific subpolar seasonally stratified (NP-SPSS), Northern Hemisphere subtropical seasonally stratified (NH-STSS), Northern Hemisphere subtropical permanently stratified (NH-STPS), Southern Hemisphere subtropical permanently stratified (SH-STPS), and Southern Hemisphere seasonally stratified, incorporating the subpolar and subtropical components (SH-SS). Surrounding panels show time series plots of biome-integrated sea-air CO_2 fluxes (annual maximum and minimum values irrespective of the month of occurrence). pCO_2 products (blue) and GOBMs (green) are shown for both the ensemble mean (bold) and for one standard deviation (shaded). Positive (negative) values indicate outgassing (ingassing) of CO_2. The regions in white in the central panel are not included in this analysis., in each panel, winter is designated by W, and summer by S, in order to distinguish the seasonal phasing between the subtropical and subpolar/Southern Ocean biomes.

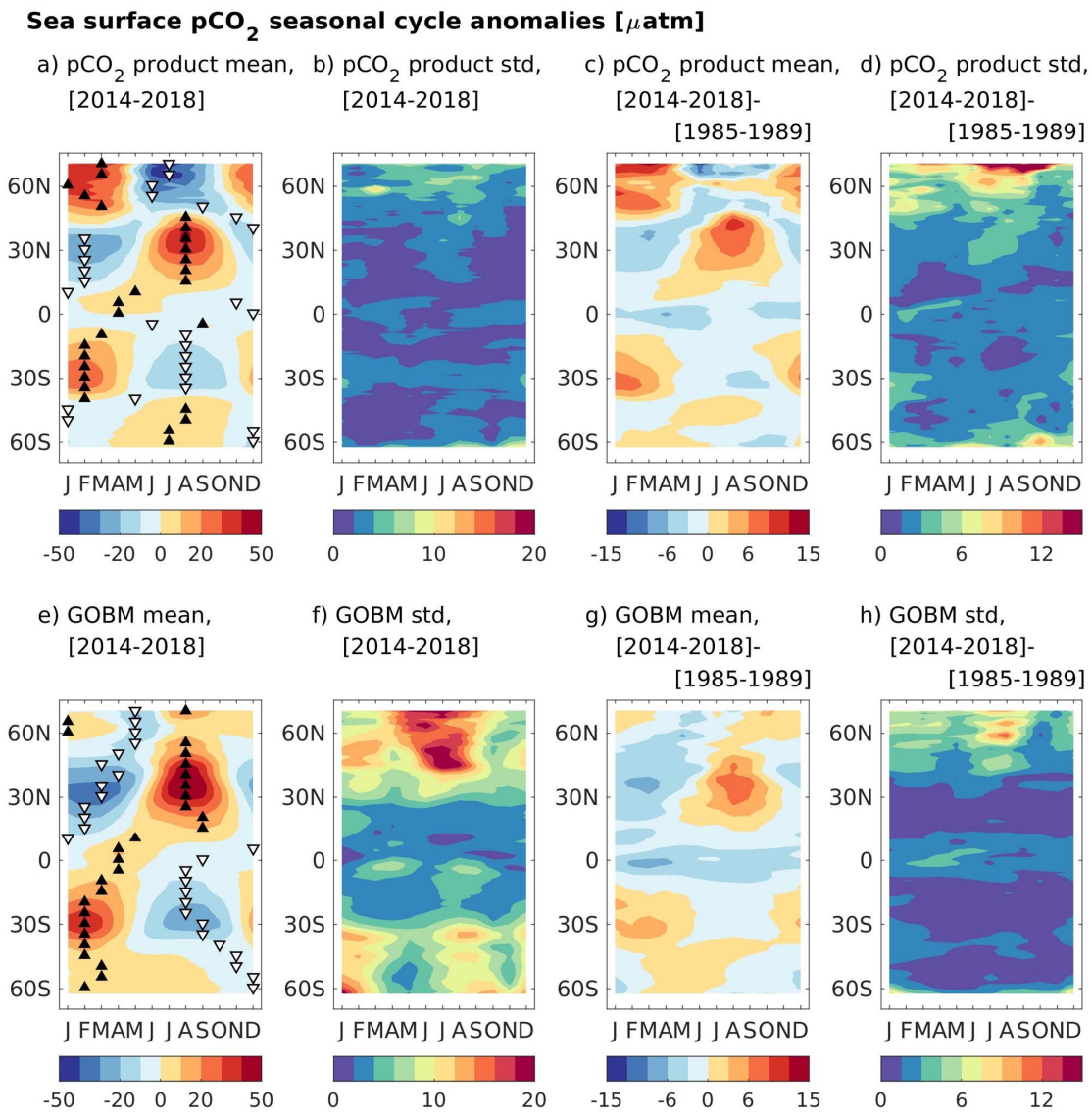

Fig. 2: Hovmöller diagrams of zonally-averaged climatological (2014-2018) pCO_2 anomalies for pCO_2 products (a) and GOBMs (e), and corresponding standard deviations (b, f); multi-decadal change in pCO_2 climatology between 1985-1989 and 2014-2018 for pCO_2 products (c) and GOBMs (g) and corresponding standard deviation (d, h). The seasonal maxima (black triangles) and minima (white triangles) are highlighted in panels a and e. Anomalies were calculated, grid-point by grid-point, by first fitting a quadratic polynomial through the full monthly time series over the period 1985-2018 and removing this trend from the data. Then, mean pCO_2 values over 1985-1989 and 2014-2018 were calculated for each month as a deviation from the detrended mean pCO_2 over the whole five year period.

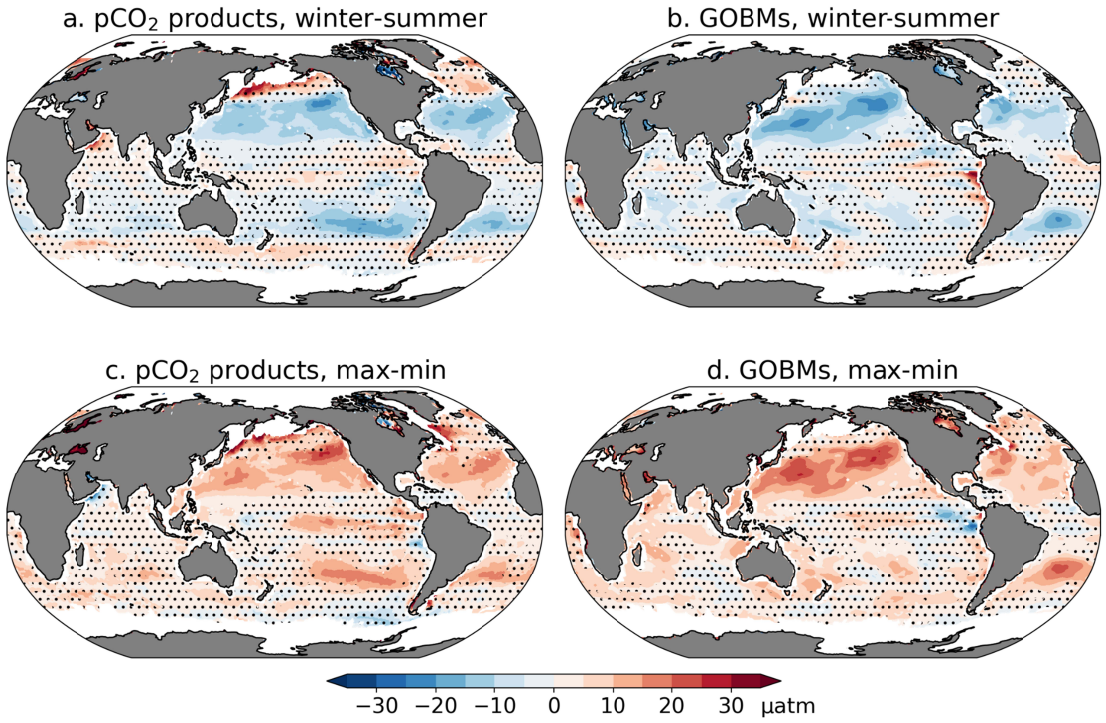

Fig. 3: Multi-decadal changes in the pCO_2 seasonal amplitude between the two five-year periods 1985-1989 and 2014-2018, for (a,c) pCO_2 products and (b,d) GOBMs. For panels a and b, seasonal amplitude is calculated as a winter-minus-summer difference, where winter and summer are defined as JFM and JAS (JAS and JFM) for the Northern (Southern) Hemisphere, respectively. For panels c and d seasonal amplitude is calculated as maximum-minus-minimum. Dotted regions indicate where the spread of the ensemble members (STD=1 level) is larger than the ensemble mean multi-decadal change. For this analysis, the nine pCO_2 products listed in **Table 2** and the 11 GOBMs in **Table 3** (excluding OCIM) are used. The sensitivity to the choice of five-year versus 10-year versus 15-year averaging for characterizing decadal changes is displayed in **Fig. S3**.

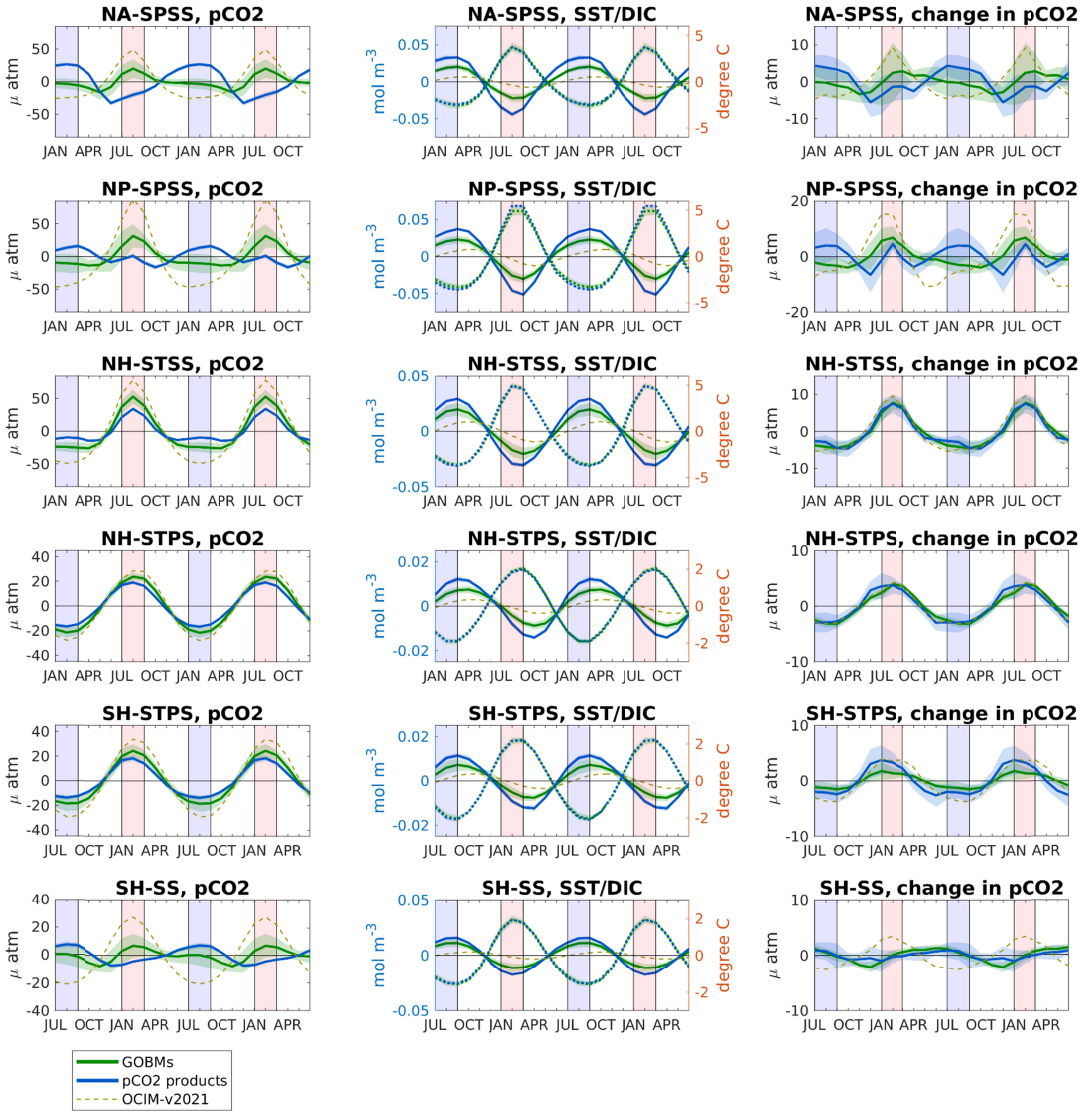

Fig. 4: Climatological seasonal cycle anomalies for 2014-2018 for pCO_2 (left column), SST (center column, dashed) and DIC (center column, solid), and change in pCO_2 seasonale cycle anomalies between 1985-1989 and 2014-2018 (right column) over the six aggregated biomes for GOBMs (green), pCO_2 products (blue), and for OCIM (brown, dashed). The biome names as defined in **Table 1** and **Fig. 1** are given in each panel title. Ensemble means for GOBMs and pCO_2 products are shown as thick lines while the shading indicates the standard deviation around the mean. Note the different scales of the left and right columns, and that the Southern Hemisphere sub-plots begin with the month of July.

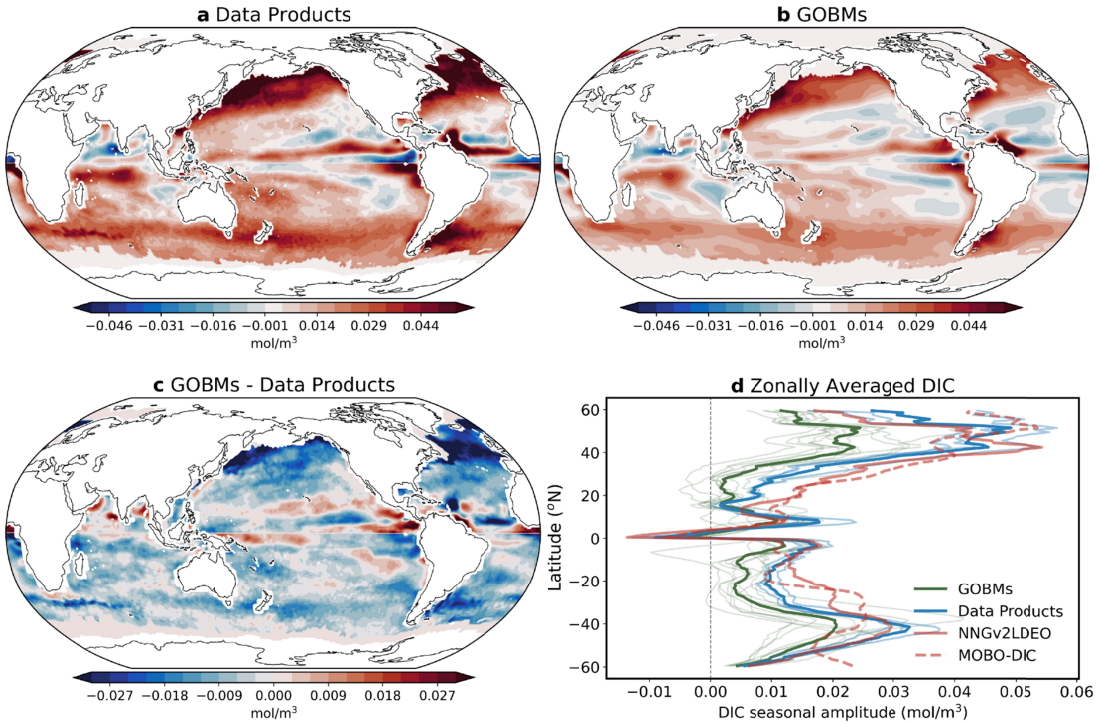

Fig. 5: Climatological seasonal amplitudes in surface DIC concentrations over 2014-2018 considered as winter-minus-summer (JFM-JAS for the Northern Hemisphere and JAS-JFM for the Southern Hemisphere) for (a) the average of three pCO_2/TA (DIC) products (JMAMLR, CMEMS-LSCE-FFNN, and OceanSODA-ETHZ), (b) the average across 11 GOBMs, and (c) the difference between (b) and (a), where negative (positive) values indicate that GOBMs under-represent (over-represent) the climatological seasonal amplitude of DIC variability. (d) shows latitudinal averages for GOBMs (green) and data products (blue), where bold lines represent product averages, and light lines indicate individual products. Also shown in (d) are MOBO-DIC (red dashed) and NNGv2LDEO (red solid). The MOBO-DIC climatology corresponds to the period 2004 through 2017 and NNGv2LDEO to 1995.

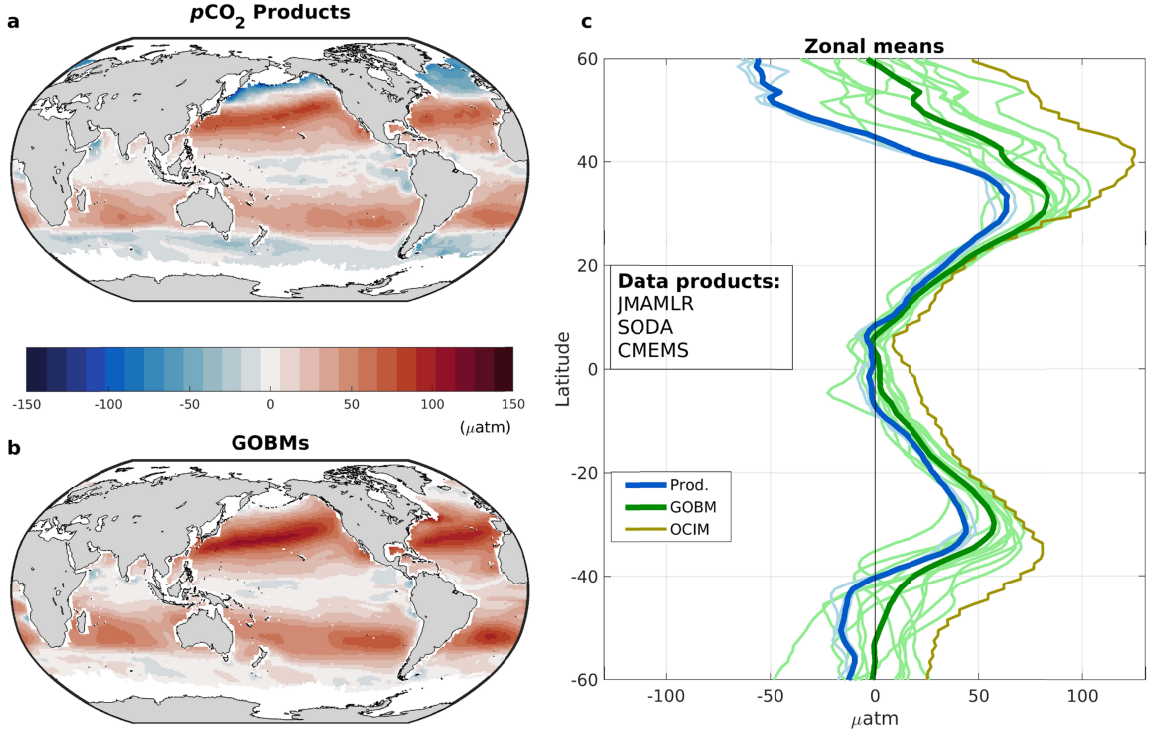

Fig. 6: Ensemble mean difference between the thermal and nonthermal pCO_2 component of its seasonal cycle amplitude (ΔA) for (**a**) the three pCO_2 products that include associated DIC and TA products (JMAMLR, OceanSODA-ETHZ, and CMEMS-LSCE-FFNN and (**b**) 11 GOBMs. (**c**) Zonal mean of ΔA values for GOBMs and pCO_2 products with bold lines showing the ensemble mean values. The olive-colored line shows the abiotic OCIM model, which is not included in the model ensemble mean. pCO_2 component seasonal cycle amplitudes were computed as the absolute value of the difference between the winter minus summer seasonal averages over 2014-2018. For each case the separation into thermal and nonthermal components follows the approach of *Fassbender et al.* (2022), where a carbon system calculator (CO2SYS) is used to quantify the thermal component, and thereby the nonthermal component via difference from the full pCO_2 annual cycle. Seasons are defined as JFM and JAS.

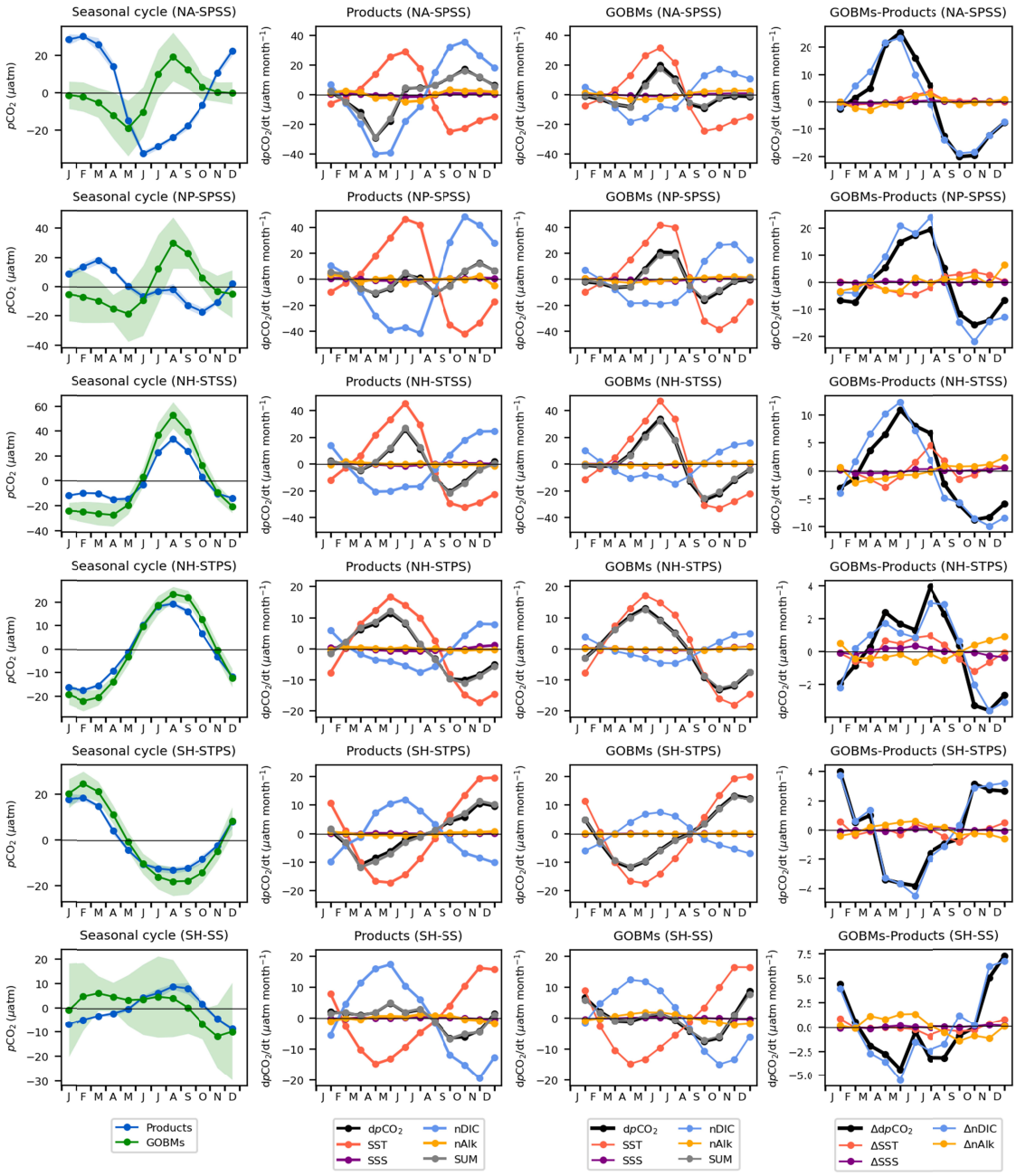

Fig. 7: Decomposition of the seasonality drivers for pCO_2 products and GOBMs (one standard deviation shading for GOBMs) for all six biomes. The 2014-2018 climatological seasonal cycle of pCO_2 (left column) is decomposed into month-to-month changes due to two physical (SST (orange) and SSS (purple)) and two biogeochemical (salinity-normalized DIC (nDIC, blue) and salinity-normalized TA (nAlk, yellow)) drivers (2nd and 3rd column). The

observational products are the three products that include DIC and TA, namely JMAMLR, OceanSODA-ETHZ, and CMEMS-LSCE-FFNN. Calculations are performed first individually on each product or GOBM, and subsequently averaged to arrive at a mean respectively for the observation-based products and GOBMs. The differences in the drivers between the pCO_2 products and the GOBMs are shown in the right column - note the differences in scale. The drivers are identified via Taylor Series decomposition using PYCO2SYS to calculate the coefficients for DIC and TA, and using constant values for SST and SSS ($d\ln pCO_2/dT=0.0423°C^{-1}$ and $d\ln pCO_2/d\ln S=1$) as in *Sarmiento and Gruber* (2006). For pCO_2 itself (left column) the monthly dots are positioned mid-month, mid-way between tick marks. For tendencies (columns two and three) dots are located at the end of the month, so on tick marks. SUM in columns two and three represents the sum of the four underlying tendencies.

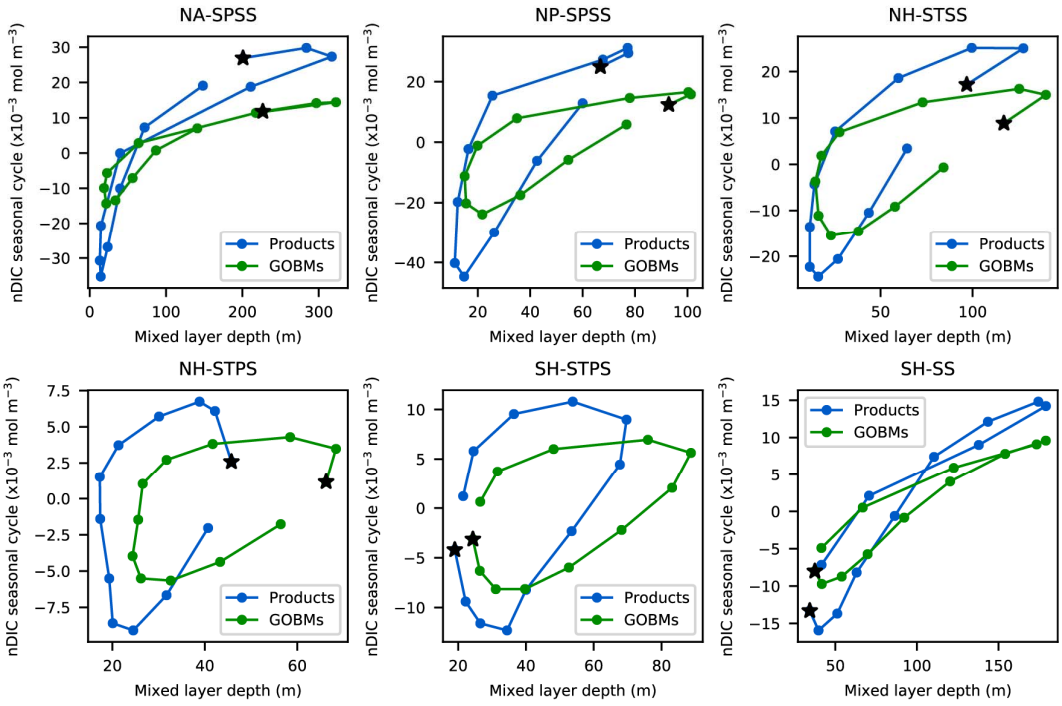

Fig. 8: Seasonal evolution of the relationship between MLD and anomalies of nDIC over the six biomes for a climatology over 2014-2018 for observation-based products (blue) and GOBMs (green). The stars indicate January. The pCO_2 products that include DIC and TA, namely JMAMLR, OceanSODA-ETHZ, and CMEMS-LSCE-FFNN, are considered along with the full suite of 11 GOBMs. Observationally-based MLDs have been derived for this study from the gridded Argo-derived temperature and salinity product of *Roemmich and Gilson* (2009) using a density threshold criterion (*Holte and Talley*, 2009) using the years 2014-2018, for consistency with the nDIC fields.

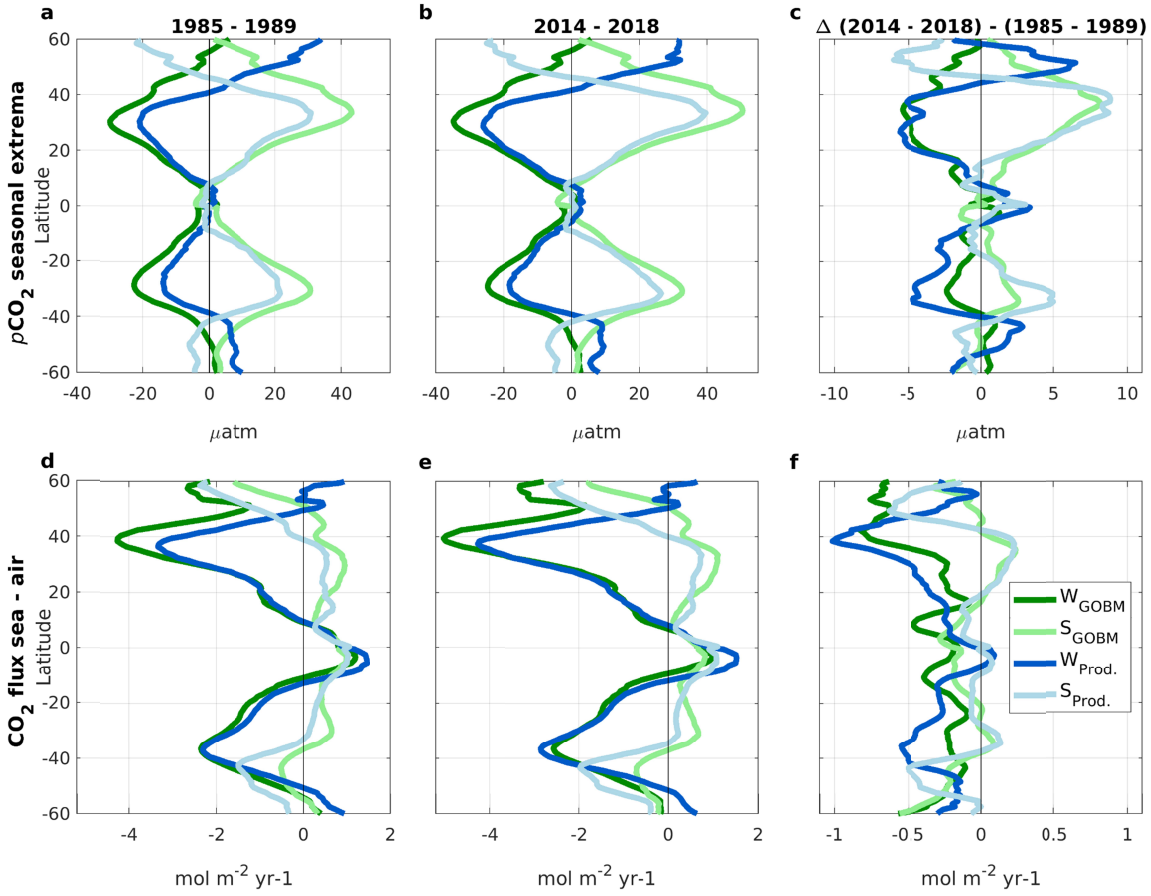

Fig. 9: Mean summer (S) and winter (W) (**a-c**) surface pCO_2 anomalies and (**d-f**) CO_2 sea-to-air flux. Results for the 1985-1989 period, 2014-2018 period, and the difference between periods (Δ) are shown in separate columns. Sea pCO_2, seasonal anomalies are calculated relative to the annual mean computed from annual means of temperature, salinity, dissolved inorganic carbon, total alkalinity, and nutrients for each year ($pCO_{2\ AM}$). Different magnitudes in the multi-decadal changes for each season (panel c) reflect asymmetry in the pCO_2 seasonal cycle change. Ensemble mean GOBM changes are shown in green hues (11 models listed in **Table 3**, excluding OCIM). Ensemble mean pCO_2 product (Prod.) changes are shown in blue hues (same pCO_2 products as in **Fig. 6**). Seasons are defined as JFM and JAS.

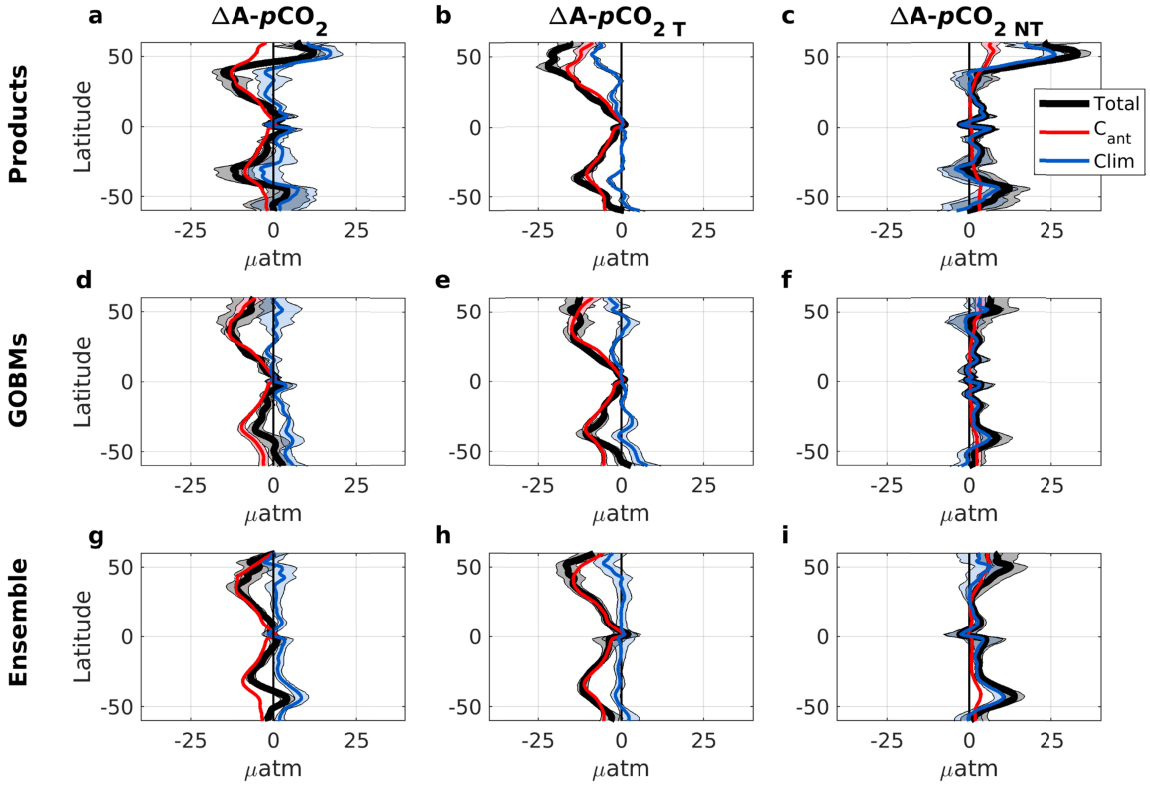

Fig. 10: Mean change in the seasonal cycle amplitude (winter minus summer) of pCO_2 and its thermal (T) and nonthermal (NT) components from the period 1985-1989 to the period 2014-2018. Changes are broken down into the total change and the portion of the change attributed to the accumulation of anthropogenic carbon (C_{ant}) versus climate (Clim: changes to the ocean physical or biogeochemical state caused by anthropogenic climate change). The top, middle, and bottom rows show the ensemble mean results for the three pCO_2 products, the eleven GOBMs listed in **Table 3**, and the CESM2 large ensemble, respectively. Shading reflects the standard deviation across the pCO_2 products, GOBMs, and ensemble members. Seasons are defined as JFM and JAS.

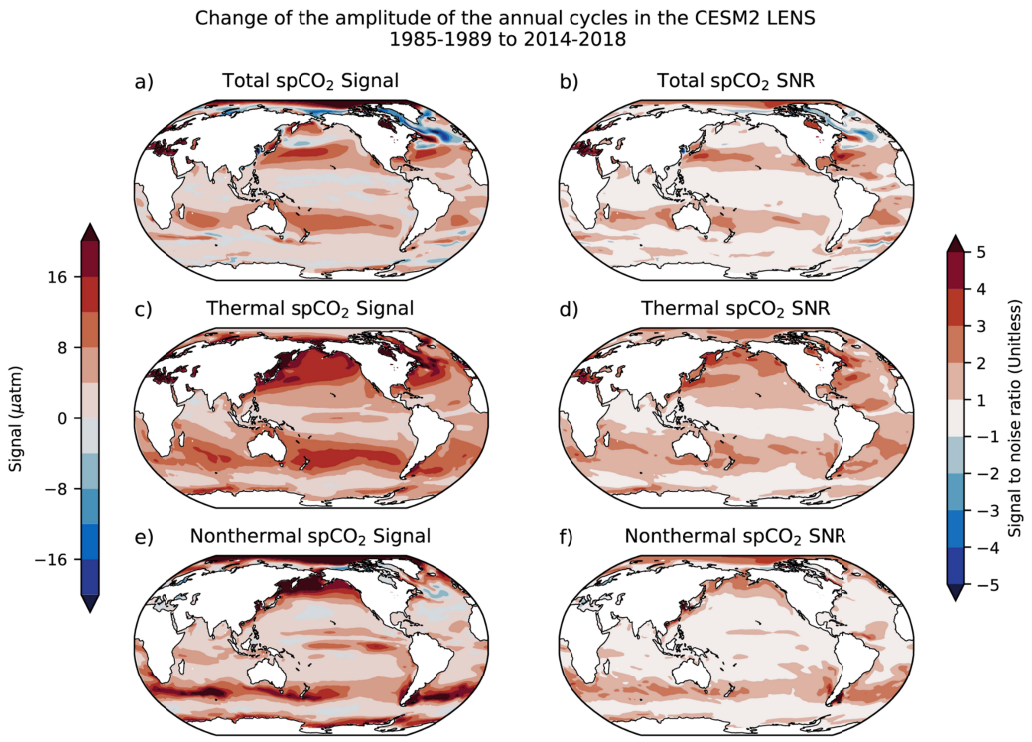

Fig. 11: Multi-decadal changes in pCO_2 seasonality between 1985-1989 and 2014-2018 (left column) and signal-to-noise ratio (SNR) maps for pCO_2 seasonality changes between 1985-1989 and 2014-2018 (right column). For each case, the seasonal amplitude is defined as the absolute value of the difference between JFM and JAS averages of pCO_2 in the model, such that negative values indicate decreasing amplitude. (a) the full decadal change in pCO_2 seasonal amplitude, (b) the SNR for the full pCO_2 signal, (c) the absolute value of the change in the thermal component of pCO_2 seasonal amplitude, (d) the SNR for the thermal component change, (e) the absolute value of the change in the nonthermal component, and (f) the SNR for the nonthermal component. All fields are from the CESM2 large ensemble (50 members). For each ensemble member, the change in the amplitude of the annual cycle was measured by (i) detrending the 1985-2018 time series by subtracting a quadratic polynomial fit, (ii) calculating the annual cycle strength as the absolute value of the JFM-JAS difference in pCO_2 for each year, (iii) averaging the five yearly values for each period, and (iv) subtracting the average over the earlier period from the average over the later period. For the full pCO_2 seasonal cycle, (i) the signal is defined as the ensemble mean change, and (ii) the

noise as the ensemble standard deviation, and (iii) the SNR indicates the confidence levels for emergence. This is done analogously for the thermal component of seasonality changes for (iv) the signal, (v) the noise, and (vi) the confidence intervals for emergence. Likewise for the nonthermal component, (vii) the signal, (viii) the noise, and (ix) the confidence intervals for emergence. Absolute magnitudes are chosen to emphasize the strength of the signal, so that the thermal and nonthermal fields in the left column do not necessarily sum to the total pCO_2 signal. The decomposition of the thermal and nonthermal components of the pCO_2 seasonal cycle is described in the Appendix.

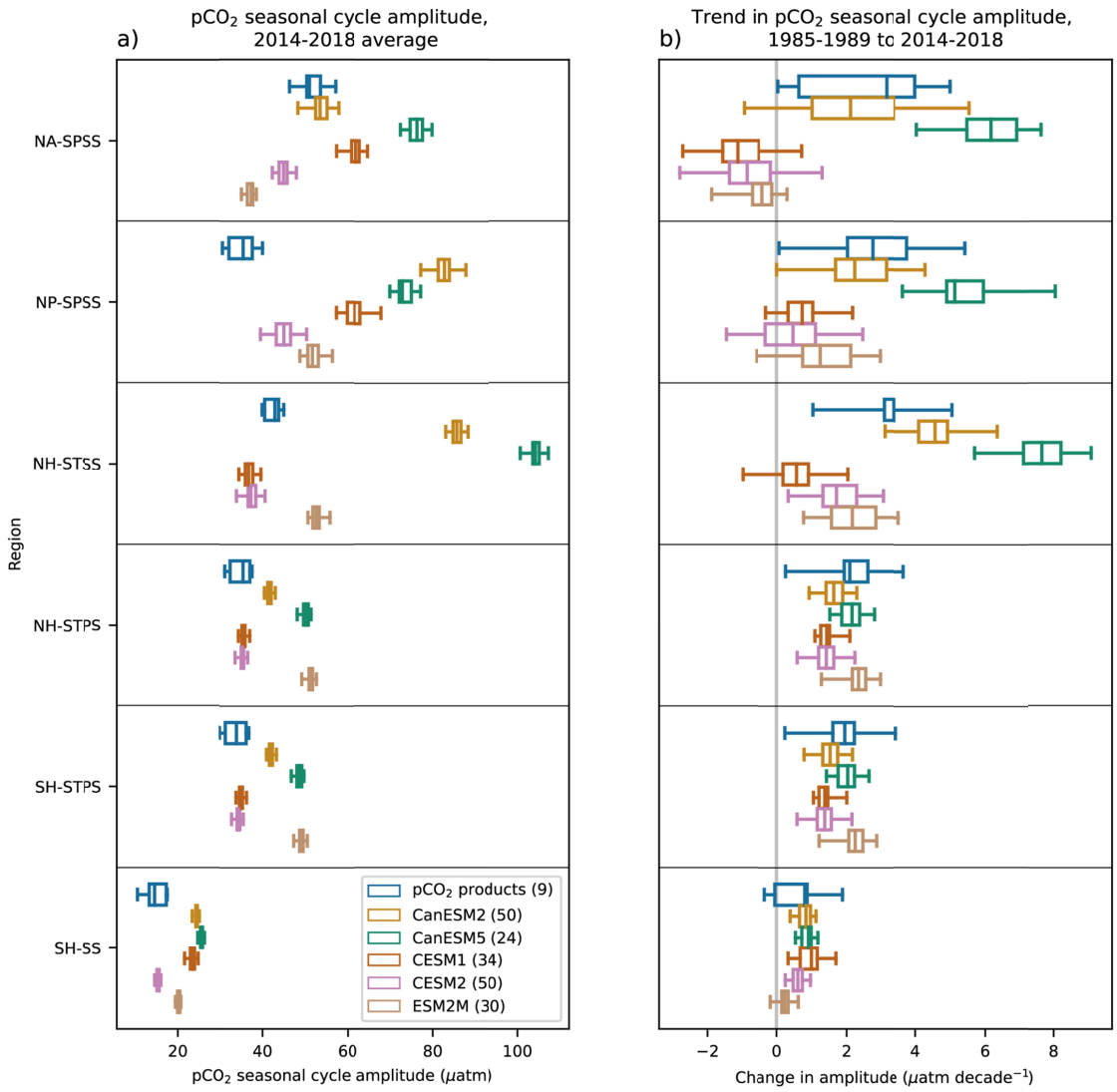

Fig. 12: Box plots of the absolute amplitude of the sea surface pCO_2 seasonal cycle for the period 2014-2018 (left) and the change in the amplitude of the pCO_2 seasonal cycle between 1985-1989 and 2014-2018 (right) based on pCO_2 products (blue) and five large ensemble experiments. For the large ensemble experiments, the number of ensemble members used for each model is shown in parentheses in the legend. The seasonal cycle amplitude is calculated as the absolute value of biome-averaged winter-minus-summer differences (JFM-JAS and JAS-JFM for the Northern and Southern Hemisphere, respectively). The boxes show the values between the first quartile (25%) and the third quartile (75%) with a line at the median (50%), with the whiskers indicating the minimum and maximum values. Note that for the pCO_2 products, the uncertainty range reflects uncertainty between the available nine

observational pCO_2 products, whereas the uncertainty range for the large ensemble simulations indicates natural climate variability as simulated by each model. For each ensemble member and data product, the change of the amplitude of the seasonal cycle for each region was measured by (i) detrending the 1985-2018 time series by subtracting a quadratic polynomial fit, (ii) calculating the seasonal cycle amplitude as the winter-minus-summer pCO_2 values for each year, (iii) averaging the five yearly values for each period, (iv) subtracting the earlier period average from the latter, and (v) calculating the spatial mean with latitude weighting. The amplitude of the seasonal cycle in 1985-1989 was obtained in step (iii). For each biome the sequencing of the colors is identical to the sequencing in the legend.

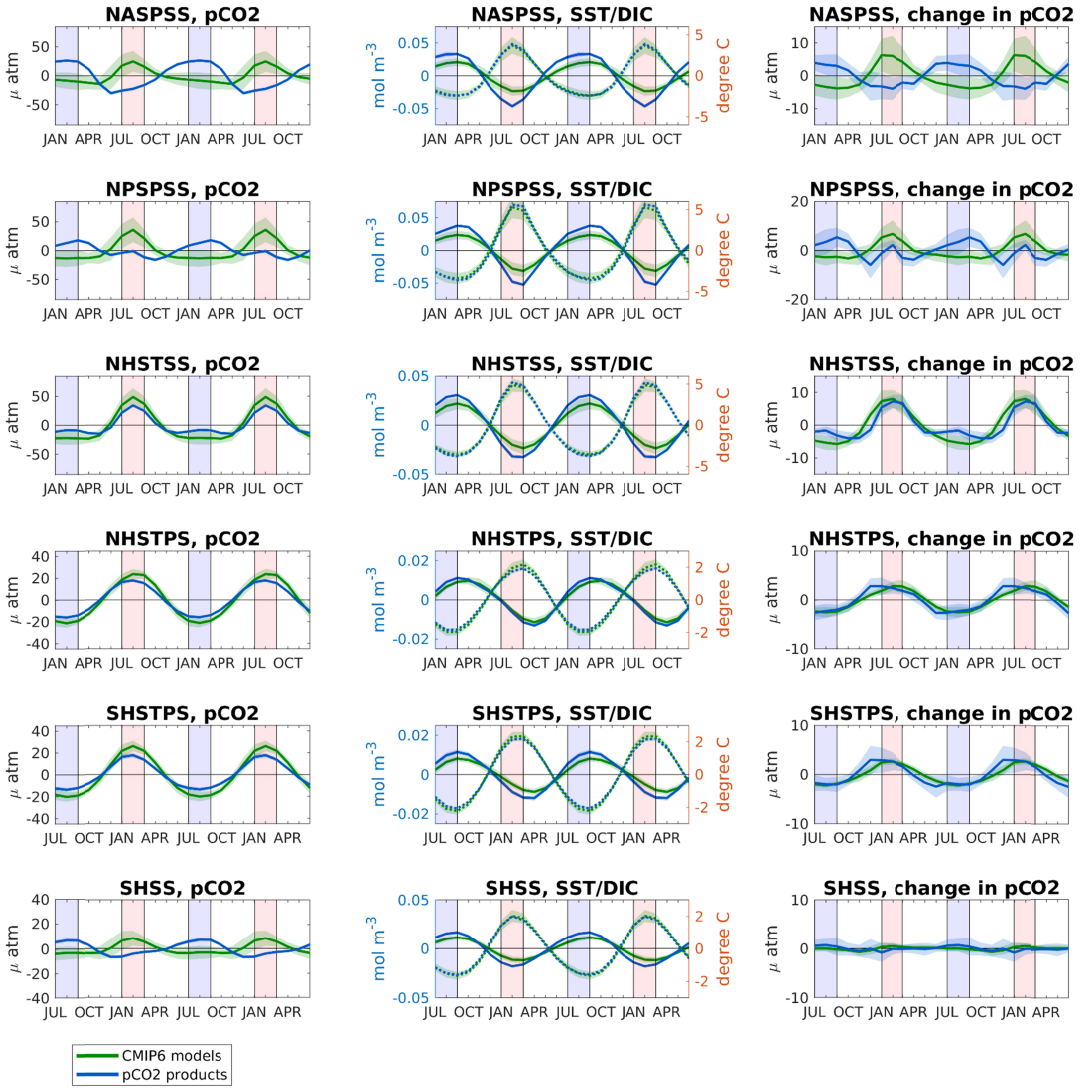

Fig. 13: Same as **Fig. 4** but with CMIP6 models as listed in **Table 6.** Note that the climatologies for pCO_2 (left column) and both DIC and SST (middle column) are taken over the years 2010-2014 (last five years of the CMIP6 historical simulations) and that the change in pCO_2 seasonality (right column) is calculated as the difference between 2010-2014 and 1985-1989.

Seasonal variability of the surface ocean carbon cycle: a synthesis

Supplementary Materials

Draft: April 3rd 2023

Keith B. Rodgers[1,2,*,†], Jörg Schwinger[3,*,†], Andrea J. Fassbender[4,†], Peter Landschützer[5], Ryohei Yamaguchi[6,†], et al.

† principal scientific contribution

* corresponding authors: keithbrodgers@gmail.com, jrsc@norceresearch.no

1. Center for Climate Physics, Institute for Basic Science, Busan, Republic of Korea
2. Pusan National University, Busan, Republic of Korea
3. NORCE Climate & Environment, Bjerknes Centre for Climate Research, Bergen, Norway
4. NOAA/OAR Pacific Marine Environmental Laboratory, Seattle, USA
5. Flanders Marine Institute (VLIZ), Oostende, Belgium
6. Japan Agency for Marine-Earth Science and Technology, Yokosuka, Japan

Surface DIC products associated with pCO_2 products

Here we provide more details on the pCO_2/TA products that provide time-varying surface DIC. These have been provided for CMEMS-LSCE, OceanSODA-ETHZ, and JMAMLR.

For CMEMS-LSCE, surface ocean DIC is calculated by using the CO2SYS speciation software (Lewis & Wallace, 1998; Van Heuven et al., 2011) given the reconstructions of pCO_2 and TA, nutrient concentrations (silicate, nitrate, phosphate), physical variables (SST and SSS), and dissociation constants. Total dissociation constants follow the best practices of (Dickson, 2010), wherein K_1 and K_2 are from Lueker et al. (2000). K_{HSO4} is from Dickson et al. (1990), and the formulation of boron to salinity ratio is from Uppstrom (1974). Details of the algorithms and derivations are documented in Chau et al. (2022). TA is derived from LIAR (Carter et al., 2018) - an approach of multiple linear regressions.

For OceanSODA-ETHZ, TA is (equivalent to the sea surface pCO_2) estimated using ensembles of two-step cluster-regression approaches, using K-means clustering for the first step, and a combination of neural networks, gradient-boosted trees and support vector regression for the second step (Gregor & Gruber, 2021). K_1 and K_2 are from the Dickson and Millero (1987) refit of Mehrbach et al. (1973), as these constants had the lowest error for the pCO_2-TA pairing (Raimondi et al., 2019). The K_{HSO4} and boron-salinity ratios are consistent with the CMEMS-LSCE approach.

For the JMAMLR product, salinity-normalized DIC (nDIC) is calculated by coupling each set of pCO_2, SST and SSS in SOCATv2019 (Bakker et al., 2016) with monthly fields of surface ocean TA expressed as a function of sea surface dynamic height (SSDH) and SSS that was built on GLODAPv2.2019 (Olsen et al., 2019; Takatani et al., 2014). The dissociation constants used are those recommended in the best practices of Dickson (2010). They are then fitted by multiple linear regressions for respective ocean domains with explanatory variables such as SST, SSS, SSDH, chlorophyll, mixed layer depth and year of measurements to account for the trend of DIC increase due to anthropogenic CO_2 uptake. Monthly fields of surface ocean nDIC are derived by combining these empirical expressions of nDIC with data

sets of these explanatory variables derived from satellite measurements and an ocean data assimilation (Iida et al., 2021).

Three Dimensional DIC climatologies

Here we provide a brief overview of the three-dimensional DIC climatologies used to assess GOBM representation of vertical gradients in DIC. The two climatologies described below are MOBO-DIC and NNGv2LDEO, and they are both independent of the surface DIC products that are directly associated with the surface pCO_2 products described above.

An interior DIC climatology DP is provided from the Mapped Observation-Based Oceanic DIC (MOBO-DIC) product by Keppler et al. (2020a; 2020b). MOBO-DIC is a machine-learning-based approach, and is built on the same 2-step neural network method that has been used previously to reconstruct surface ocean pCO_2 for the SOM-FFN product by Landschützer et al. (2016) and adjusted to resolve DIC fields in the interior ocean. This two-step cluster-regression approach first divides the ocean into clusters using self-organizing maps (SOM), and then runs a feed-forward network (FFN) in each of the SOM-clusters. During the FFN step, this version of MOBO-DIC uses mapped observation-based temperature and salinity fields from the Argo program (Roemmich & Gilson, 2009) together with climatological nutrient and oxygen fields from the World Ocean Atlas (WOA18; *(Garcia et al., 2019)*) to obtain the statistical relationships between these predictor data and interior ocean DIC measurements from the GLODAPv2019 database (Olsen et al., 2019). These relationships are then applied to reconstruct gap-filled maps of the interior oceanic DIC. The differences between MOBO-DIC and the original SOM-FFN approach include that the target variable to be mapped is DIC (compared to pCO_2 in SOM-FFN), the fields have an additional dimension (depth), and different predictors are used due to data availability and different processes in the water column relative to the surface. In addition, this version of MOBO-DIC only resolves a monthly climatology (compared to monthly resolution in SOM-FFN). As a result of these differences, the structure of the networks differs in MOBO-DIC, with fewer clusters in the SOM-step, and fewer neurons in the FFN step. More information on the

method is provided in Keppler et all (2020a). This MOBO-DIC monthly climatology is at 1° horizontal resolution on 28 depth levels (2.5-2000 m), and is based on data from 2004 through 2017.

We also use the NNGv2LDEO monthly climatology of interior DIC by Broullón et al. (2020). This DIC product is based on a two-layer FFN neural network, that utilizes physical and biogeochemical predictor data from the World Ocean Atlas (WOA13; Garcia et al., 2013; Locarnini et al., 2013; Zweng et al., 2019), as well as information on the depth, horizontal location, and year of the measurement, to reconstruct gap-filled maps of the interior oceanic DIC. The relationship from predictors and DIC measurements is established through a combination of observation-based DIC measurements from GLDAPv2.2019 (Olsen et al., 2019) and DIC obtained from pCO2 from the Lamont Doherty Earth Observatory (LDEO) database (Takahashi et al., 2017), combined with TA from the NNGv2 neural network of Broullón et al. (2019). These NNGv2LDEO DIC fields are at 1° horizontal resolution, on 102 depth levels (0–5500 m), where the upper 1500 m resolve a monthly climatology and below 1500 m it is at annual resolution; the data are centered around the year 1995.

Attribution of discrepancies in the pCO_2 seasonal cycle phase and amplitude

In the main text section describing climatological pCO_2 seasonal cycle drivers, we applied the method of Fassbender et al. (2022), which is a modified version of the framework originally developed by Takahashi et al. (1993; 2002), where for each grid point local temperature and pCO_2 are used as follows to define the thermal ($pCO_{2\ T}$) and nonthermal ($pCO_{2\ NT}$) components of pCO_2 seasonal variability:

$$pCO_{2\,T} = pCO_{2\,am} * exp[0.0423\,(T_{mm} - T_{am})] \quad (1)$$

$$pCO_{2\,NT} = pCO_{2\,mm} * exp[0.0423\,(T_{am} - T_{mm})] \quad (2)$$

Within this approach the subscripts *am* and *mm* represent annual means and monthly means, respectively. However, one of the limitations of the method of Takahashi et al. (1993; 2002) is that the two components in (1) and (2) do not sum to reproduce the full pCO_2 seasonal

cycle (e.g., $pCO_{2\ mm} \neq pCO_{2\ T} + pCO_{2\ NT} - pCO_{2\ am}$). This is because the thermal sensitivity of pCO_2 (expressed with a factor of 0.0423/°K in the equations above) in fact varies slightly with background chemistry (Wanninkhof et al., 1999).

In this study, we use the alternative approach of Fassbender et al. (2022), where an important focus of the analysis is to identify asymmetries in seasonal pCO_2 variations. For this case, rather than working with an annual mean pCO_2 to characterize asymmetries, one defines a neutral pCO_2 with respect to the annual cycle as being the pCO_2 one would obtain using annual means of its drivers (T, S, DIC, TA, PO_4, and SiO_4), which reflects the mean pCO_2 if pCO_2 were to respond linearly to the seasonal variability of its drivers. With this in mind, $pCO_{2\ AM}$ is given by:

$$pCO_{2\ AM} = f\left(\overline{T}, \overline{S}, \overline{DIC}, \overline{TA}, \overline{PO_4}, \overline{SIO_4}\right) \quad (3)$$

where the function f() represents a carbon system calculator. The time-varying (monthly mean) thermally-driven pCO_2 component can be identified using the same approach but by using monthly varying output temperature for the carbonate system calculator:

$$pCO_{2\ T\ FASS} = f\left(T_{mm}, \overline{S}, \overline{DIC}, \overline{TA}, \overline{PO_4}, \overline{SIO_4}\right) \quad (4)$$

The thermal pCO_2 component seasonal cycle anomaly is then determined as:

$$pCO_{2\ T_{anom}} = pCO_{2\ T\ FASS} - pCO_{2\ AM} \quad (5)$$

making it possible to calculate the nonthermal component by difference:

$$pCO_{2\ NT\ FASS} = pCO_2 - pCO_{2\ T_{anom}} \quad (6)$$

These definitions for thermal- and nonthermal decomposition in Equations (5)-(6), which are applied in **Fig. 6**, will prove to be important to our attribution of decadal changes in pCO_2 seasonality, to identify whether decadal changes project differently onto summer and winter.

Attribution of decadal changes in the pCO_2 seasonal cycle

The goal of the attribution analysis is to isolate the direct (C_{ant}) and indirect (climate change; Clim) influences of C_{ant} on pCO_2 seasonal cycle changes between the time periods of interest via offline calculations. Due to the short duration over which this method is applied relative to what it was originally designed for (i.e., >100-year time scales), both the C_{ant} and Clim components of the total pCO_2 seasonal cycle change may contain non-trivial interference from natural variability, which we attempt to constrain with the CESM2 LE analysis in **Sections 3.3.1** and **3.3.2**. Here we provide further description of the method of Fassbender et al. (2022) to facilitate understanding of the attribution analysis for decadal changes; however, readers are encouraged to review the original publication for complete methodological details.

To perform the attribution analysis, we focus on isolating the direct and indirect impacts of C_{ant} on thermal and nonthermal pCO_2 component seasonal cycle changes. Since these calculations are performed offline, the method requires an initial step of reconstructing the model pCO_2 values. A Taylor series decomposition was used previously in **Section 3.2.2** to compare discrepancies between the GOBM and pCO_2 product seasonal pCO_2 variability resulting from each of its drivers. A similar approach is used here for attribution following the method of Fassbender et al. (2022).

Changes in surface ocean pCO_2 with time can be expressed as the sum of temporal changes in the various pCO_2 drivers multiplied by the sensitivity of pCO_2 to that driver:

$$\frac{dpCO_2}{dt} = \left(\frac{\partial pCO_2}{\partial DIC}\right)\left(\frac{\partial DIC}{\partial t}\right) + \left(\frac{\partial pCO_2}{\partial TA}\right)\left(\frac{\partial TA}{\partial t}\right) + \left(\frac{\partial pCO_2}{\partial SSS}\right)\left(\frac{\partial SSS}{\partial t}\right) + \left(\frac{\partial pCO_2}{\partial SST}\right)\left(\frac{\partial SST}{\partial t}\right) \quad (7)$$

The first three terms on the right-hand side reflect the nonthermal pCO_2 drivers and the last term on the right-hand side reflects the thermal pCO_2 driver. For the thermal sensitivity, we use a carbonate system calculator, as described in the preceding section, to isolate the monthly thermal pCO_2 component anomalies ($pCO_{2\ Tanom}$) relative to $pCO_{2\ AM}$ at each grid point during each year of 1985-1989 and 2014-2018. For the remaining sensitivity terms, we rely on familiar relative sensitivity terms including the Revelle Factor (RF; (Bolin & Eriksson, 1959;

Broecker et al., 1979)), Alkalinity Factor (AF; (Takahashi et al., 1993)), and Salinity Factor (Takahashi et al., 1993), which all take the same form, with an example for the AF given here:

$$AF = \left(\frac{\Delta pCO_2}{\overline{pCO_2}}\right) \times \left(\frac{\Delta TA}{\overline{TA}}\right)^{-1} \quad (8)$$

Where ΔpCO_2 reflects the change imposed by a small TA perturbation (ΔTA) to initial TA and pCO_2 values with all other parameters held constant. The RF is provided as direct output from the carbonate system calculator while the AF and SF are calculated using the carbonate system calculator by independently imposing small TA and salinity perturbations (±0.01 µmol/kg TA and ±0.0001, respectively) for each grid point and month.

Monthly anomalies (Δ) in DIC, TA and SSS, relative to their annual mean values, can then be multiplied by their corresponding relative sensitivity factors to estimate the relative change in pCO_2. These relative changes in pCO_2 are then summed and multiplied by $pCO_{2\ AM}$ to estimate the corresponding monthly nonthermal pCO_2 component anomalies ($pCO_{2\ NT}$) relative to $pCO_{2\ AM}$ at each grid point during each year of 1985-1989 and 2014-2018, as follows:

$$pCO_{2\ NT_{anom}} = pCO_{2\ AM} \times \left(\left[RF \times \left(\frac{\Delta DIC}{\overline{DIC}}\right)\right] + \left[AF \times \left(\frac{\Delta TA}{\overline{TA}}\right)\right] + \left[SF \times \left(\frac{\Delta SSS}{\overline{SSS}}\right)\right]\right) \quad (9)$$

Summing the thermal and nonthermal component anomalies with $pCO_{2\ AM}$ yields the total pCO_2 value consistent with the model pCO_2 output for the time periods of interest. The offline reconstruction of the model pCO_2 field is important in later methodological steps when we difference a suite of calculated values that are subject to the same offline estimation uncertainties.

To isolate the influence of C_{ant} and Clim on $pCO_{2\ NT}$, we perform the same calculations outlined above but use the climatological monthly mean RF and AF values from the 1985-1989 period in each year of the 2014-2018 calculations. This holds the sensitivity of pCO_2 to the nonthermal carbonate system drivers constant at the 1980s level, providing an estimate of the indirect impact of C_{ant} (i.e., Clim) on the nonthermal pCO_2 component ($pCO_{2\ NTanom\text{-}Clim}$).

The difference between $pCO_{2\ NTanom}$ and $pCO_{2\ NTanom\text{-}Clim}$ yields an estimate of the direct impact of C_{ant} on the nonthermal pCO_2 component.

$$pCO_{2\ NT_{anom}-C_{ant}} = pCO_{2\ NT_{anom}} - pCO_{2\ NT_{anom}-Clim} \quad (10)$$

Similarly, to isolate the influence of C_{ant} and Clim on $pCO_{2\ T}$, we use the same carbonate system calculator approach described in the previous section but apply the climatological $pCO_{2\ AM}$ value from the 1985-1989 period ($pCO_{2\ AM80s}$) in each year of the 2014-2018 calculations as input values rather than annual mean DIC.

$$pCO_{2\ T\ FASS80s} = f\left(SST_{mm}, \overline{SSS}, pCO_{2\ AM80s}, \overline{TA}, \overline{PO_4}, \overline{SIO_4}\right) \quad (11)$$

This holds the thermal sensitivity of pCO_2 constant at the 1980s level providing an estimate of the indirect impact of C_{ant} (i.e., Clim) on the thermal pCO_2 component ($pCO_{2\ Tanom\text{-}Clim}$). We then subtract $pCO_{2\ AM80s}$ to yield the thermal term anomalies for each year of the 2014-2018 period.

$$pCO_{2\ T_{anom}-Clim} = pCO_{2\ T\ FASS80s} - pCO_{2\ AM80s} \quad (12)$$

The difference between $pCO_{2\ Tanom}$ and $pCO_{2\ Tanom\text{-}Clim}$ yields an estimate of the direct impact of C_{ant} on the thermal pCO_2 component.

$$pCO_{2\ T_{anom}-C_{ant}} = pCO_{2\ T_{anom}} - pCO_{2\ T_{anom}-Clim} \quad (13)$$

Summing the thermal and nonthermal anomalies derived using time-varying and constant sensitivity terms with $pCO_{2\ AM}$ yields the total pCO_2 and $pCO_{2\ Clim}$ values, respectively, which can be differenced to isolate the C_{ant} contribution:

$$pCO_{2\ C_{ant}} = pCO_2 - pCO_{2\ Clim} \quad (14)$$

With the Clim and C_{ant} components of total pCO_2 differentiated relative to the 1980s reference period, we can assess attribution for the changes in seasonal cycle characteristics in the thermal, nonthermal, and full pCO_2 values for the 2014-2018 period.

Fig. S1: Time series of the net amplitude (annual maximum minus minimum) of monthly CO_2 fluxes spatially integrated over the six aggregated biomes shown in **Fig. 1**. The GOBMs (green) and pCO_2 products (blue) are shown for their product-mean (bold line) and 1-std of their spread amongst individual products (shaded).

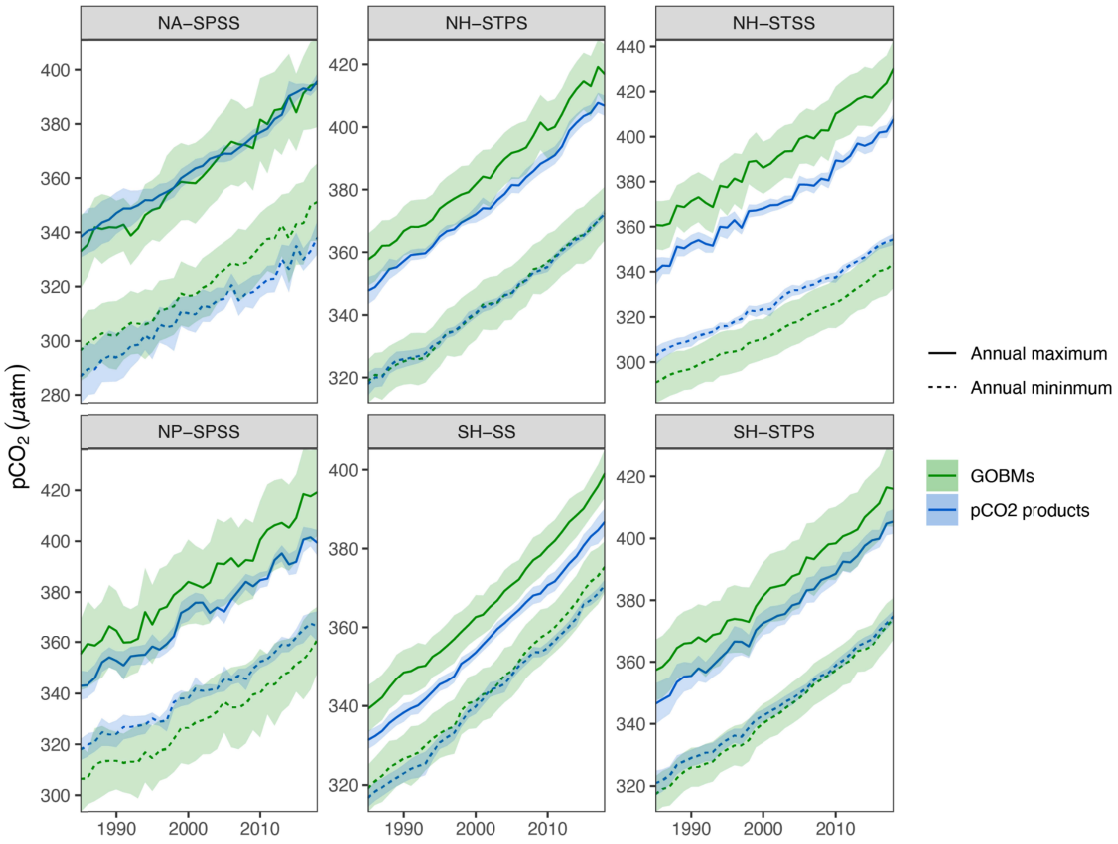

209

210 **Fig. S2**: Time series of pCO_2 averaged over biomes showing annual maximum and annual
211 minimum values, both for GOBMs and for pCO_2 products. Lines indicate the mean and
212 shading indicates the one standard deviation range for each ensemble of estimates.

213

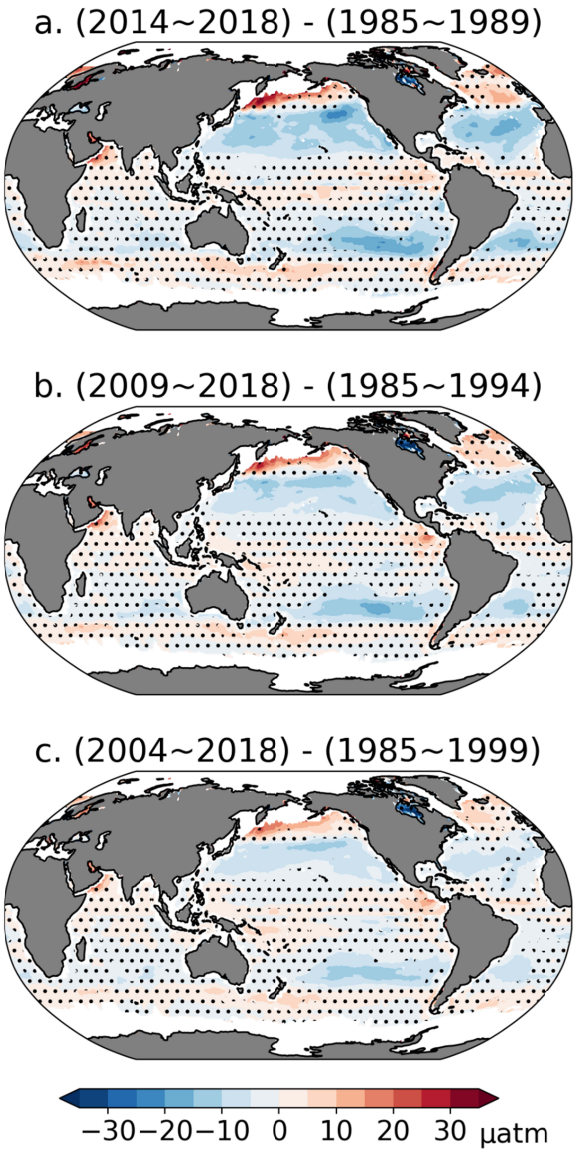

214

215 **Fig. S3**: Evaluation of the sensitivity of the decadal changes in pCO_2 seasonal amplitude for
216 the pCO_2 products using (a) five-year climatologies, (b) 10-year climatologies, and (c) 15-
217 year climatologies. Panel (a) is the same field shown in **Fig. 3a**.

218

219

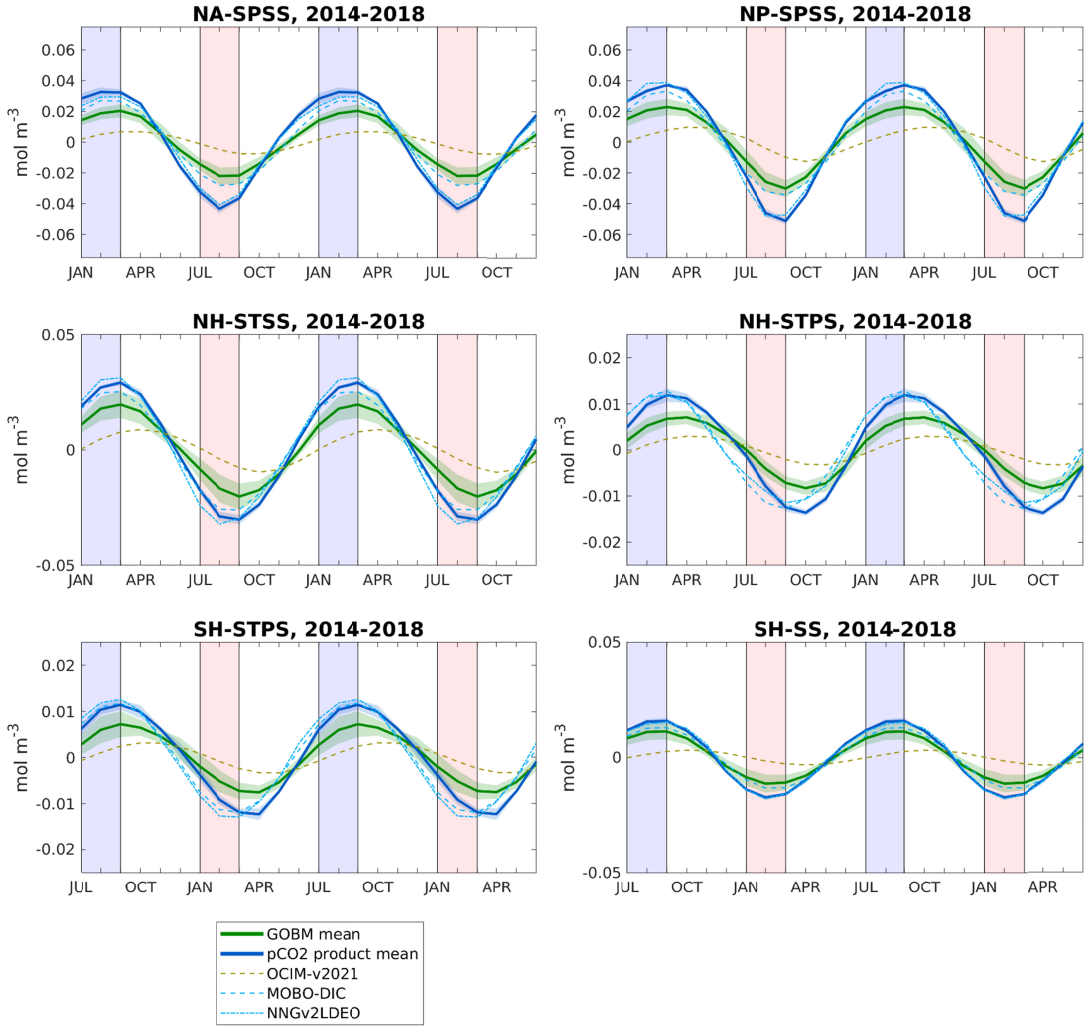

Fig. S4: Climatological seasonal cycle anomalies for 2014-2018 DIC over the six aggregated biomes for GOBMs (green), pCO_2 products (blue), for OCIM (brown, dashed), and for the two DIC-climatologies MOBO-DIC (lightblue, dashed) and NNGv2LDEO (lightblue, dash-dotted). The biome names as defined in **Table 1** and **Fig. 1** are given in each panel title. Ensemble means for GOBMs and pCO_2 products are shown as thick lines while the shading indicates the standard deviation around the mean. Note that the DIC climatologies are referenced to time periods 2004 through 2017 for MOBO-DIC and 1995 for NNGv2LDEO different from the averaging period used for GOBMs and pCO_2 products (2014-2018). Also note that, due to differences in spatial data coverage, the inclusion of MOBO-DIC and NNGv2LDEO entails that the areas.

Bakker, D. C. E., Pfeil, B., Landa, C. S., Metzl, N., O'Brien, K. M., Olsen, A., et al. (2016). A multi-decade record of high-quality fCO2 data in version 3 of the Surface Ocean CO2 Atlas (SOCAT). *Earth System Science Data*, *8*(2), 383–413. https://doi.org/10.5194/essd-8-383-2016

Bolin, B., & Eriksson, E. (1959). Changes in the carbon dioxide content of the atmosphere and sea due to fossil fuel combustion. *The atmosphere and the sea in motion*.

Broecker, W. S., Takahashi, T., Simpson, H. J., & Peng, T. H. (1979). Fate of Fossil Fuel Carbon Dioxide and the Global Carbon Budget. *Science*, *206*(4417), 409–418. https://doi.org/10.1126/science.206.4417.409

Broullón, D., Perez, F. F., Velo, A., Hoppema, M., Olsen, A., Takahashi, T., et al. (2019). A global monthly climatology of total alkalinity: a neural network approach. *Earth System Science Data*. https://doi.org/10.5194/essd-11-1109-2019

Broullón, D., Pérez, F. F., Velo, A., Hoppema, M., Olsen, A., Takahashi, T., et al. (2020). A global monthly climatology of oceanic total dissolved inorganic carbon: a neural network approach. *Earth System Science Data*, *12*(3), 1725–1743.

Carter, B. R., Feely, R. A., Williams, N. L., Dickson, A. G., Fong, M. B., & Takeshita, Y. (2018). Updated methods for global locally interpolated estimation of alkalinity, pH, and nitrate. *Limnology and Oceanography-Methods*, *16*(2), 119–131. https://doi.org/10.1002/lom3.10232

Chau, T. T. T., Gehlen, M., & Chevallier, F. (2022). A seamless ensemble-based reconstruction of surface ocean pCO 2 and air–sea CO 2 fluxes over the global coastal and open oceans. *Biogeosciences*, *19*(4), 1087–1109.

254 Dickson, A. G. (2010). The carbon dioxide system in seawater: equilibrium chemistry and
255 measurements. *Guide to Best Practices for Ocean Acidification Research and Data*
256 *Reporting*, *1*, 17–40.

257 Dickson, A. G., & Millero, F. J. (1987). A comparison of the equilibrium-constants for the
258 dissociation of carbonic acid in seawater media. *Deep-Sea Res.*
259 https://doi.org/10.1016/0198-0149(87)90021-5

260 Dickson, A. G., Wesolowski, D. J., Palmer, D. A., & Mesmer, R. E. (1990). Dissociation
261 constant of bisulfate ion in aqueous sodium chloride solutions to 250°C. *Journal of*
262 *Physical Chemistry*, *94*(20), 7978–7985. https://doi.org/10.1021/j100383a042

263 Fassbender, A. J., Schlunegger, S., Rodgers, K. B., & Dunne, J. P. (2022). Quantifying the
264 role of seasonality in the marine carbon cycle feedback: an ESM2M case study.
265 *Global Biogeochemical Cycles*, *36*(6), e2021GB007018.

266 Garcia, H. E., Locarnini, R. A., Boyer, T. P., Antonov, J. I., Baranova, O. K., Zweng, M. M.,
267 et al. (2013). World ocean atlas 2013. Volume 4, Dissolved inorganic nutrients
268 (phosphate, nitrate, silicate).

269 Garcia, H. E., Weathers, K. W., Paver, C. R., Smolyar, I., Boyer, T. P., Locarnini, M. M., et
270 al. (2019). World ocean atlas 2018. Vol. 4: Dissolved inorganic nutrients (phosphate,
271 nitrate and nitrate+ nitrite, silicate).

272 Gregor, L., & Gruber, N. (2021). OceanSODA-ETHZ: a global gridded data set of the surface
273 ocean carbonate system for seasonal to decadal studies of ocean acidification. *Earth*
274 *System Science Data*, *13*(2), 777–808. https://doi.org/10.5194/essd-13-777-2021

Iida, Y., Takatani, Y., Kojima, A., & Ishii, M. (2021). Global trends of ocean CO2 sink and ocean acidification: an observation-based reconstruction of surface ocean inorganic carbon variables. *Journal of Oceanography*, *77*(2), 323–358. https://doi.org/10.1007/s10872-020-00571-5

Keppler, L., Landschützer, P., Gruber, N., Lauvset, S., & Stemmler, I. (2020a). Mapped Observation-Based Oceanic Dissolved Inorganic Carbon (DIC), monthly climatology from January to December (based on observations between 2004 and 2017), from the Max-Planck-Institute for Meteorology (MOBO-DIC_MPIM)(NCEI Accession 0221526), NOAA National Centers for Environmental Information [data set]. *Centers Environ. Information. Dataset., Https://Doi. Org/10.25921/Yvzj-Zx46*, *1020*.

Keppler, L., Landschützer, P., Gruber, N., Lauvset, S. K., & Stemmler, I. (2020b). Seasonal Carbon Dynamics in the Near-Global Ocean. *Global Biogeochemical Cycles*, *34*(12). https://doi.org/10.1029/2020gb006571

Landschützer, P., Gruber, N., & Bakker, D. C. E. (2016). Decadal variations and trends of the global ocean carbon sink. *Global Biogeochemical Cycles*, *30*(10), 1396–1417. https://doi.org/10.1002/2015gb005359

Lewis, E., & Wallace, D. (1998). CO2SYS-Program developed for the CO2 system calculations, Carbon Dioxide Inf. Anal. Center. *Oak Ridge National Laboratory, US Department of Energy, Oak Ridge, TN, USA*.

Locarnini, R. A., Mishonov, A. V., Antonov, J. I., Boyer, T. P., Garcia, H. E., Baranova, O. K., et al. (2013). Coauthors, 2013: Temperature. Vol. 1, World Ocean Atlas 2013, NOAA Atlas NESDIS 73, 40 pp.

297 Lueker, T. J., Dickson, A. G., & Keeling, C. D. (2000). Ocean pCO2 calculated from
298 dissolved inorganic carbon, alkalinity, and equations for K1 and K2: validation based
299 on laboratory measurements of CO2 in gas and seawater at equilibrium. *Marine*
300 *Chemistry*, *70*(1–3), 105–119. https://doi.org/10.1016/s0304-4203(00)00022-0

301 Mehrbach, C., Culberson, C. H., Hawley, J. E., & Pytkowicx, R. M. (1973). Measurement of
302 the apparent dissociation constants of carbonic acid in seawater at atmospheric
303 pressure 1. *Limnology and Oceanography*, *18*(6), 897–907.

304 Olsen, A., Lange, N., Key, R. M., Tanhua, T., Alvarez, M., Becker, S., et al. (2019).
305 GLODAPv2.2019-an update of GLODAPv2. *Earth System Science Data*, *11*(3),
306 1437–1461. https://doi.org/10.5194/essd-11-1437-2019

307 Raimondi, L., Matthews, J. B. R., Atamanchuk, D., Azetsu-Scott, K., & Wallace, D. W. R.
308 (2019). The internal consistency of the marine carbon dioxide system for high latitude
309 shipboard and in situ monitoring. *Marine Chemistry*, *213*, 49–70.

310 Roemmich, D., & Gilson, J. (2009). The 2004-2008 mean and annual cycle of temperature,
311 salinity, and steric height in the global ocean from the Argo Program. *Progress in*
312 *Oceanography*, *82*(2), 81–100. https://doi.org/10.1016/j.pocean.2009.03.004

313 Takahashi, T., Olafsson, J., Goddard, J. G., Chipman, D. W., & Sutherland, S. C. (1993).
314 Seasonal Variation of CO2 and Nutrients in the High-Latitude Surface Oceans: A
315 Comparative Study. *Global Biogeochemical Cycles*, *7*(4), 843–878.
316 https://doi.org/10.1029/93gb02263

317 Takahashi, T., Sutherland, S. C., Sweeney, C., Poisson, A., Metzl, N., Tilbrook, B., et al.
318 (2002). Global sea-air CO2 flux based on climatological surface ocean pCO2, and
319 seasonal biological and temperature effects. *Deep-Sea Research Part II: Topical*

Studies in Oceanography, *49*(9–10), 1601–1622. https://doi.org/10.1016/s0967-0645(02)00003-6

Takahashi, T., Sutherland, S. C., & Kozyr, A. (2017). Global ocean surface water partial pressure of CO2 database: Measurements performed during 1957–2016 (version 2016). *ORNL/CDIAC-161, NDP-088 (V2015), Carbon Dioxide Information Analysis Center, Oak Ridge National Laboratory, US Department of Energy, Oak Ridge, Tennessee, Dataset, Document available at: https://www. nodc. noaa. gov/ocads/oceans/LDEO_Underway_Database/NDP-088_V2016. pdf (last access: 31 July 2020)*.

Takatani, Y., Enyo, K., Iida, Y., Kojima, A., Nakano, T., Sasano, D., et al. (2014). Relationships between total alkalinity in surface water and sea surface dynamic height in the Pacific Ocean. *Journal of Geophysical Research-Oceans*, *119*(5), 2806–2814. https://doi.org/10.1002/2013jc009739

Uppstrom, L. (1974). The boron/chlorinity ratio of deep-sea water from the Pacific Ocean. *Deep Sea Res.*, *21*, 161–162.

Van Heuven, S. M. A. C., Pierrot, D., Rae, J. W. B., Lewis, E., & Wallace, D. W. R. (2011). MATLAB Program developed for CO2 system calculations, ORNL/CDIAC-105b, Carbon Dioxide Information Analysis Center, Oak Ridge National Laboratory, US Department of Energy, Oak Ridge, Tennessee, doi: 10.3334/CDIAC/otg. *CO2SYS MATLAB V1*, *1*.

Wanninkhof, R., Lewis, E., Feely, R. A., & Millero, F. J. (1999). The optimal carbonate dissociation constants for determining surface water pCO2 from alkalinity and total inorganic carbon. *Marine Chemistry*, *65*(3–4), 291–301.

Zweng, M. M., Seidov, D., Boyer, T. P., Locarnini, M. M., Garcia, H., Mishonov, A. V., et al. (2019). World ocean atlas 2018, volume 2: Salinity.